

Photodiodes for Applications in Quantum Information and Microwave Photonic Systems

A Dissertation

Presented to

the Faculty of the School of Engineering and Applied Science

University of Virginia

In Partial Fulfillment of the
Requirements for the Degree of
Doctor of Philosophy

By

Jizhao Zang

December 2018

APPROVAL SHEET

This Dissertation
is submitted in partial fulfillment of the requirements
for the degree of
Doctor of Philosophy

Author Signature: _____

This Dissertation has been read and approved by the examining committee:

Advisor: Joe C. Campbell

Committee Member: Andreas Beling

Committee Member: Arthur W. Lichtenberger

Committee Member: Kyusang Lee

Committee Member: Olivier Pfister

Committee Member: _____

Accepted for the School of Engineering and Applied Science:



Craig H. Benson, School of Engineering and Applied Science

December 2018

Copyright by

Jizhao Zang

All rights reserved

2018

*This dissertation is dedicated
to my parents and my sister*

Contents

Acknowledgement	VIII
Abstract	X
List of Figures	XII
List of Tables	XVII
Chapter 1. Introduction	1
1.1 High-efficiency photodiodes for quantum information processing.....	1
1.2 Photovaractor for optically modulated scatterer	2
1.3 MUTC photodiodes with reduced AM-to-PM noise conversion	5
1.4 Dissertation organization.....	6
Chapter 2. Photodiode fundamentals	7
2.1 Important parameters of photodiodes.....	7
2.1.1 <i>Responsivity and quantum efficiency</i>	7
2.1.2 <i>Bandwidth</i>	9
2.1.3 <i>Photodiode nonlinearity</i>	14
2.1.4 <i>S11 of the photodiode</i>	18
2.1.5 <i>AM-to-PM Coefficient</i>	21
2.2 Different photodiode structures.....	22
Chapter 3. Fabrication process	26
3.1 P-mesa etch.....	26
3.2 N-mesa etch.....	28
3.3 N-metal deposition	29
3.4 Open P-contact	31
3.5 Other steps.....	32
Chapter 4. High-efficiency photodiodes for quantum information processing	35

4.1 Device design and fabrication	35
4.2 Device Characterization	37
4.3 Conclusion.....	47
Chapter 5. Photovaractor for optically modulated scatterer	48
5.1 Device design and fabrication	48
5.2 Device Characterization	53
5.3 Photovaractor flip-chip bonded with matching network.....	60
5.4 Conclusion.....	62
Chapter 6. Photovaractor Working as a Microwave Attenuator	63
6.1 Introduction	63
6.2 Principle of the optically-controlled microwave attenuator	63
6.3 Results and discussions	65
6.4 Conclusion.....	67
Chapter 7. AM-to-PM in transit-time limited Photodiodes	68
7.1 Introduction	68
7.2 Device design and fabrication	69
7.2 Device Characterization	73
7.3 Conclusion.....	81
Chapter 8. Investigation of AM-to-PM in Large Devices.....	82
8.1 Introduction	82
8.2 Results and discussions	82
8.3 Conclusions	93
Chapter 9. Conclusions and Future work.....	94
9.1 Conclusions	94
9.2 Future work	95

9.2.1 Application of photovaractors in other microwave circuits.....	95
9.2.2 Further investigation on the AM-to-PM in large devices	95
9.2.3 Investigation of photodiode nonlinearity.....	96
References	99
A. List of publications.....	112
B. Vita.....	115

Acknowledgement

This dissertation is a summary of my work at University of Virginia. The University of Virginia is a great place for research and Charlottesville is also a wonderful place to live. I feel so lucky to have worked with many excellent researchers here and I would like to express my deepest appreciation to all of them.

First, I would like to express my deepest gratitude to my advisor, Dr. Joe C Campbell. His enthusiasm for scientific research impressed me very much. He not only provides insightful research guidance, but also offers the best he can to help us in personal life. He is so friendly and always glad to share his stories with us. Thanks to his support and encouragement, I was able to smoothly finish my study. He has set an example for me to learn for the rest of my life. I feel so lucky and honored to be a student of such friendly and knowledgeable man who made outstanding contributions to photonics.

I also would like to thank my proposal committee, Dr. Andreas Beiling, Dr. Arthur W. Lichtenberger, Dr. Olivier Pfister, and Dr. Kyusang Lee. They have given me a lot of valuable suggestions and helped me improve my research, especially Dr. Andreas Beiling, who is always very patient and glad to help me. I benefited greatly from many productive discussions with him. Besides being smart and knowledgeable in research, he is also humorous and friendly in daily life. It is really a memorable experience to have worked with him.

I feel so grateful to our group members: Xiaojun Xie, Min Ren, Yang Shen, Keye Sun, Jiyuan Zheng, Nan Ye, Yaojia Chen, Zhanyu Yang, Qianhuan Yu, Ye Wang, Qinglong Li, Madison Woodson, Jesse S. Morgan, Bassem M. Tossoun, Andrew H. Jones, Yuan Yuan, Ze Wang, Yiwei Peng, Ta Ching Tzu, Junyi Gao, Junming Mao, Fengxin Yu, and Arber Kaso. I have unforgettable memories of working and playing with them, especially Xiaojun Xie, who gave me a lot of help

in both scientific research and personal life like an elder brother; Jesse S. Morgan and his family, who treated me as one of their family members and made me feel at home even abroad.

I would like to thank the staff of the Microfabrication Lab at University of Virginia, Alex Lobo, Michael Stogoski, and Joseph Beatrice. Thanks for their contributions in student training and instrument maintenance of the cleanroom. Without their technical support, I would not have finished my fabrication in a timely manner.

Last, but not least, I would thank my family: my father Zhanqian Zang, my mother Chaoyu Zhao, and my sister Shanshan Zang. Without their support and love, I could not have finished my PhD study. It has been three years since I saw them last time and I miss them very much. I feel so grateful for their love and I will love them forever.

Jizhao Zang

University of Virginia

August 2018

Abstract

Photodiodes are widely used in quantum optical and microwave photonic systems. This dissertation focuses on three topics: high quantum efficiency photodiodes, a photovaractor for optically modulated scatterer, and investigation of AM-to-PM noise conversion.

For the high-efficiency photodiodes, we achieved 98% $\pm 0.8\%$ external quantum efficiency at 1064 nm. At bias voltage of -5 V, the 3 dB bandwidth is 7 GHz and the dark current is ~ 10 nA. The dark current at low bias voltage is dominated by generation-recombination with 0.23 eV activation energy.

For the photovaractor, we designed III-V photovaractors whose capacitance change is based on the decrease of depletion width and the steep increase of the effective area after illumination. At photocurrent of 12 mA, the reactance at 60 GHz is changed by 280 times relative to the dark condition. S11 parameter fitting shows that the capacitance of a 50 μm -diameter device increases by 37 times after illumination. The photovaractor is further flip-chip bonded with matching network to enhance the scattering. The S11 can be changed by ~ 40 dB by modulating it optically or electrically. Further, the proposed photovaractor is used as an optically-controlled microwave attenuator. By changing the photocurrent, a dynamic range of up to 40 dB is achieved. At photocurrent < 3 mA, the phase variation is less than 10 degrees in the frequency range of 5 GHz to 55 GHz.

For the investigation of AM-to-PM, we have optimized the epitaxial layer design of the CC-MUTC photodiodes to reduce the AM-to-PM noise conversion. Measurement results show that the range of phase change at different photocurrent is reduced by more than three times and the AM-to-PM conversion is greatly suppressed, especially at large photocurrent. For 10 μm

devices, the 3-dB bandwidth is 35 GHz at bias voltage of -6 V and the maximum RF output power at 15 GHz is 13.7 dBm after optimization. The AM-to-PM in large ($>10 \mu\text{m}$) devices is also investigated. Measurement shows that not only the carrier transit time, but also the RC phase response will influence the AM-to-PM in large devices.

List of Figures

Figure 1-1. Measurement of the radiation pattern of the antenna with an optically modulated scatterer.	2
Figure 1-2. Generation of ultra-stable microwave signals based on optical frequency combs stabilized to an optical reference [1.37].	5
Figure 2-1. The equivalent circuit of the photodiode.	10
Figure 2-2. Bandwidth measurement setup based on intensity modulators.	11
Figure 2-3. Optical heterodyne setup for bandwidth measurement.	12
Figure 2-4. A comparison between linear and nonlinear photodetection.	14
Figure 2-5. Definition of OIP3.	15
Figure 2-6. Three-tone OIP3 measurement setup.	16
Figure 2-7. S11 measurement setup.	18
Figure 2-8. S11 parameter fitting: (a) Equivalent circuit in Keysight ADS software; (b) fitting result.	19
Figure 2-9. Comparison between the fitted capacitance for different frequency range.	20
Figure 2-10. AM-to-PM measurement setup.	21
Figure 2-11. (a) Photos of a photodiode killed by thermal energy; (b) Space charge effect at large photocurrent.	22
Figure 2-12. Different photodiode structures.	23
Figure 3-1. Deposition of p contact metal and silicon dioxide hard mask.	26
Figure 3-2. Process of p mesa etch (PR: photoresist).	27
Figure 3-3. Process of n mesa etch.	29
Figure 3-4. Process of open n contact and n metal deposition.	30

Figure 3-5. Process of open p contact.	31
Figure 3-6. An example of the wafer before dicing.	32
Figure 3-7. Device after flip-chip bonding.	33
Figure 4-1. Epitaxial-layer design of the high efficiency photodiode.	35
Figure 4-2. (a) Fabricated photodiode; (b) Backside surface after polishing; (c) Measured reflection coefficient of the anti-reflection coating.	36
Figure 4-3. (a) Current-voltage curves for devices of different size; (b) Dark current versus device diameter at different bias voltage.	37
Figure 4-4. Quantum efficiency measurement setup.	38
Figure 4-5. Comparison of the quantum efficiency before (a) and after (b) polishing.	39
Figure 4-6. (a) Measured quantum efficiency at different wavelength; (b) Possible origins of QE loss.	40
Figure 4-7. Measured quantum efficiency at higher incident optical power.	41
Figure 4-8. The measured bandwidth at different bias voltage.	42
Figure 4-9. Measured bandwidth of 50 μm devices at different photocurrent.	43
Figure 4-10. Current-voltage curves of a 50 μm device for temperature 80 K to 300 K in 20 K steps.	44
Figure 4-11. $-\ln(I_{\text{dark}}/T^2)$ versus $1/kbT$ for a 50 μm -diameter device at (a) -10 V and (b) -35 V.	46
Figure 5-1. Epitaxial-layer design of the photovaractor.	48
Figure 5-2. The depletion region in the dark case (a) and after illumination (b).	50
Figure 5-3. The decrease of depletion width after illumination.	51
Figure 5-4. A vertical cut of the simulated electric field distribution.	52

Figure 5-5. (a) Measured current-voltage curves of devices with different area and (b) dark current at -5V versus the square of the diameter.....	53
Figure 5-6. (a) Measured capacitance-voltage curves for devices with diameters of 28 μm , 34 μm , 40 μm , and 50 μm ; (b) capacitance at - 5 V bias versus diameter.	54
Figure 5-7. S11 measurement setup.....	55
Figure 5-8. (a): S11 of a 50 μm -diameter photovaractor in the dark and after illumination. Two markers show the impedance at 60 GHz; (b) Equivalent circuit of the photovaractor.....	56
Figure 5-9. Calculated capacitance in the dark case: (a): capacitance of 50 μm device versus frequency; (b): capacitance at 60 GHz versus device size.....	57
Figure 5-10. Capacitance of different-size devices versus incident optical power.....	58
Figure 5-11. Capacitance versus photocurrent for 50 μm device at different reverse bias voltage. The measurement frequency is 60 GHz.....	59
Figure 5-12. Measurement setup.....	60
Figure 5-13 . Measured S11 versus frequency at different photocurrent.	61
Figure 5-14. Measured S11 at different bias voltage in the dark case.....	62
Figure 6-1. Epitaxial layers design (a) and equivalent circuit (b) of the photovaractor.	64
Figure 6-2. S11 measurement setup.....	65
Figure 6-3. Amplitude (a) and phase (b) of S11 for 34 μm devices flip-chip bonded with CPW.....	66
Figure 7-1. The epitaxial layer design of the CC-MUTC and optimized CC-MUTC.....	69
Figure 7-2. Simulated electric field distribution at different photocurrent for CC-MUTC (a) and optimized CC-MUTC (b).....	71
Figure 7-3. Fabricated back-illuminated devices.....	72

Figure 7-4. (a) Current-voltage curves of the optimized CC-MUTC photodiodes; (b) Dark current at -5V for devices with different diameter.	73
Figure 7-5. Measured phase versus photocurrent for CC-MUTC (a) and optimized CC-MUTC (b).	74
Figure 7-6. Calculated AM-to-PM coefficient versus photocurrent for CC-MUTC and optimized CC-MUTC at bias voltage of -3 V (a), -4 V (b), -5 V (c) and -6 V (d).	77
Figure 7-7. Measured 3-dB bandwidth of CC-MUTC and optimized CC-MUTC at different photocurrent, the bias voltage is -6 V.	78
Figure 7-8. Measured RF output power and RF power compression of 10 μm devices at different photocurrent.	79
Figure 7-9. Measured OIP3-photocurrent curves of optimized CC-MUTC at different bias voltage.	80
Figure 8-1. Comparison of the phase-photocurrent curves for 20 (a), 30 (b), 40 (c) photodiodes, the bias voltage is -3 V.	83
Figure 8-2. Variation of relative phase with bias voltage for different photodiodes, the photocurrent is fixed at ~ 10 mA.	84
Figure 8-3. Capacitance-voltage curves of the photodiodes with different diameter.	85
Figure 8-4. (a) ADS simulation model of the photodiode phase response; (b) simulated phase change with photodiode capacitance.	87
Figure 8-5. Measured phase-photocurrent curves at different frequency for 10 (a), 20 (b) and 40 (c) optimized CC-MUTC photodiodes.	90

Figure 8-6. Measured phase-photocurrent curves for different distance between the lensed fiber and devices, the device diameters are 10 μm (a), 20 μm (b), 30 μm (c) and 40 μm (d), respectively. 92

Figure 9-1. Influence of the equivalent circuit..... 95

Figure 9-2. Simulation schematic of the photodiode nonlinearity..... 96

List of Tables

Table 8-1. Simulated phase change for 10 um and 40 um photodiodes.	88
---	----

Chapter 1. Introduction

A photodiode is a sensor of light that converts photons into current [1.1-1.4]. The incident light is absorbed and electron-hole pairs are generated. The electrons and holes are collected by the anode and cathode and current flows if there is a closed circuit. Photodiodes are widely used in optical communication systems [1.5, 1.6], microwave signal generation [1.7, 1.8], quantum information systems [1.9, 1.10], and medical imaging instruments [1.11, 1.12]. My research focuses on photodiodes for applications in quantum information and microwave photonic systems, which includes three topics: high-efficiency photodiodes for quantum information processing, a photovaractor for optically modulated scatterer, and high-power modified untravelling carrier (MUTC) photodiodes with reduced AM-to-PM noise conversion.

1.1 High-efficiency photodiodes for quantum information processing

High quantum efficiency (QE) photodiodes are key components in quantum information and quantum optical systems [1.13-1.15]. To meet the demand of these systems, the photodiodes should have three characteristics. First, they need to work at 1064 nm, the wavelength of neodymium-doped yttrium aluminum garnet (Nd:YAG) lasers, which are ultra-stable, ultra-low noise, and are widely used in quantum optical systems. Second, the dark current needs to be as low as possible to reduce the noise because these photodiodes may be used to detect very weak signals. Third, the quantum efficiency needs to be as high as possible, especially for some specific applications such as light squeezing. In light squeezing experiments, the degree to which the amplitude or phase noise can be squeezed is directly determined by the photodiode quantum efficiency [1.14].

To increase the quantum efficiency, the most straightforward method is simply to increase the thickness of the absorber [1.16]. On the other hand, if the layer is too thick, recombination can become a limiting factor. Therefore, it is important to optimize the thickness for the material and the operating wavelength. It is also important to incorporate a high-quality anti-reflection coating. It is well known that a thick absorber results in a transit-time penalty [1.17]. Thus, high quantum efficiency is achieved at the cost of reduced bandwidth. However, for many quantum optical applications, the photodiode bandwidth does not need to exceed ~ 100 MHz [1.12, 1.17, 1.18].

In Chapter 4 we report high-quantum-efficiency uni-traveling-carrier (UTC) photodiodes that achieve $98\% \pm 0.8\%$ detection efficiency at 1064 nm. For 50 μm -diameter devices, the 3-dB bandwidth is 7 GHz, which is transit-time limited.

1.2 Photovaractor for optically modulated scatterer

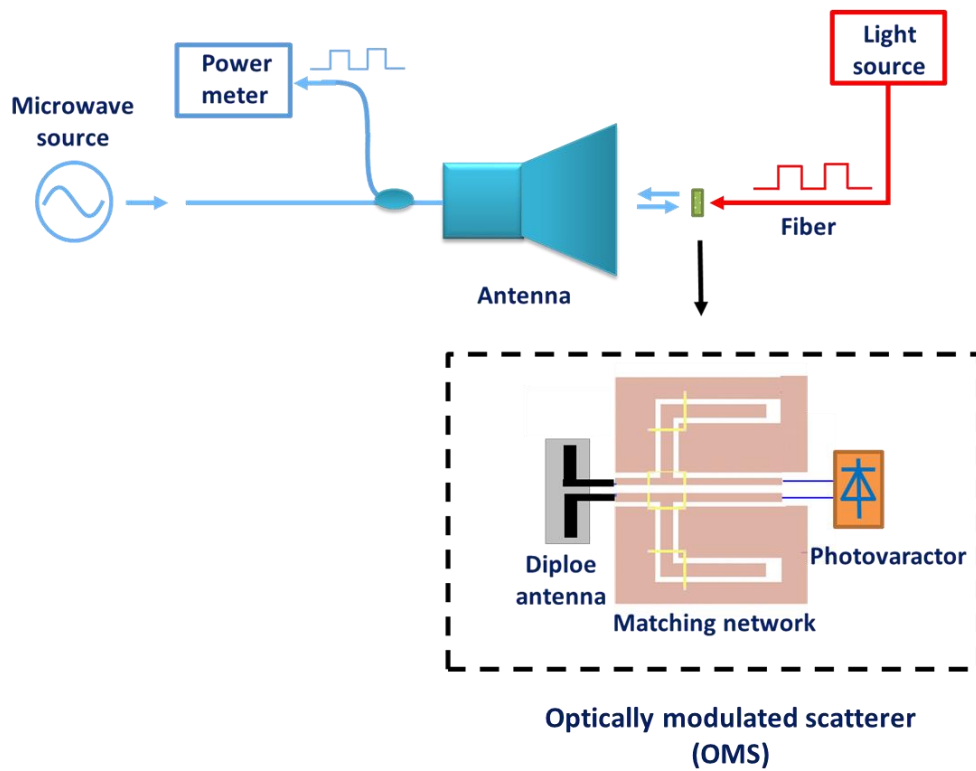


Figure 1-1. Measurement of the radiation pattern of the antenna with an optically modulated scatterer.

Varactors [1.19-1.22], which have voltage-dependent capacitance, are widely used in RF oscillators [1.23], reconfigurable antennas [1.24], and terahertz modulation [1.25]. However, for some applications, such as characterizing the radiation pattern of an antenna [1.26-1.28], the metal in the voltage supply cable of the varactor can alter the antenna field profile and lead to measurement error. A special type of photodiode, photovaractor, is a good candidate to solve this problem [1.29-1.31]. Fig. 1-1 shows the measurement of the radiation pattern of the antenna with optically modulated scatterer (OMS). The OMS consists of 3 parts: a dipole antenna, a microwave matching network and a photovaractor. The high-frequency signal from the antenna is reflected back by the OMS probe and measured by the power meter. To distinguish the reflected signal from the background reflection, the OMS performs low-frequency amplitude modulation on the reflected signal. This is achieved by controlling the impedance of photovaractor with intensity-modulated light through the optical fiber. Since the light intensity changes with time, the impedance of the photovaractor and the S11 of the OMS also change with time. Because the optical fiber is made of silicon dioxide, there is no electromagnetic interference and the original radiation pattern will not be influenced. Also, if the photovaractor can be operated at zero bias, the associated circuitry is greatly simplified. In addition, optical control has the advantage of fast tuning speed and good isolation between the controlling and microwave signals [1.30].

At low frequencies and zero bias, the AC signal from the measurement apparatus, e.g., LCR meter or vector network analyzer (VNA), may induce diffusion capacitance because the photovaractor is forward biased during the positive half cycle. As a consequence, the measured value may be larger than the actual depletion capacitance [1.32]. Higher AC signals will induce larger diffusion capacitance. At high frequencies, both the diffusion capacitance and depletion capacitance decrease; the diffusion component drops faster owing to its shorter carrier transport

time [1.33]. This calls into question whether the low frequency capacitance shift can be maintained at high frequencies. In recent years, there has been increasing demand for the circuits that operate at high-frequency microwave or even millimeter-wave bands, especially around 60 GHz. Having the advantage of license free, large band availability (~ 7 GHz), high security and low interference, the spectrum around 60 GHz is at the frontier of next generation high-speed wireless communications [1.34-1.36].

In Chapter 5 we report a zero-bias photovaractor that operates at up to 60 GHz. S11 measurement shows that illumination induces a large change of the impedance at 60 GHz. The resistance decreases by more than three times, while the reactance decreases by ~ 280 times. S11 parameter fitting is used to obtain the varactor equivalent circuit. The capacitance of a 50 μm -diameter device increases by 37 times after illumination. Good agreement is achieved between theory and measured results. The photovaractors are further flip-chip bonded with matching network and modulation depth of 39.5 dB is achieved. In Chapter 6, we will explore the application of photovaractors as an optically-controlled tunable microwave attenuator. Experimental results show that the proposed attenuator exhibits uniform attenuation in the frequency range of 5 GHz to 60 GHz. By changing the photocurrent, a dynamic range of up to 40 dB can be achieved.

1.3 MUTC photodiodes with reduced AM-to-PM noise conversion

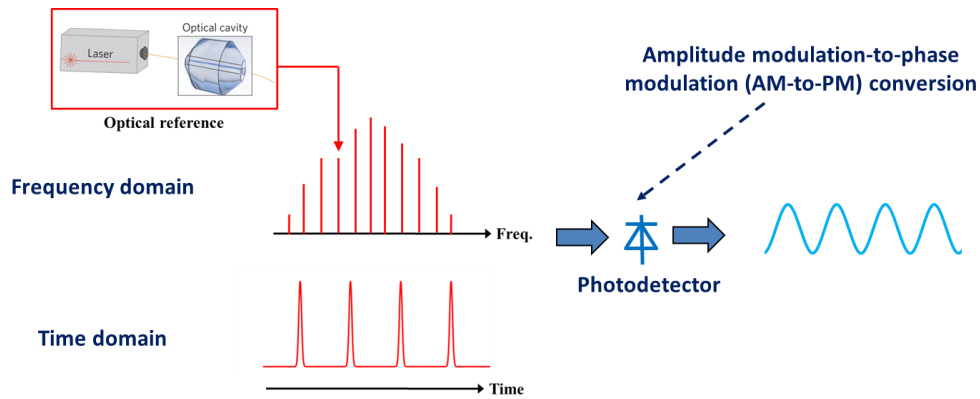


Figure 1-2. Generation of ultra-stable microwave signals based on optical frequency combs stabilized to an optical reference [1.37].

Amplitude modulation-to-phase (AM-to-PM) conversion of the photodiodes is related to the generation of ultra-stable microwave signals [1.37-1.39]. The ultra-stable microwave signals are widely used in coherent radar [1.40], telecommunication [1.41], ranging [1.42], and navigation systems [1.43]. Many approaches have been proposed to generate microwave signals with ultra-low phase noise [1.37, 1.44-1.48], among which the technique based on stabilized optical frequency combs has achieved the lowest phase noise reported to date. As shown in Fig. 1-2, the optical frequency comb from a mode-locked laser is phase-locked to the optical reference, which consists of a continuous wave (CW) laser stabilized to a high-Q Fabry-Perot (FP) resonant cavity. After photo-detection with a P-I-N photodiode, the frequency stability of the CW laser is transferred to the generated microwave signal. Based on this approach, a 10 GHz signal with integrated timing jitter of 760 fs over a bandwidth from 1 Hz-1 MHz is generated. This is one of most stable microwave signals generated by any source [1.37].

In this type of photonic oscillator, the phase noise is so low that any noise induced by the components cannot be neglected. One of the primary noise sources is identified as amplitude-to-

phase conversion in the photo-detection process [1.49-1.52]. Due to the AM-to-PM effect, the intensity fluctuations of the laser are converted to phase variations of the generated microwave signal, which can significantly affect the overall timing performance. Therefore, it is necessary to optimize the photodiodes and reduce the AM-to-PM conversion. In our previous work [1.53], the AM-to-PM conversion in charge-compensated modified unitravelling carrier (CC-MUTC) photodiodes is investigated. The origin of AM-to-PM conversion is identified as the electron acceleration by the self-induced field in the un-depleted absorption region and hole deceleration due to the collapsed electrical field in the depleted absorption region.

In Chapter 7 I describe optimization of the epitaxial layer design of the CC-MUTC based on our conclusions in [1.53]. Comparison of the phase measurement results indicates that the AM-to-PM conversion in 10 μm devices is greatly suppressed after optimization. For 10 μm devices, the 3-dB bandwidth is 35 GHz at bias voltage of -6 V and the maximum RF output power at 15 GHz is 13.7 dBm. In Chapter 8 we further investigated the AM-to-PM in photodiodes with diameter > 10 μm . Experimental results show that not only the transit-time, but also the RC phase response of the photodiode will influence the AM-to-PM in these devices.

1.4 Dissertation organization

This dissertation focuses on the photodiodes for applications in quantum information and microwave photonic systems. It is organized as follows: Chapter 2 introduces some photodiode fundamentals, which include the important parameters of photodiodes and different photodiode structures; Chapter 3 describes the fabrication process; The high-efficiency photodiode is investigated in Chapter 4; Chapter 5 and 6 discuss the photovaractors and their applications; Chapter 7 and 8 are the investigation on AM-to-PM in transit-time limited (10 μm) and larger photodiodes. Chapter 9 is the summary and future work.

Chapter 2. Photodiode fundamentals

2.1 Important parameters of photodiodes

2.1.1 Responsivity and quantum efficiency

The responsivity of the photodiode is defined as the ratio of the generated photocurrent to the incident optical power, and can be expressed as:

$$R_p = \frac{I_p}{p} = \frac{I - I_{dark}}{p}, \quad (2.1)$$

where p , I , I_p , and I_{dark} are the incident optical power, total current, photo-generated current, and dark current, respectively. The dark current is a small current that flows through a reverse biased photodiode in the absence of light. It is generated by three current sources: generation-recombination through R-G centers, band-to-band tunneling, and diffusion of thermally generated minority carriers [2.1].

There are two types of quantum efficiency that are usually considered, external quantum efficiency and internal quantum efficiency. The external quantum efficiency is used to describe the probability that each incident photon generates an electron-hole pair that contributes to the photocurrent. It is defined as the ratio of the number of effectively-generated electrons/holes to the number of incident photons:

$$\eta_{external} = \frac{N_e}{N_p} = \frac{I_p \cdot h\nu}{p \cdot q} \quad (2.2)$$

where h is the Plank constant, ν is optical frequency, and q is electron charge. From Eq. 2.1 and Eq 2.2, it can be seen that the relationship between responsivity and the external quantum efficiency is:

$$\eta_{external} = R_p \frac{h\nu}{q} \quad (2.3)$$

The internal quantum efficiency is defined as the ratio of the number of effectively-generated electrons/holes to the number of absorbed photons. It is determined by material properties and light propagation distance in the absorption layers:

$$\eta_{internal} = \xi \left[1 - e^{-\alpha(\lambda)d} \right] \quad (2.4)$$

where $\alpha(\lambda)$ is the absorption coefficient at wavelength λ , d is the light propagation distance, and ξ is the ratio of electron-hole pairs that avoid recombination and contribute to the overall photocurrent. Eq. 2.4 shows that, for a certain absorption material, high internal quantum efficiency can be achieved by increasing the thickness of absorption layers.

The relationship between the external and internal quantum efficiency can be expressed as:

$$\eta_{external} = \eta_{internal} (1 - \eta_{loss}) = \xi (1 - \eta_{loss}) \left[1 - e^{-\alpha(\lambda)d} \right] \quad (2.5)$$

where η_{loss} denotes the propagation loss from the air/semiconductor interface to the absorption layers. Eq. 2.3 and Eq. 2.5 are the two expressions of the external quantum efficiency. In this thesis, unless otherwise stated, the quantum efficiency refers to the external quantum efficiency.

For the vertically-illuminated photodiodes, the propagation loss mainly results from the reflection at the air/semiconductor interface. Owing to the refractive index discontinuity, there is also some reflection at the interface of different materials in the epitaxial layers, but normally it is insignificant. When light travels from a material with refractive index n_1 to a material with refractive index n_2 , the reflection loss can be calculated as:

$$R_{loss} = \frac{(n_1 - n_2)^2}{(n_1 + n_2)^2} \quad (2.6)$$

For example, in back-illuminated photodiodes with InP substrate, the reflection loss at 1550 nm is approximately 30.3 %. The reflection in the air/substrate interface is the predominant factor that limits the maximum achievable quantum efficiency. To maximize throughput and reduce the reflection loss, anti-reflection coatings, which consist of single or stacking dielectric layers, are usually used/employed [2.2, 2.3].

2.1.2 Bandwidth

Bandwidth is used to describe how fast the photodiodes can operate. As the modulation frequency of the incident light increases, at some point the RF output power of the photodiode will decrease. The 3 dB bandwidth is defined as the frequency at which the RF output power drops by 3 dB. The bandwidth of the photodiode is limited by two factors: the RC response time and the carrier transit time. An approximate formula for the 3 dB bandwidth is [2.4]:

$$f_{3dB} = \sqrt{\frac{1}{\frac{1}{f_{RC}^2} + \frac{1}{f_{tr}^2}}} \quad (2.7)$$

where f_{RC} and f_{tr} are the RC-limited and transit-time limited bandwidths, respectively. The RC-limited bandwidth originates from the resistance and capacitance of the photodiode. As shown in Fig. 2-1, C_{pn} , R_{pn} , R_s and R_L are the junction capacitance, junction resistance, series resistance and load resistance (usually 50 Ω), respectively. The RC-limited bandwidth can be expressed as:

$$f_{RC} = \frac{1}{2\pi C_{pn} (R_s + R_L)} \quad (2.8)$$

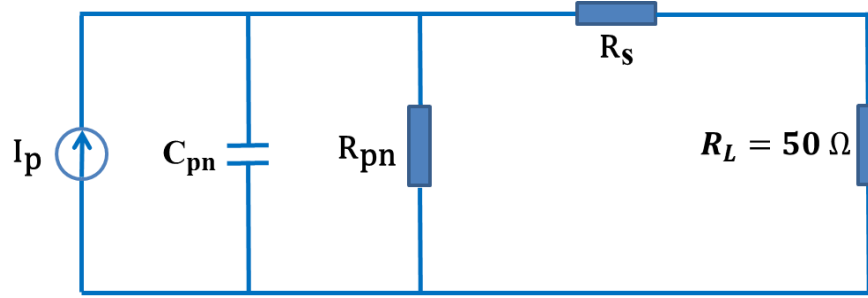


Figure 2-1. The equivalent circuit of the photodiode.

Eq. (2.8) shows that f_{RC} is inversely proportional to the junction capacitance, so a smaller junction capacitance is beneficial for increasing the RC-limited bandwidth. The junction capacitance is expressed as:

$$C_{pn} = \epsilon_0 \epsilon_r \frac{A_{PD}}{W_D} \quad (2.9)$$

where ϵ_0 is the electric constant, ϵ_r is dielectric constant of the material in the depletion region, A_{PD} is the cross-sectional area of the photodiode, and W_D is the width of the depletion region. By designing the photodiode with smaller area or wider depletion region, we can reduce the junction capacitance and achieve a larger RC-limited bandwidth. However, a wider depletion region also leads to larger transit-time and smaller f_{tr} , so there is a tradeoff and the thickness of the depletion region needs to be carefully optimized.

The transit-time limited bandwidth results from the fact that it takes time for the photo-generated electrons and holes to be collected by the metal contacts after generation in the absorption layers. It can be approximately calculated using the expressions [2.4]:

$$f_{tr} = \frac{3.5v}{2\pi D} \quad \text{and} \quad (2.10)$$

$$\bar{v} = \sqrt[4]{2 \left(\frac{1}{v_e^4} + \frac{1}{v_h^4} \right)^{-1}} \quad (2.11)$$

where v_e is the electron drift velocity, v_h is the hole drift velocity, and D is the carrier travel distance before being collected.

To measure the bandwidth, intensity-modulated light is incident on the photodiode. Based on the methods of generating intensity-modulated light, the bandwidth measurement setup is classified into two types: one is based on an intensity modulator and the other is based on optical heterodyning two free-running lasers.

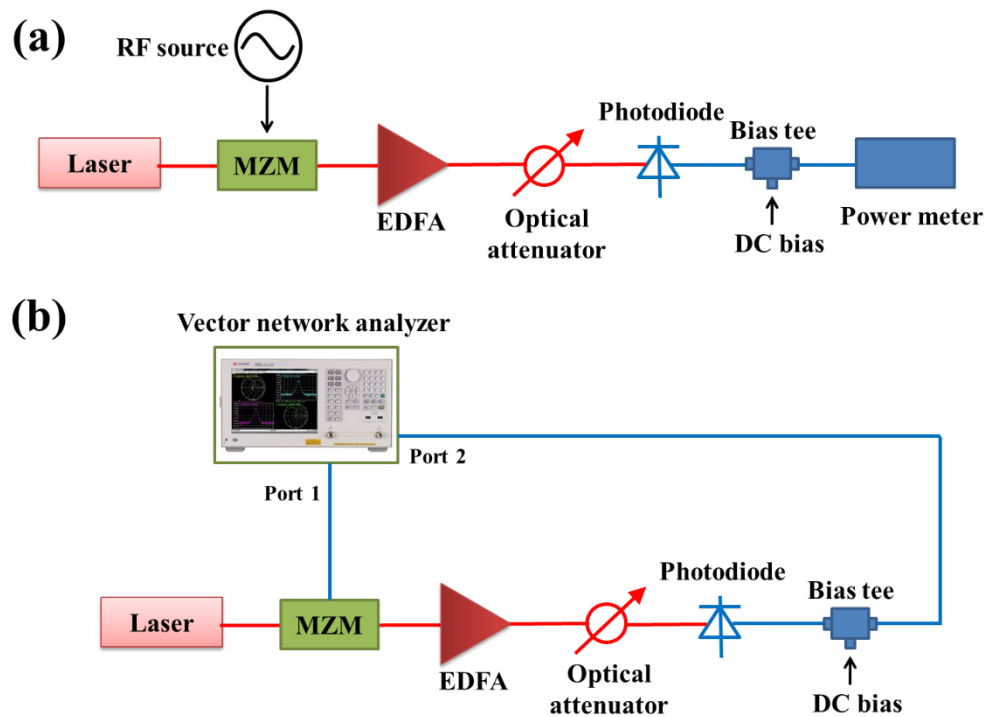


Figure 2-2. Bandwidth measurement setup based on intensity modulators.

As shown in Fig. 2-2, there are two alternative ways to measure the bandwidth using an intensity modulator. In Fig. 2-2 (a), a RF generator is used to drive a Mach-Zehnder modulator (MZM). CW light from the laser is modulated by the MZM, amplified by an EDFA, and coupled

into the photodiode. An optical attenuator is inserted after the EDFA to adjust the photocurrent. The RF output power of the photodiode is measured by a power meter. The bandwidth is measured by tuning the signal frequency of the RF source and monitoring the RF output power. In this setup, the bandwidths of the modulator and RF components (coaxial cables, RF connector, and bias tee) need to be much larger than the estimated bandwidth of the photodiode. They should have flat frequency response in the measurement frequency range, otherwise the measured results will be much smaller than the actual photodiode bandwidth.

An alternative way of using a modulator is shown in Fig. 2-2 (b). Compared with Fig. 2-2 (a), the RF source and power meter are replaced by a vector network analyzer. This setup is able to avoid the influence of the modulator and RF components by calibration with a high-speed photodiode before measurement. However, the bandwidth of the photodiode in calibration should be much larger than that of photodiodes under test.

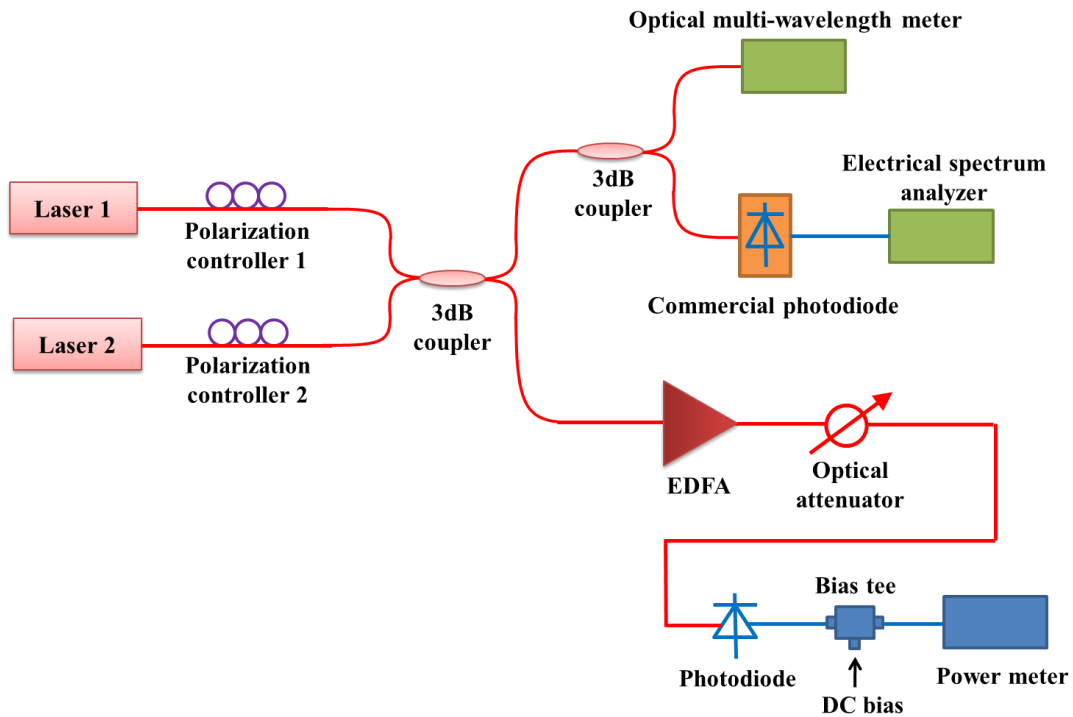


Figure 2-3. Optical heterodyne setup for bandwidth measurement.

Fig. 2-3 shows an optical heterodyne setup for bandwidth measurement [2.5]. CW light from two lasers at ~ 1550 nm is combined using a 3 dB optical coupler after two polarization controllers. Intensity-modulated light is generated when one laser beats with the other, and the modulation frequency is equal to the frequency difference between the two lasers, which is also called beat frequency. The output wavelength of the laser is temperature-controlled, so the beat frequency can be tuned by changing the temperature of one of the laser. To achieve 100% modulation, light from the two lasers needs to have the same intensity and polarization, which can be achieved by adjusting the laser current and polarization controllers, respectively. Another 3 dB optical coupler is used after the first optical coupler, so the heterodyned signal is split into 3 branches. In the first branch, the optical signal goes to an optical multi-wavelength meter to measure the frequency difference between the two lasers. In the second branch, the signal is detected by a commercial photodiode with 3 dB bandwidth of 50 GHz, and the beat signal (frequency) is measured by an electrical spectrum analyzer (ESA). Both of these measurements are used to monitor the beat frequency. When the beat frequency is lower than 50 GHz, it is measured with the ESA, which has high resolution (1 Hz), but limited measurement range (<50 GHz). When the beat frequency is higher than 50 GHz, it is measured with a multi-wavelength meter, which has low resolution, but broader frequency range. The third branch is similar to the setup in Fig. 2-2. The optical beat signal is amplified by an EDFA, attenuated by an optical attenuator and then sent to the photodiode under test. After a bias tee, the photodiode output power is monitored with a RF power meter. All these instruments can be controlled by a Labview program through GPIB cables. The bandwidth is measured by tuning the wavelength of the laser and recording the RF output power.

These two methods have advantage and disadvantages. In the setup with modulators, the frequency tuning step of the RF source can be <1 Hz, so it has high measurement resolution.

However, the measurement frequency range is usually limited by the bandwidths of the modulator and RF components. Therefore, it is suitable for low-bandwidth measurement which requires high frequency resolution. In the optical heterodyne setup, the frequency resolution cannot be high because it is difficult to control the optical frequency precisely by changing the laser temperature. For example, at 1550 nm, wavelength error of 0.008 nm means 1 GHz difference in the frequency domain. However, the beat frequency can be easily tuned from DC to several hundred GHz, so it is suitable to measure devices with estimated bandwidth of tens or hundreds of GHz.

2.1.3 Photodiode nonlinearity

Linearity describes whether the output of the photodiode is directly proportional to its input or keeps the same waveform as its input [2.6-2.8]. Due to the nonlinearity of the photodiodes, there is some distortion in the output waveform. In the frequency domain, that means new frequencies are generated. Nonlinearity of the photodiode is important for applications such as analog photonic link [2.9] and optoelectronic oscillators [2.10].

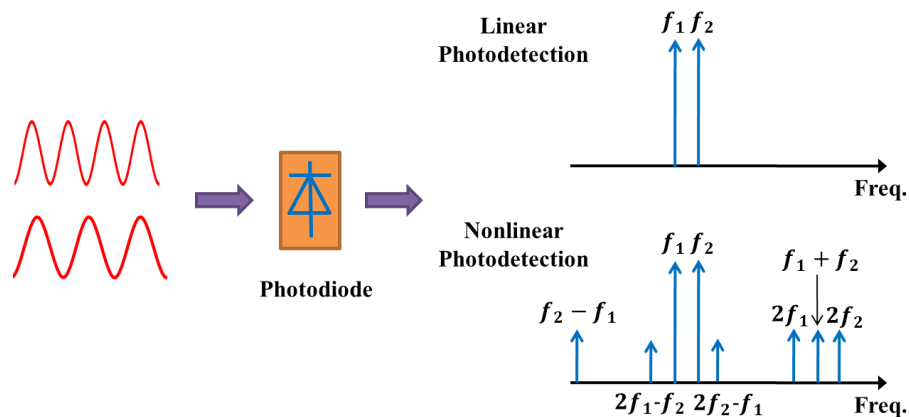


Figure 2-4. A comparison between linear and nonlinear photodetection.

Fig. 2-4 shows a comparison between linear and nonlinear photodetection. Two intensity-modulated light sources are incident on the photodiode. In the case of ideal linear photodetection,

there are only two fundamental frequencies (f_1 and f_2) in the output electrical spectrum. If there are nonlinearities in the photodetection, some intermodulation distortion (IMD) will be generated. Since the IMD2 frequencies are far away from the signal frequencies, they can be easily filtered out with a bandpass filter. The IMD4 and higher-order intermodulation distortion are usually much weaker than lower order harmonics. Typically, for photodiodes, the nonlinearity lines of most interest are IMD3 at $2f_1 - f_2$ and $2f_2 - f_1$. These two harmonics are close to signal frequency and cannot be filtered out easily. Also, they increase with input power three times faster than the signal frequency because they are mixing products. Therefore, IMD3 usually plays an important role in the characterization of photodiode nonlinearity.

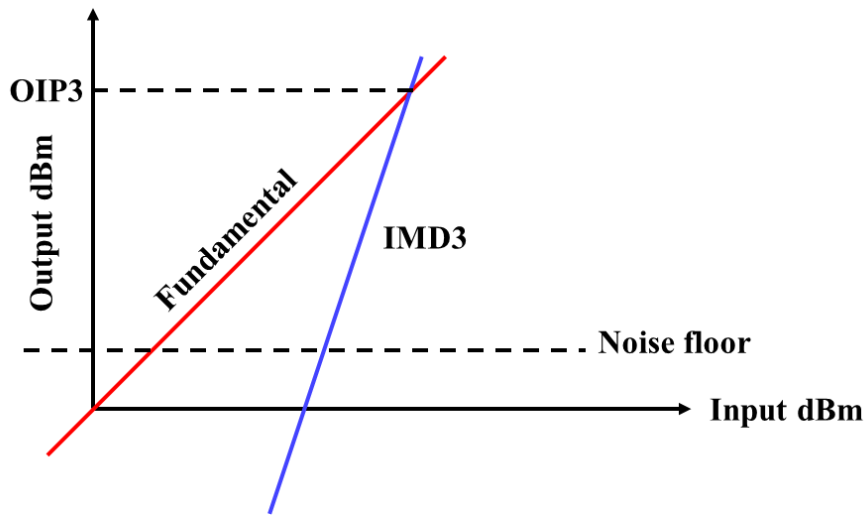


Figure 2-5. Definition of OIP3.

The 3rd-order output intercept point (OIP3) is a figure of merit that is widely used to characterize photodiode nonlinearity. As shown in Fig. 2-5, the horizontal axis is the input power of fundamental frequency and the vertical axis is the output RF power. The red line is the output power at the fundamental frequency and the blue line is that of IMD3. Both are measured in units of dBm. In theory, the red line will have a slope of 1 and the slope of the blue line is 3. The intercept

of linear extrapolations of these two lines is defined as the 3rd-order output intercept point. In literature, OIP3 usually refers to the corresponding power value (in dBm) on the vertical axis. A higher OIP3 indicates higher linearity.

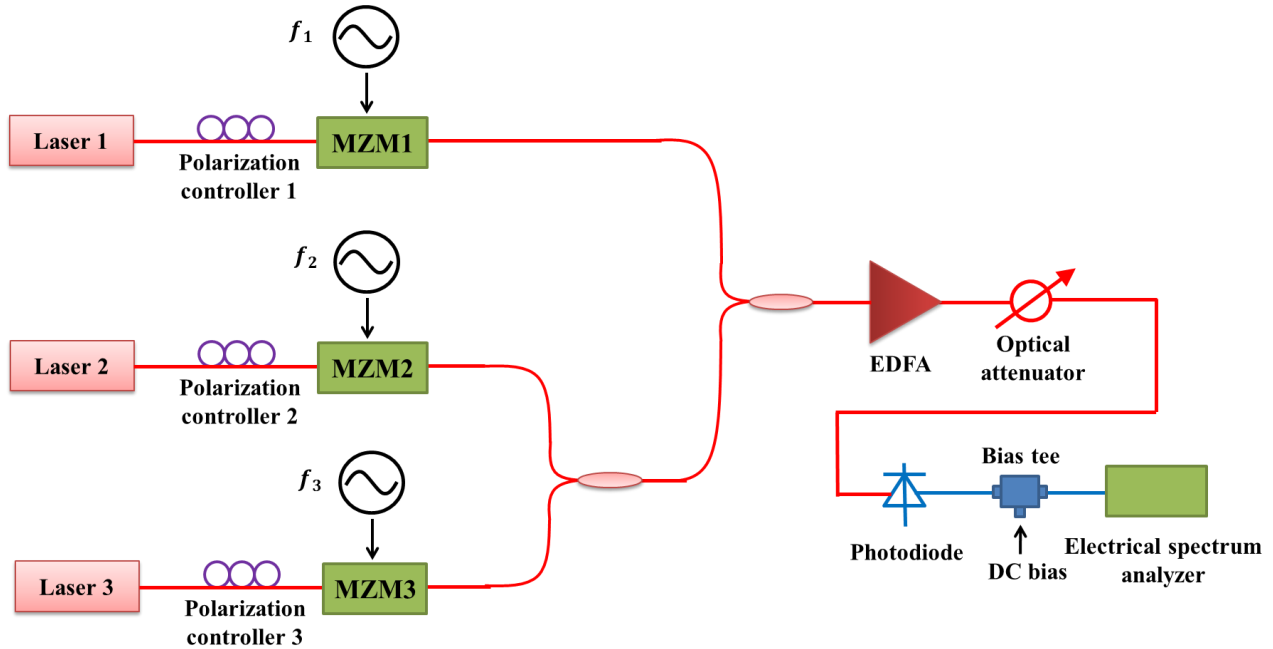


Figure 2-6. Three-tone OIP3 measurement setup.

Fig. 2-6. shows the three-tone OIP3 measurement setup [2.11]. Light from three lasers is intensity-modulated by three MZMs and the modulation frequencies are f_1 , f_2 , and f_3 , respectively. Three polarization controllers are used before the MZMs to achieve the largest modulation efficiency because the input of an MZM is polarization-sensitive. These light signals are further combined by two 3 dB optical couplers, amplified by an EDFA and then detected by the photodiode. An optical attenuator is used after the EDFA to adjust the photocurrent. After a bias tee, the generated electrical is measured with an electrical spectrum analyzer. During the measurement, the output power of the RF source needs to be set properly to ensure that, f_1 , f_2 , and f_3 in the ESA have the same power level. The OIP3 can be calculated by measuring the power

of IMD3 ($f_1 + f_2 - f_3$, $f_1 + f_3 - f_2$, and $f_2 + f_3 - f_1$) at different power levels of the fundamental frequency, doing linear fitting, and then finding the intercept point. Assuming that the curve for IMD3 always has a slope of 3 (which is usually not exactly 3 because of the measurement error), the OIP3 can also be approximately calculated as:

$$\text{OIP3} = P_f + \frac{P_f - P_{\text{IMD3}}}{2} \quad (2.12)$$

where P_f and P_{IMD3} is the power at the fundamental frequency and the power of IMD3.

In the OIP3 measurement, there are several points that require attention. First, the frequency of the RF signals f_1 , f_2 , and f_3 need to be chosen properly to make sure that the IMD3 will not overlap with other intermodulation distortion products. For example, if $f_1 = f_2$, then IMD3 $f_1 + f_2 - f_3$, $2f_1 - f_3$ and $2f_2 - f_3$ will occur at the same frequency and the measured OIP3 will be much lower than actual value. Second, in the ESA, the resolution bandwidth (RBW) will influence the noise floor. In the case of very weak IMD3, the RBW needs to as high as possible to lower the noise floor, otherwise the IMD3 will be buried in the noise. Third, due to the nonlinearity of the RF components in the ESA, the ESA itself will generated another IMD3. In most cases, the IMD3 generated by the ESA is much stronger than that generated by the device under test. To solve this problem, an attenuator is used in the input of the ESA (or use the internal attenuation in the ESA, or both). Since the IMD3 decreases three times faster than the fundamental frequency, that attenuation will make the IMD3 generated by the ESA much weaker than the IMD3 generated by the photodiode, and the influence of the ESA nonlinearity can be avoided. The attenuation value needs to be carefully optimized. If it is too small, the ESA nonlinearity cannot be effectively avoided. But if it is large, the attenuated IMD3 may be lower than the noise floor and cannot be

measured. It should be noted that, when calculating OIP3, the attenuation from the photodiode to the ESA (induced by the bias tee, cable, attenuators and ESA internal attenuation) also needs to be added to the power value read from the ESA.

2.1.4 S11 of the photodiode

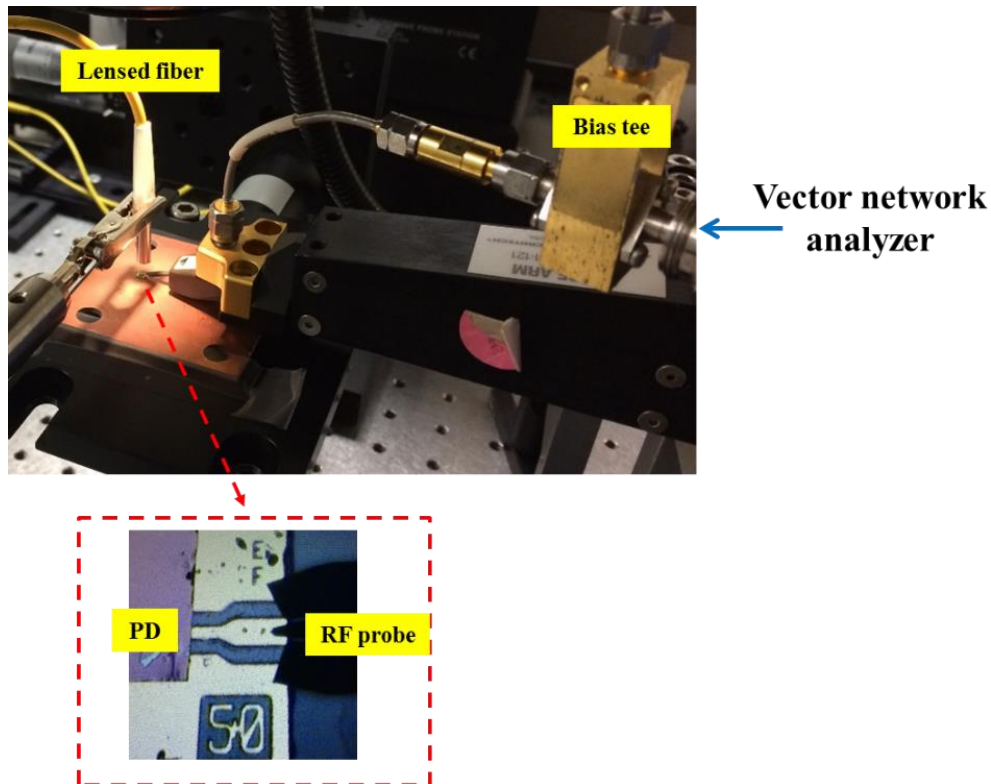


Figure 2-7. S11 measurement setup.

Scattering parameters (S-parameters) describe the input-output relationship between different ports in electrical networks. For photodiodes, the most important S-parameter is S11, which is the ratio of the reflected wave to incident wave at the RF output port [2.12, 2.13]. Fig. 2-7 shows the S11 measurement setup. A flip-chip bonded device is measured by a vector network analyzer (VNA) with a ground-signal-ground (GSG) probe. A bias tee is inserted between them to provide bias voltage and to measure photocurrent. The incident light comes from a lensed fiber above the

device, which enables us to measure S11 in the case of illumination.

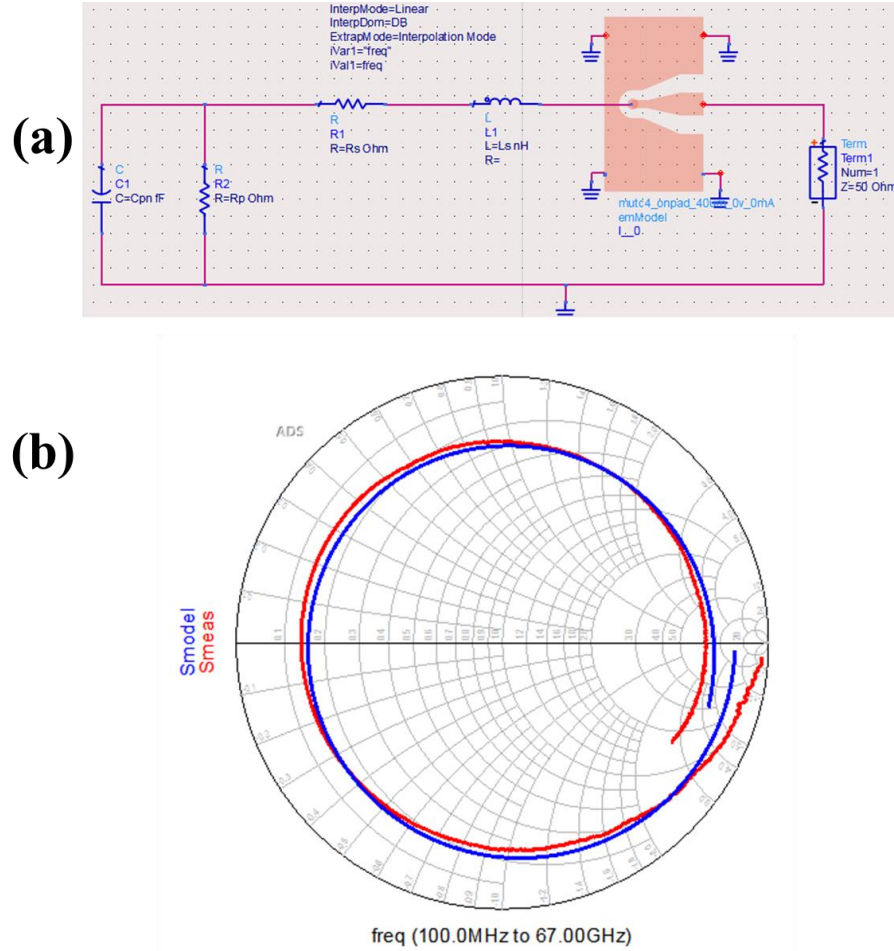


Figure 2-8. S11 parameter fitting: (a) Equivalent circuit in Keysight ADS software; (b) fitting result.

S11 measurement results are usually used to estimate the equivalent circuit of the photodiode by parameter fitting. Fig. 2-8 (a) shows the simulation model built with Keysight ADS software. Both the RC equivalent circuit and co-planar waveguide (CPW) pads are included. During the fitting process, the value of resistance, inductance and capacitance is tuned to make S11 curves of the simulation model coincide with the measured S11 curves. Fig 2-8 (b) shows an example of the fitting results. The blue curve is the simulated S11 and the red one is the measured result. They agree well.

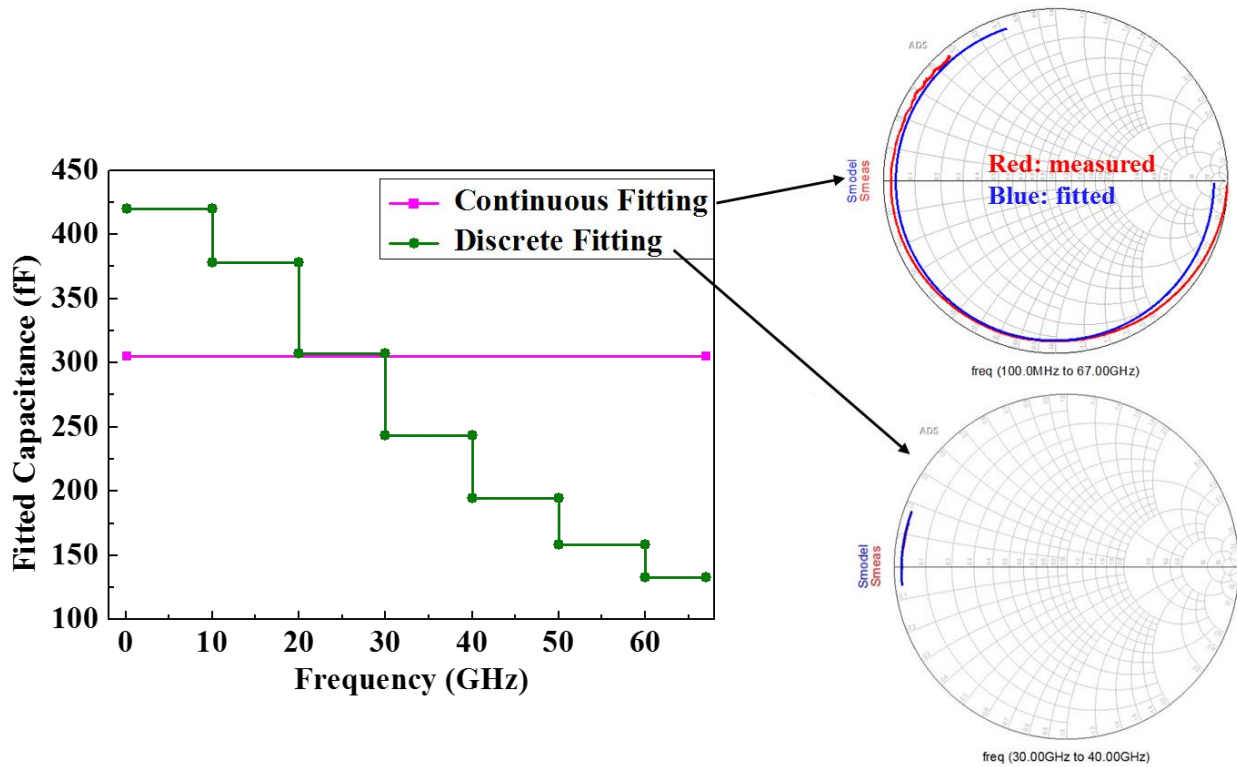


Figure 2-9. Comparison between the fitted capacitance for different frequency range.

Fig. 2-9 shows the fitted junction capacitance for a $40\ \mu\text{m}$ MUTC photodiode at bias voltage of -1 V. For comparison, two methods are used. In the case of “Continuous Fitting”, the S11 curve is fitted in the frequency range of 100 MHz to 67 GHz. In the case of “Discrete Fitting”, the curve fitting is performed with a step of ~ 10 GHz from 100 MHz to 67 GHz. The results in Fig. 2-9 show that different frequency ranges lead to different fitting results, which is caused by the frequency-dependence of the junction capacitance [2.14]. The measured junction capacitance is frequency dependent. Therefore, to get a more accurate result, the frequency range cannot be too large in the parameter fitting.

2.1.5 AM-to-PM Coefficient

The AM-to-PM conversion coefficient α is used to characterize the amplitude-variation-induced phase change. It is defined as:

$$\alpha = \frac{\Delta\phi}{\Delta P / P} \quad (2.13)$$

where $\Delta\phi$ is the microwave phase change caused by the relative optical power fluctuation $\Delta P / P$ [2.15]. Assuming that the photodiode responsivity is independent of incident optical power, the optical power fluctuation $\Delta P / P$ is equivalent to the photocurrent fluctuation $\Delta I / I$. Eq. (2.13) can be re-written as:

$$\alpha = \frac{\Delta\phi}{\Delta I / I} = I \cdot \frac{\Delta\phi}{\Delta I} \quad (2.14)$$

Eq. (2.14) shows that the AM-to-PM coefficient is directly related to the slope of phase-photocurrent curve. α becomes 0 at each pole of the phase-photocurrent curve.

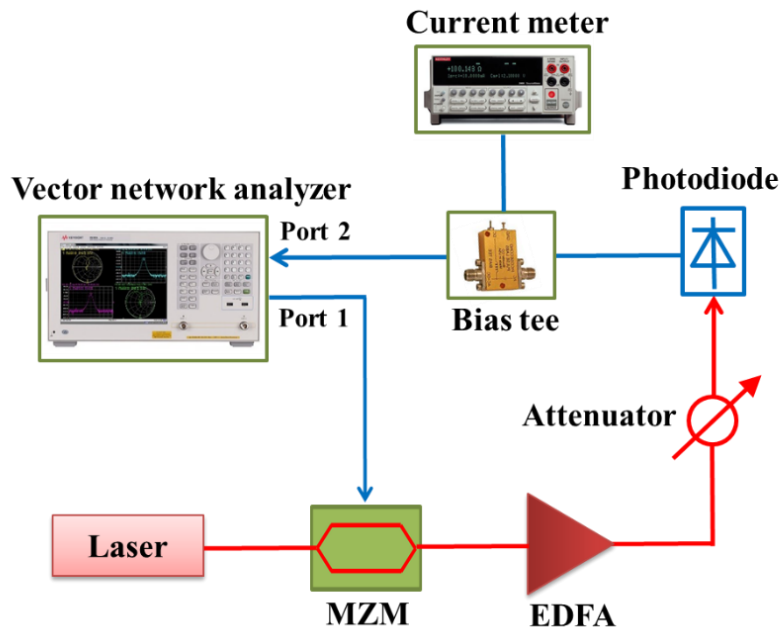


Figure 2-10. AM-to-PM measurement setup.

Fig. 2-10 shows the AM-to-PM measurement setup. Light from a laser at 1550 nm is intensity-modulated by a Mach-Zehnder modulator, amplified by an EDFA, and focused onto the photodiode with a lensed fiber. A mechanical variable optical attenuator is inserted after the EDFA to adjust the photocurrent, which is monitored by a current meter through a bias tee. The vector network analyzer (VNA) operates in CW mode with output frequency of 15 GHz. The signal from Port 1 of the VNA is used to drive the MZM and the RF signal from the photodiode is received by Port 2. The AM-to-PM measurement is conducted by tuning the optical attenuator and the S21 phase is monitored with the VNA.

2.2 Different photodiode structures

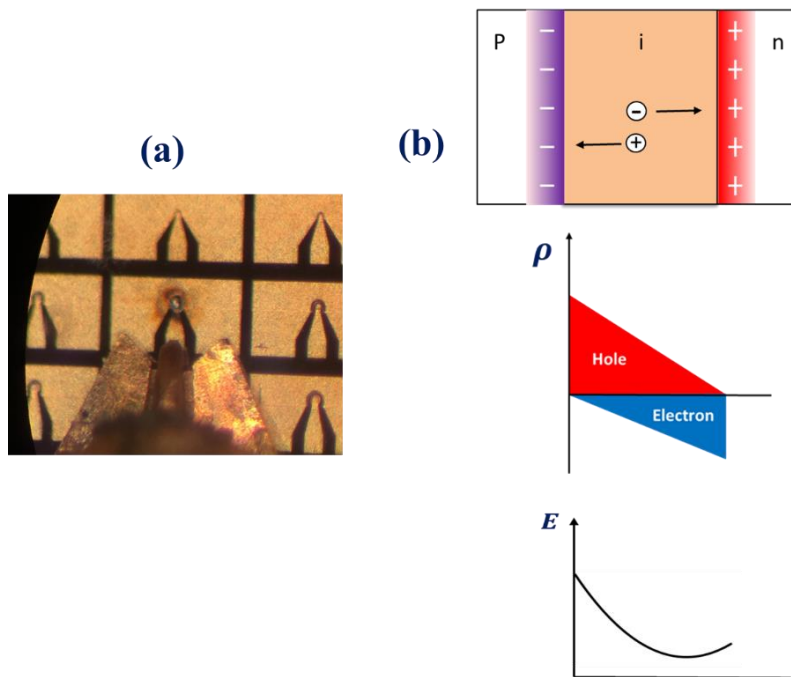


Figure 2-11. (a) Photos of a photodiode killed by thermal energy; (b) Space charge effect at large photocurrent.

In addition to responsivity and bandwidth, the power-handling capability of the photodiode is important for some applications. In an analog photonic link, a high-power photodiode enables high link gain, low noise figure, and high dynamic range [2.17]. It is also beneficial for generating ultra-

low-noise microwave signals because the noise floor is also limited by the power-handling capabilities of the photodiodes in these systems [1.37]. As shown in Fig. 2-11, usually there are two limitations on the RF output power. One is thermal failure [2.18]; another is the space charge effect [2.19]. Fig. 2-11 shows the principle of the space charge effect. At high incident optical power, the photo-generated holes and electrons will accumulate in the depletion region. Owing to the spatial distribution of the photo-generated carriers, there will be another electric field in the depletion layer that opposes the electrical field created by the applied bias. When the density of carriers increases to a certain level, the field generated by space charge is so strong that the overall electric field can drop below the level required to maintain the saturation velocity, which slows down the carrier transport and further promotes the carrier accumulation. As a result, the RF output power drops at large photocurrent.

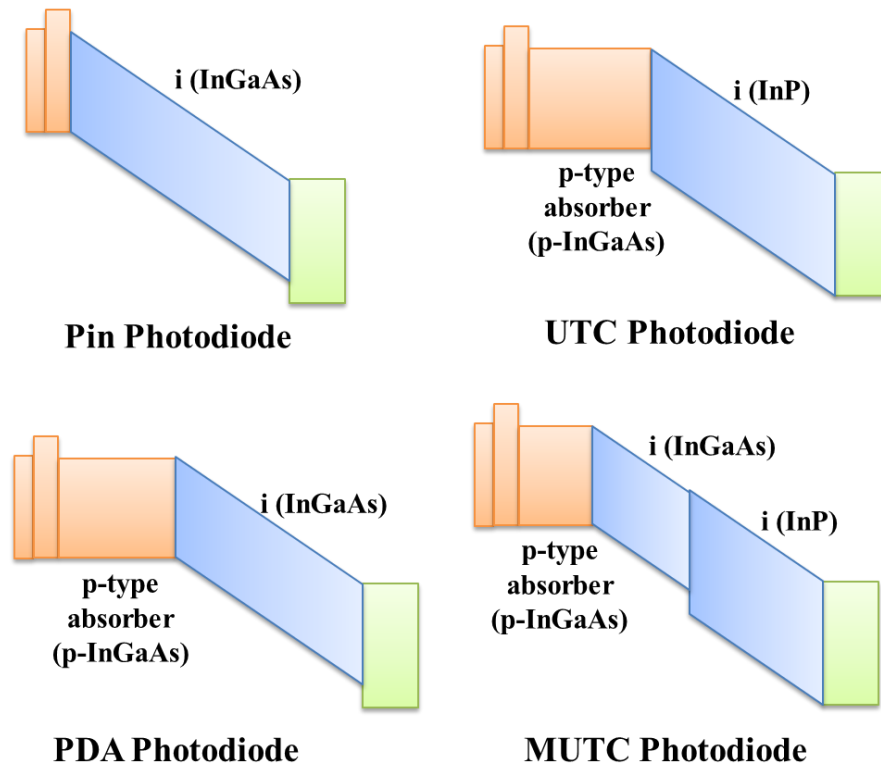


Figure 2-12. Different photodiode structures.

For photodetectors, both the epitaxial layer arrangement and electronic output design will influence its performance. As shown in Fig. 2-12, the simplest structure is a p-i-n photodiode. However, the p-i-n photodiode cannot generate very high RF power due to the space charge effect. Several photodiode structures have been proposed to achieve high saturation photocurrent and large bandwidth, including the partially depleted absorber (PDA) [2.20], the dual-depletion pin photodiode [2.21], uni-traveling-carrier (UTC) photodiodes [2.22], and modified UTCs (MUTCs) [2.23]. In addition, different electronic output designs, such as the travelling-wave design [2.24], integration with a horn antenna [2.25], and linear cascade of UTC-photodiodes [2.26], have also been used to extend the bandwidth or improve the output power.

In photodiodes, both electron and hole currents exist, but their balance can be adjusted by through design of the epitaxial layers. In UTC-photodiodes, an undepleted p-type absorber is used and only electrons transit the depletion region. Holes generated in the absorber are collected directly since they are majority carriers and are very close to the cathode. Since the drift velocity of electrons is higher than that of holes at the same electrical field, this design leads to a fast photoresponse and a high saturation current. In addition, compared with the p-i-n structure, there are two advantages of using InP as drift layer. First, the saturation velocity of electrons in InP is higher than that in InGaAs, which helps to increase the transit-time-limited bandwidth. Second, the larger band gap of InP is also beneficial for reducing the dark current.

In the UTC structure, a thin absorber results in a short response time for electron injection, but also results in a relatively low quantum efficiency. Therefore, there is a tradeoff between response speed and efficiency. This can be addressed somewhat by incorporating a depleted absorber and other layers, a structure that is referred to as the modified UTC (MUTC). The additional depleted absorber is also beneficial in reducing the junction capacitance and increasing the RC-limited

bandwidth. Using an MUTC photodiode flip-chip bonded on diamond, a 1.8 W RF output power at 10 GHz and 60 % power conversion efficiency (PCE) at 6 GHz have been achieved [2.27].

Chapter 3. Fabrication process

3.1 P-mesa etch

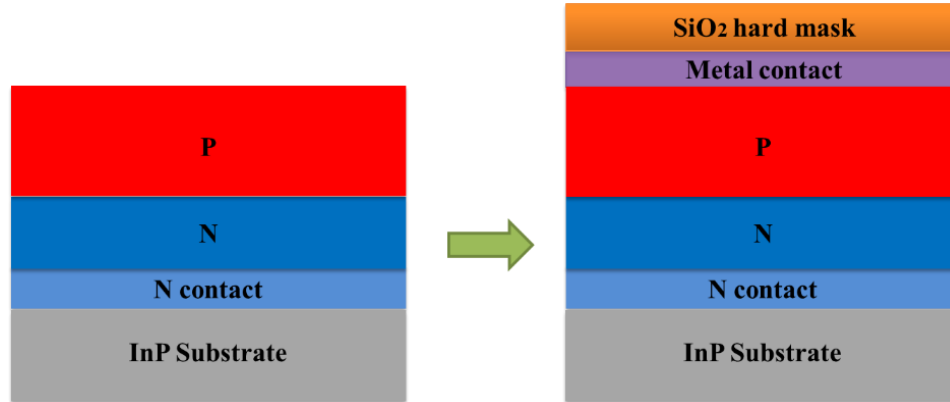


Figure 3-1. Deposition of p contact metal and silicon dioxide hard mask.

As shown in Fig. 3-1, the fabrication process starts with the deposition of p contact metal. Since the bandwidth of a photodiode is partly limited by the RC response time, the p contact resistance needs to be as low as possible to achieve a large RC-limited bandwidth. Metal layer stacks of Ti/Pt/Au/Ti are deposited on the heavily-doped InP contact layer by an electron-beam evaporator. Their thickness is 20 nm, 30 nm, 50 nm and 10 nm, respectively. The titanium layers are used to achieve good adhesion and platinum works as a “block layer” to prevent gold from diffusing to the III-V material and inducing defects.

After metal deposition, the wafer is cleaned and put into a plasma-enhanced chemical vapor deposition (PECVD) system for growth of silicon dioxide, which is used as the hard mask during mesa etch. The silicon dioxide is generated by the reaction between SiH_4 and N_2O at 285 centigrade in PECVD. SiH_4 is supplied diluted in helium with percentage of 2% and the ratio of $\text{SiH}_4/\text{N}_2\text{O}$ is 50, which will influence the refractive index and deposition rate of silicon dioxide [3.1].

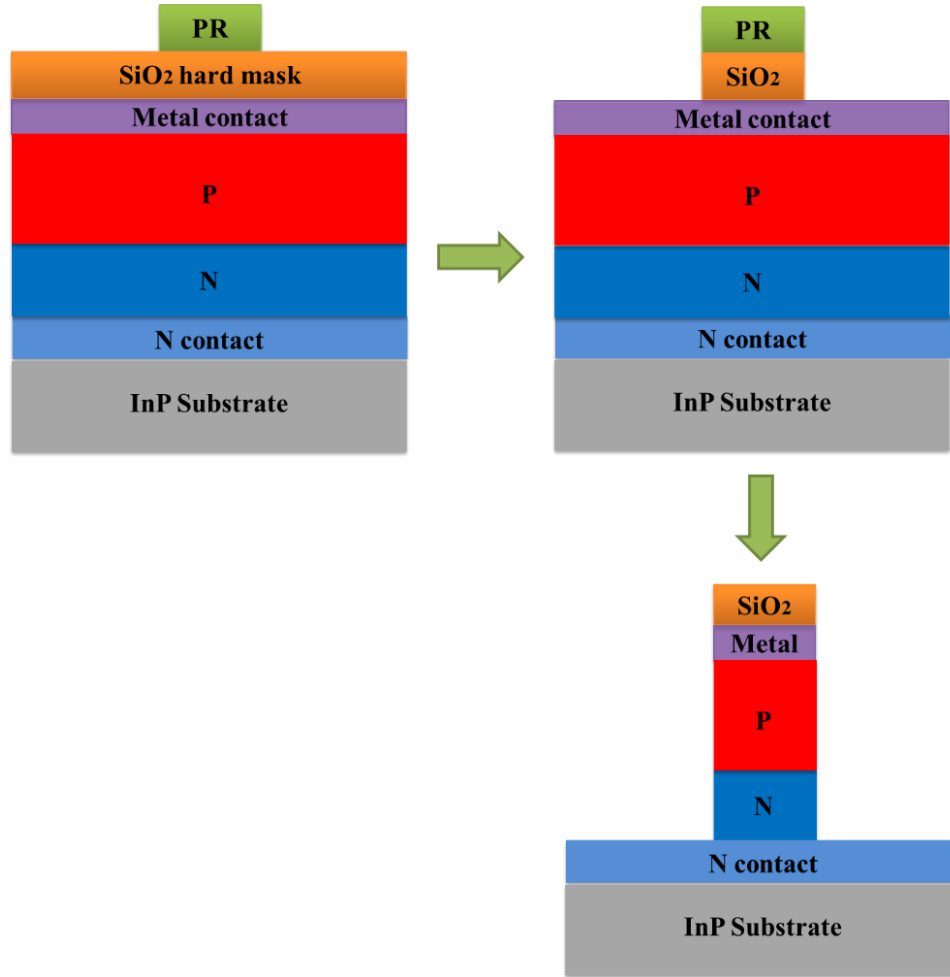


Figure 3-2. Process of p-mesa etch (PR: photoresist).

Fig. 3-2 shows the process of p-mesa etch. The first step is photolithography. After photolithography, the p-mesa pattern on the mask is transferred to the photoresist. Usually photoresist AZ5214 is used and the spin speed is 3000 rpm in spin coating. After developing in AZ300MIF for 30 second, the thickness of residual photoresist is $\sim 1.7 \mu\text{m}$.

The next step is SiO₂ hard mask etching. SiO₂ can be etched by buffered oxide etch (BOE), i.e. wet etching. Compared with dry etching, wet etching will be much easier but it is isotropic, which means there will be some undercutting after wet etching. For devices with small size, that

undercutting may be a big issue. Therefore, dry etching is preferred for the fabrication of small devices. Dry etching of SiO_2 can be done with inductively coupled plasma (ICP) etch. It is found that CHF_3 plasma has very good selectivity in etching SiO_2 relative to photoresist. It should be noted that, the wafer should have good thermal dissipation and cannot be dry etched continuously for a long time ($> 20\text{min}$), otherwise there may be some scorched photoresist or some other reaction products on the wafer that cannot be removed easily.

The last step is to define the p-mesa with ICP etching. Both the metal contact and the III-V material can be etched by Cl_2/N_2 plasma. The ICP power varies from 100-500 W, depending on the expected etch rate, and the ratio of etching rates for SiO_2 and III-V material is about 1:2.5 to 1:5, which depends on the doping concentration of the III-V material.

3.2 N-mesa etch

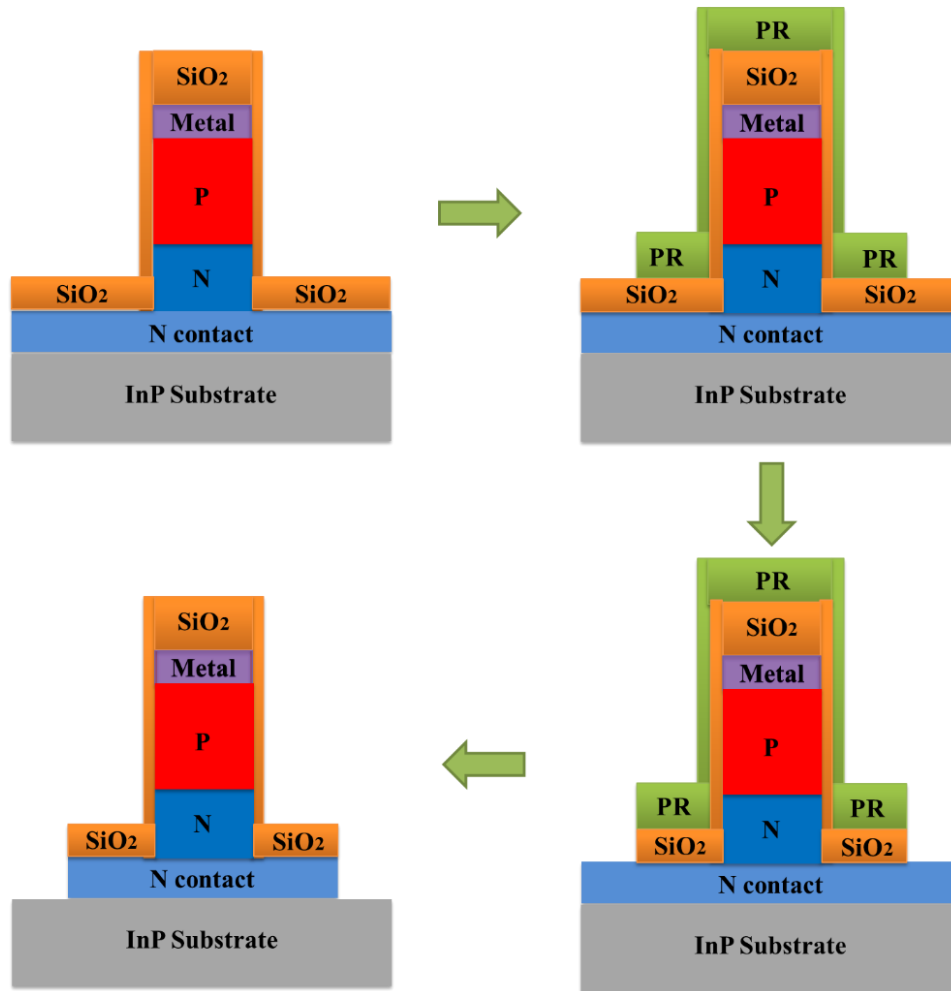


Figure 3-3. Process of n-mesa etch.

The n-mesa etch process is shown in Fig. 3-3. Similar to the p-mesa etch, the n-mesa etch consists of four steps: growth of SiO_2 , n-mesa photolithography, SiO_2 hard mask etching, and III-V material etching. The III-V material is etched to the InP substrate to make sure that each photodiode is isolated in order to reduce the parasitic capacitance. The SiO_2 in the sidewall of p-mesa also provides good passivation and is beneficial for reducing dark current caused by surface leakage.

3.3 N-metal deposition

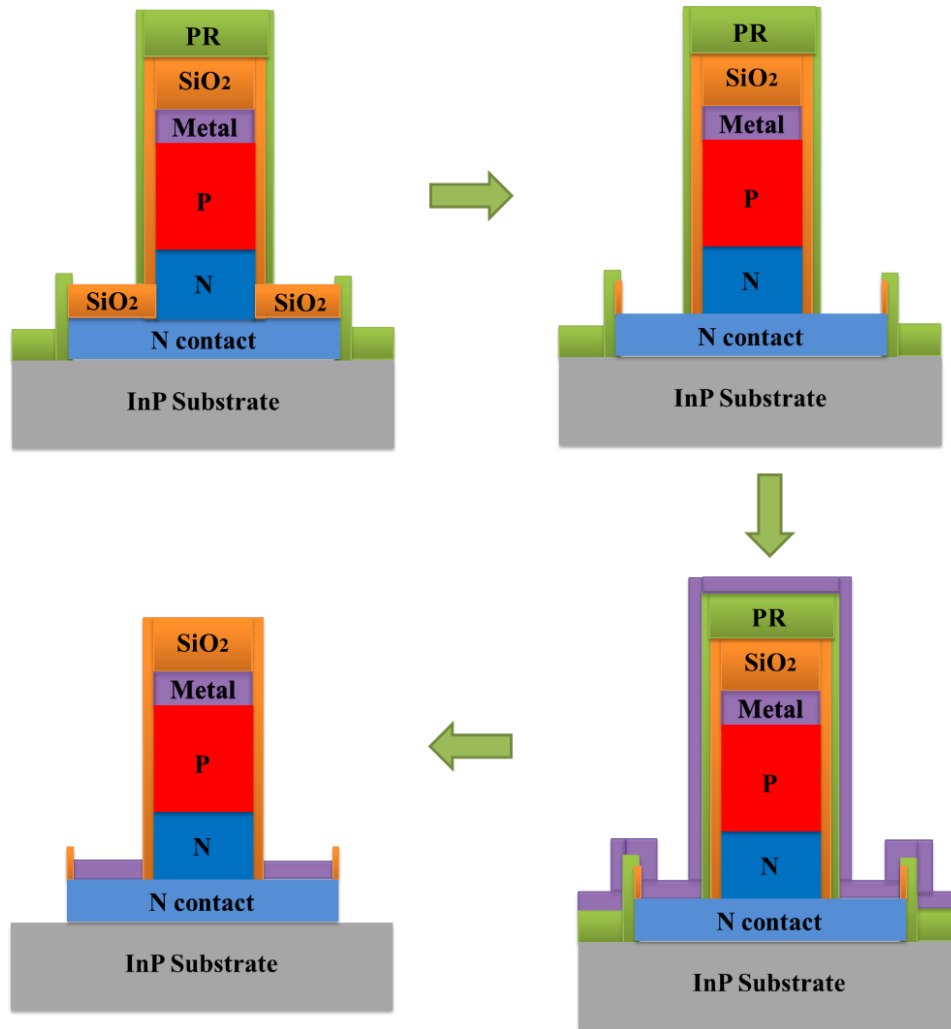


Figure 3-4. Process of open n-contact and n-metal deposition.

The next step is open the n-contact and n-metal deposition, which is shown in Fig. 3-4. After photolithography, the wafer is cover by photoresist except the n-mesa. Then the residual SiO_2 is etched by BOE; the etching rate is approximately 100 nm/30s. Then the AuGe/Ni/Au metal stacks are deposited on the n-contact layer by E-beam evaporation and their thicknesses are 30 nm, 20nm and 80 nm, respectively. AuGe forms a good ohmic contact on n-doped InP [3.2] and nickel functions as an adhesion layer. The last step is lift-off. The wafer soaks in acetone with ultrasonic for several minutes. Then all the metals and photoresist are removed except the metal on the n-contact layer.

3.4 Open P-contact

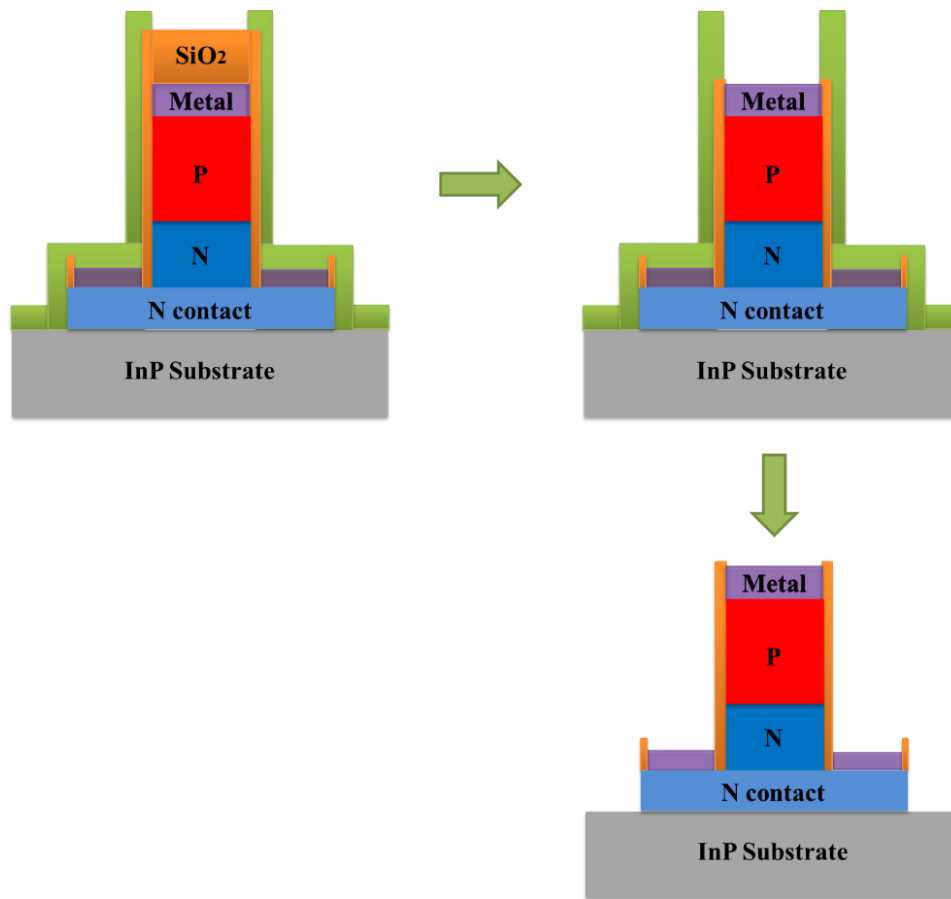


Figure 3-5. Process of open p-contact.

The next step is to open the p-contact layer. After n-metal deposition, the p-metal is still covered by SiO₂. After the first step of lithography, only the p-mesa is not covered by photoresist, and then the SiO₂ can be etched by dry etching or wet etching. For dry etching, the etch time needs to be carefully controlled, because over-etching may also remove the metal contact. For wet etching, undercutting cannot expand to the edge of the p mesa, otherwise the SiO₂ passivation in the sidewall will also be etched, which may lead to higher dark current. In the end, the photoresist can be removed by acetone and then the photodiodes are ready for current-voltage testing.

3.5 Other steps

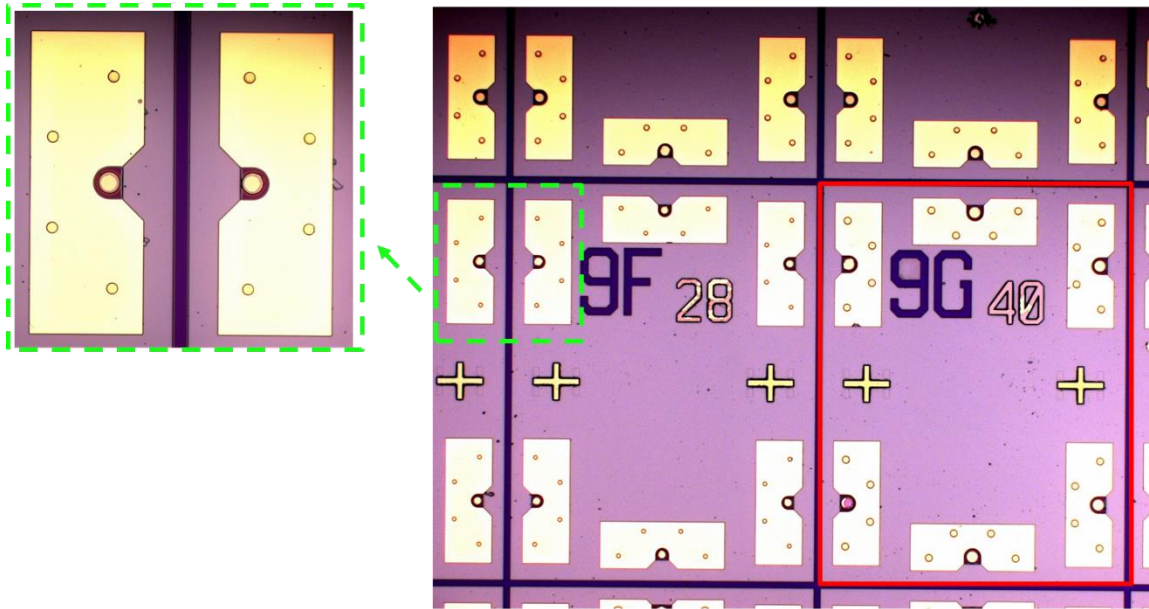


Figure 3-6. An example of the wafer before dicing.

After IV testing, there are several steps before the photodiodes are ready for other measurements. First, gold-plating is needed to increase the thickness of the metal contact and make it higher than the SiO_2 surrounding it on the p-mesa, which can be considered as preparation for flip-chip bonding. Then the backside of the wafer is polished and coated with SiO_2 to reduce light scattering and reflection. Usually a quarter-wave layer is used for the AR coating, so the thickness of the SiO_2 is

$$T_{\text{SiO}_2} = \frac{\lambda}{4n_{\text{SiO}_2}} \quad (3-1)$$

where λ is light wavelength and n_{SiO_2} is the refractive index of SiO_2 . Following the AR coating, the wafer is diced into 1mmx3mm chips for flip-chip bonding. Fig. 3-6 shows an example of the fabricated wafer before dicing. As shown by the red box, there are 6 devices on each die.

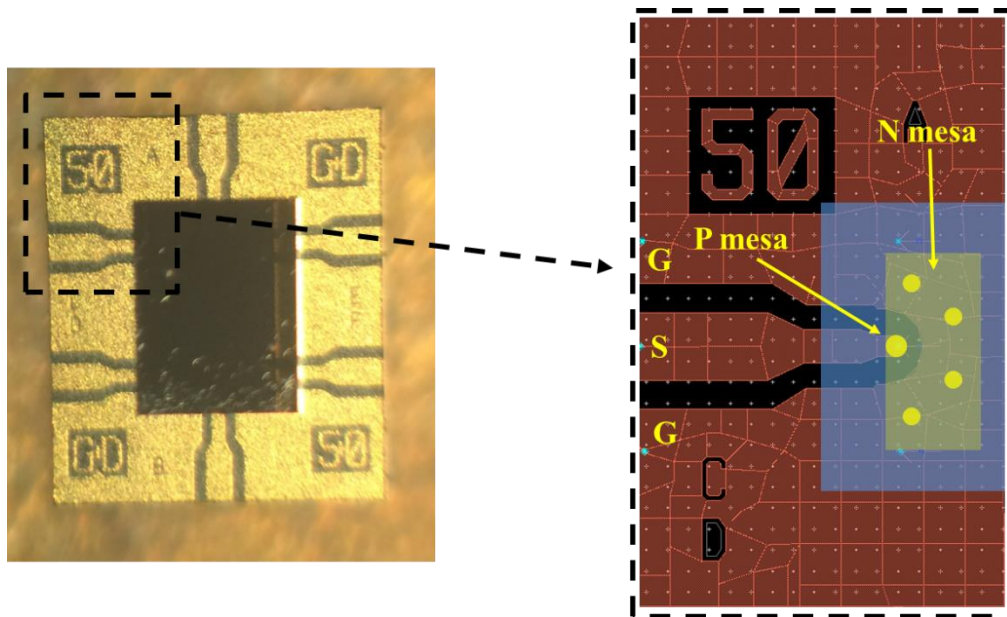


Figure 3-7. Device after flip-chip bonding.

The last step is to bond the diced chips with the RF pads on an AlN submount through gold-to-gold (Au–Au) thermo-compression bonding. Fig. 3-7 shows the diced chips after flip-chip bonding (6 devices on a chip). The right figure shows the principle of aligning the device with the ground-signal-ground (GSG) RF pads. Flip-chip bonding has several advantages. First, the photodiode is back-illuminated, which is beneficial to increasing the quantum efficiency. Light will “double-pass” the absorber because the un-absorbed light can be reflected by the p-metal and travel through the absorber again. Second, flip-chip bonding makes device characterization much easier. For photodiodes with a double mesa structure, high-frequency measurement is difficult, because the GSG probe cannot be put on the device directly, especially for devices with diameter $<10 \mu\text{m}$. The RF pads function as a connection between the photodiodes and the GSG probe, and make high-frequency characterization much easier. Third, flip-chip bonding is beneficial to the power-handling capacity of the photodiode. Thermal dissipation is one of the limiting factors for the maximum outpower of the photodiode [3.3]. The submount is much larger than the photodiode

and it is usually made of materials with good thermal conductivity, such as AlN and diamond. Therefore, heat generated in the photodiode will be dissipated quickly and thermal failure occurs at higher power level. By flip-chip bonding an MUTC photodiode on diamond, 1.8 W RF output power at 10 GHz has been achieved. [3.4]

Chapter 4. High-efficiency photodiodes for quantum information processing

4.1 Device design and fabrication

Contact layer InGaAs, P+, Zn, 2.0×10^{19} , 50 nm
InP, P+, Zn, 1.5×10^{18} , 100 nm
Grading InGaAsP, Q1.1, 2.0×10^{18} , 15 nm
Un-depleted absorber $\text{In}_{0.723}\text{Ga}_{0.277}\text{As}_{0.6}\text{P}_{0.4}$, Q1.3, Zn, 5.0×10^{19} , 450 nm
Un-depleted absorber $\text{In}_{0.723}\text{Ga}_{0.277}\text{As}_{0.6}\text{P}_{0.4}$, Q1.3, Zn, 6.0×10^{18} , 650 nm
Un-depleted absorber $\text{In}_{0.723}\text{Ga}_{0.277}\text{As}_{0.6}\text{P}_{0.4}$, Q1.3, Zn, 8.0×10^{17} , 850 nm
Un-depleted absorber $\text{In}_{0.723}\text{Ga}_{0.277}\text{As}_{0.6}\text{P}_{0.4}$, Q1.3, Zn, 1.0×10^{17} , 1050 nm
Grading InGaAsP, Q1.1, 1.0×10^{16} , 10 nm
Drift layer InP, Si, 2.0×10^{16} , 1500 nm
InP, n+, Si, 1.0×10^{18} , 100 nm
InP, n+, Si, 1.0×10^{19} , 500 nm
InP, semi-insulating substrate

Figure 4-1. Epitaxial-layer design of the high efficiency photodiode.

As noted in Chapter 1, high quantum efficiency (QE) photodiodes are key components in quantum information and quantum optical systems [1.13-1.15]. The epitaxial-layer structure of the high-efficiency photodiodes that I studied in this work is shown in Fig. 4-1. The epitaxial-layers were grown on semi-insulating InP substrate by metal organic chemical vapor deposition. The first layer grown is a 50 nm heavily n-doped ($1 \times 10^{19} \text{ cm}^{-3}$) contact layer. This is followed by a 100 nm ($1 \times 10^{18} \text{ cm}^{-3}$) n-doped InP layer. The drift layer is ($2 \times 10^{16} \text{ cm}^{-3}$) n-doped with a thickness of 1500 nm. After the drift layer, a 10 nm lightly doped InGaAsP quaternary layer is deposited to assist electron transport and suppress carrier accumulation in the heterojunction interface. To fully

absorb the light, the absorber is 3 μm -thick p-type $\text{In}_{0.723}\text{Ga}_{0.277}\text{As}_{0.6}\text{P}_{0.4}$, which is step-graded ($1 \times 10^{17} \text{ cm}^{-3}$, $8 \times 10^{17} \text{ cm}^{-3}$, $6 \times 10^{18} \text{ cm}^{-3}$, $5 \times 10^{19} \text{ cm}^{-3}$) to create a quasi-field that aids carrier transport. After the absorber, there is a 15 nm-thick InGaAsP grading layer to “smooth” the heterojunction discontinuity. Finally, the two top layers are a 100 nm $1.5 \times 10^{18} \text{ cm}^{-3}$ p-doped InP electron-blocking layer and a 50 nm heavily p-doped $2 \times 10^{19} \text{ cm}^{-3}$ InGaAs contact layer.

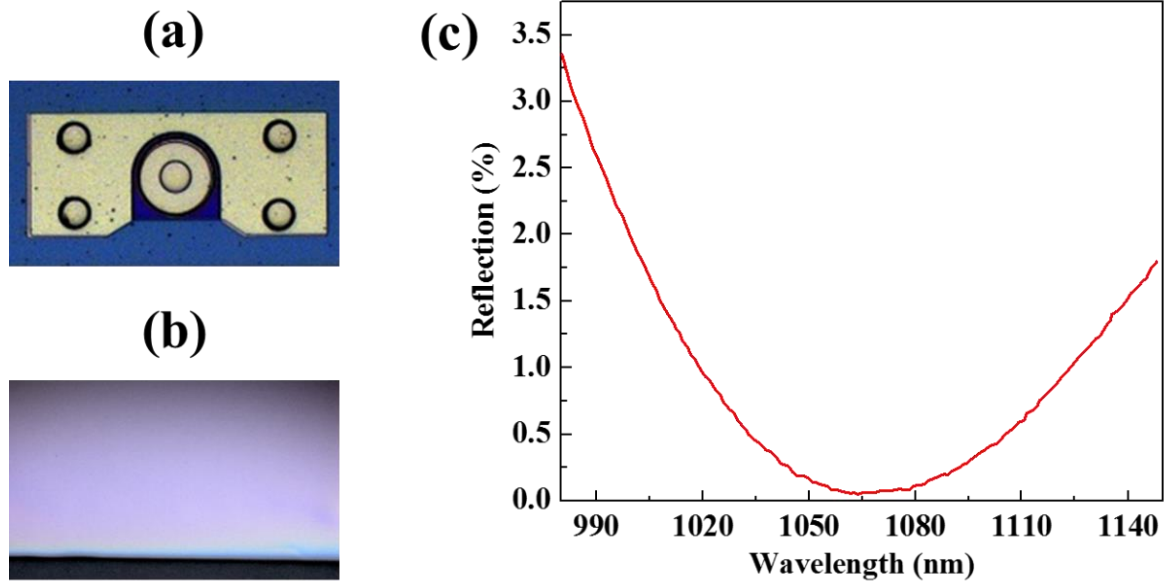


Figure 4-2. (a) Fabricated photodiode; (b) Backside surface after polishing; (c) Measured reflection coefficient of the anti-reflection coating.

Fig. 4-2 (a) shows a single high QE photodiode. The devices are fabricated as the process described in Chapter 3. SiO_2 hard mask is used for inductively coupled plasma (ICP) etching. A Ti/Pt/Au/Ti metal stack was deposited as p-type contact and the n-type contact is an AuGe/Ni/Au metal stack.

To reduce the scattering and reflection at the semiconductor/air interface, the backside of the device was polished and coated with an anti-reflection coating (ECI Inc.). Fig. 4-2 (b) shows the backside surface in the microscope after 6-hour polishing and Fig. 2-2 (c) is the measured reflection spectrum. As shown in Fig. 2-2 (c), the reflection spectrum is relatively narrow ($< 1\%$

from 1020 nm to 1125 nm) and centered at 1064 nm where the reflectivity is 0.012%.

4.2 Device Characterization

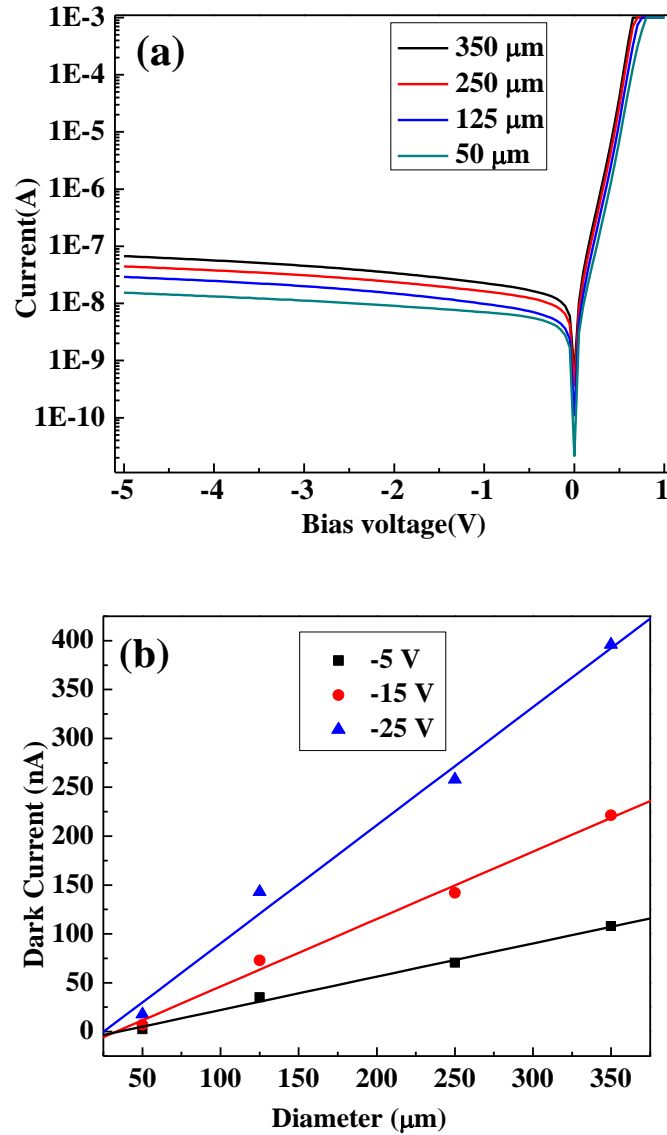


Figure 4-3. (a) Current-voltage curves for devices of different size; (b) Dark current versus device diameter at different bias voltage.

Four diameters were fabricated (50 μm, 125 μm, 250 μm, 350 μm). The corresponding current-voltage curves are shown in Fig. 4-3 (a). In quantum optical systems, the dark current of the photodiodes is one of the primary concerns. It needs to be as low as possible to reduce the

induced noise. It can be seen that, for all devices, the dark current at -5 V is less than 100 nA. Fig. 4-3 (b) shows the dark current versus device diameter. Since the dark current varies linearly with diameter, it can be concluded that surface leakage dominates.

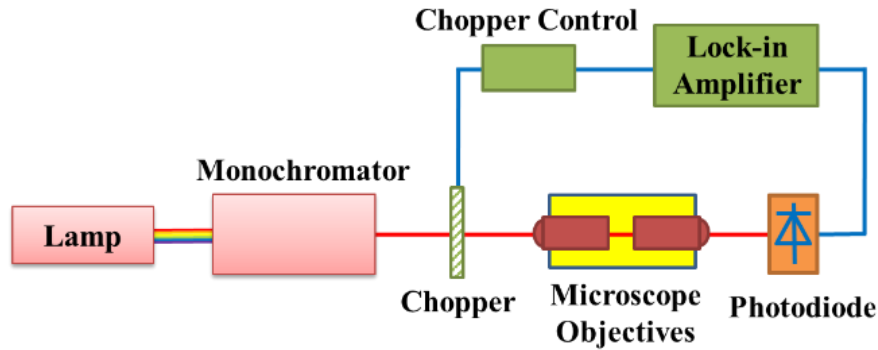


Figure 4-4. Quantum efficiency measurement setup.

Fig. 4-4 (a) shows the experimental setup for measurement of quantum efficiency. A tungsten-halogen lamp is used as a broadband optical source, followed by a monochromator to select different wavelength. A chopper is placed after the monochromator to provide intensity modulation (200-300 Hz). The light is collimated and then focused on the backside of the devices by two microscope objectives. Finally, the photocurrent is measured by a Stanford Research lock-in amplifier (SR-850).

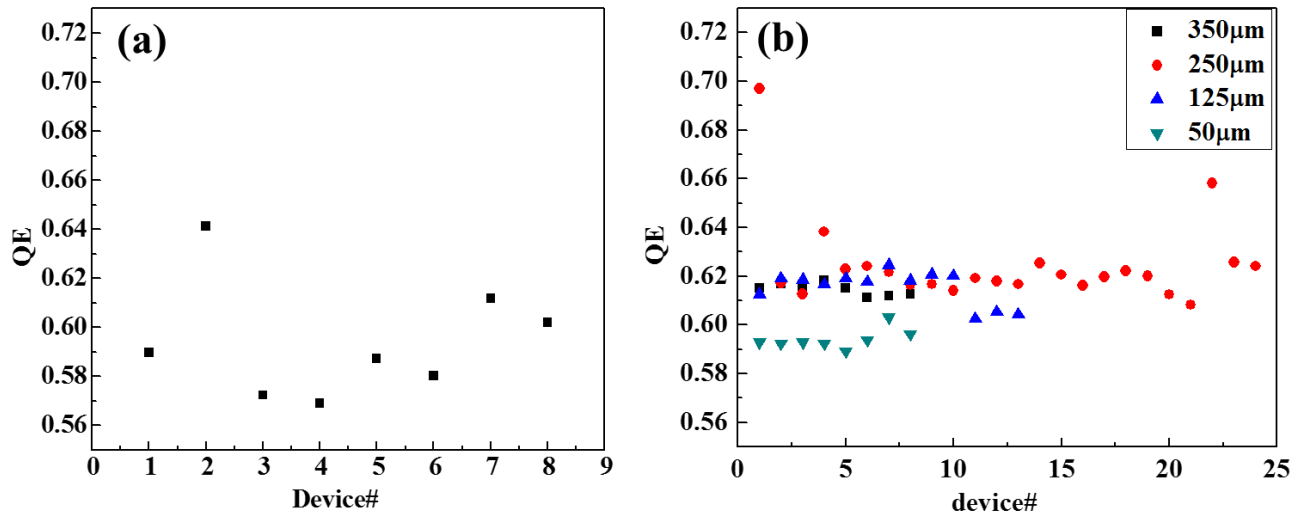
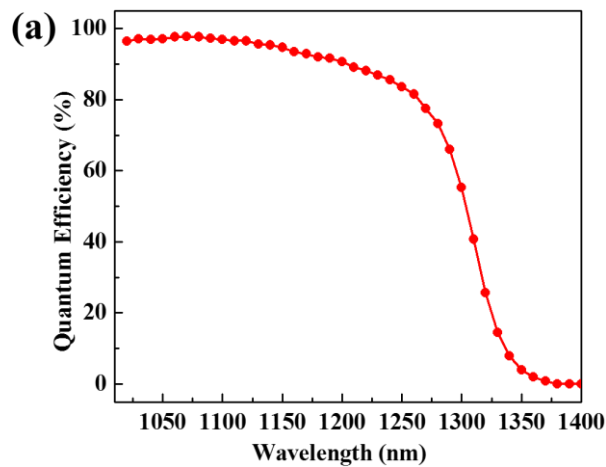


Figure 4-5. Comparison of the quantum efficiency before (a) and after (b) polishing.

Fig. 4-5 shows the measured quantum efficiency before (a) and after (b) polishing the backside of the photodiodes. There is no AR-coating in both cases. Before polishing, the average QE is 59.4 %, while that value is 61.5 % after polishing, indicating an increase of 2.1 percent is achieved.



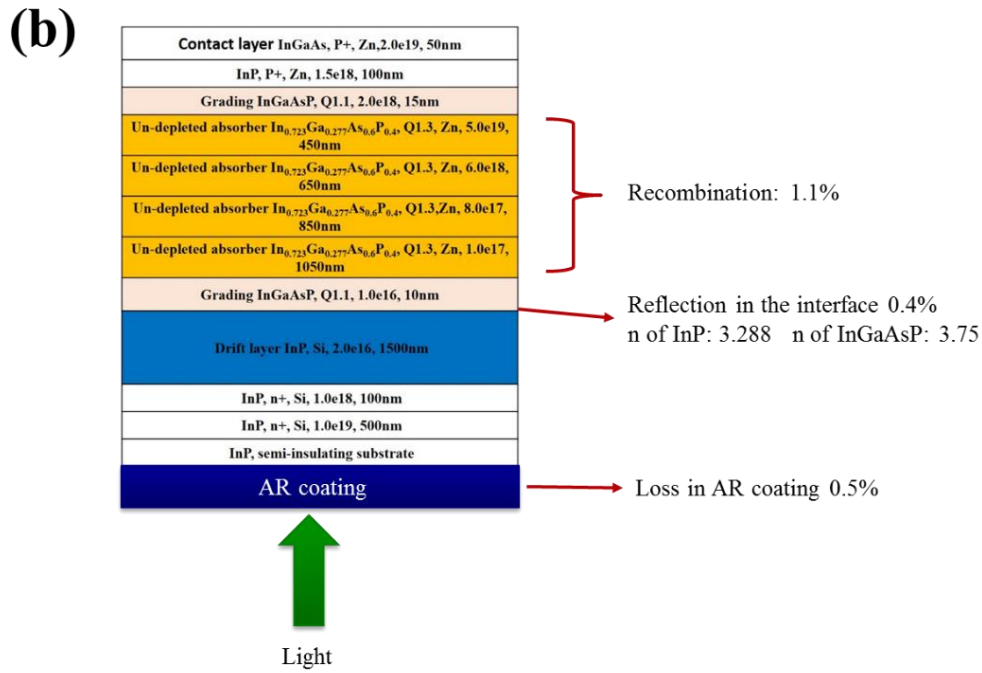


Figure 4-6. (a) Measured quantum efficiency at different wavelength; (b) Possible origins of QE loss.

As mentioned in Section 4.1, after polishing, the backside of the photodiode is coated with an anti-reflection coating, which theoretically will increase the quantum efficiency by ~30%. Fig. 4-6 (a) is the measured quantum efficiency of a 250 μm device at -5 V. The quantum efficiency is > 90% in the wavelength range 1000 nm to 1200 nm. At 1064 nm, the measured quantum efficiency is 98% \pm 0.8%. Fig. 4-6 (b) shows the possible origins of QE loss. Approximately 0.5% of the incident light is absorbed by the InP substrate, and 0.4% is reflected at the interface of InP drift layer and InGaAsP grading layer. Recombination in the absorber accounts for a loss of 1.1%. The band gap energy of the absorber material, In_{0.723}Ga_{0.277}As_{0.6}P_{0.4}, is 0.96 eV and the corresponding cutoff wavelength is 1290 nm. Therefore, the quantum efficiency decreases quickly when the wavelength increases from 1250 nm to 1350 nm. For wavelengths less than 1064 nm, the quantum efficiency decreases slowly due to the narrow-band anti-reflection coating. If a broader-band anti-reflection coating were used, the quantum efficiency at shorter wavelength should be similar to

that at 1064 nm.

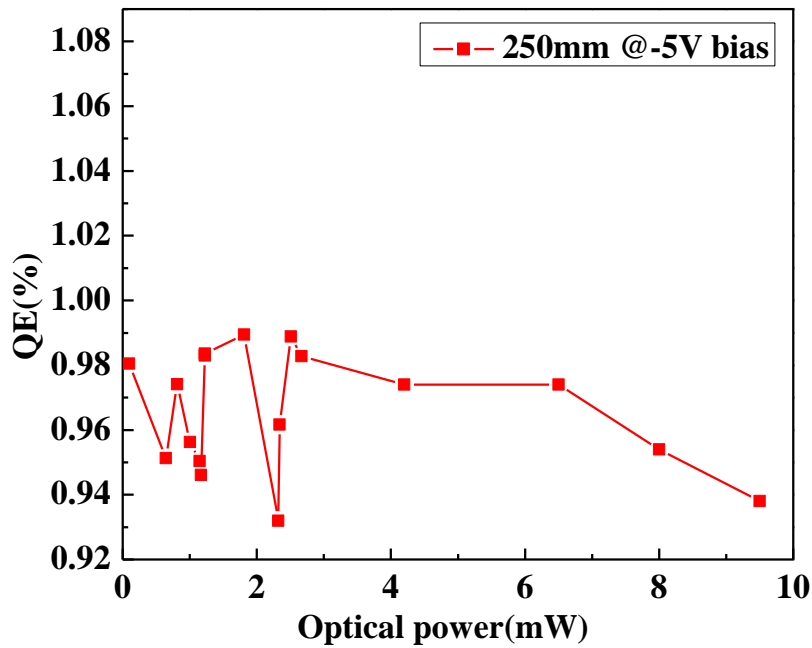


Figure 4-7. Measured quantum efficiency at higher incident optical power.

The quantum efficiency in Fig. 4-6 (a) is measured with a lamp as the optical source. Due to the broad output spectrum of the lamp, the optical power at 1064 nm is pretty low and the photocurrent is < 100 nA. The efficiency at 1064 nm has also been measured with a Nd:YAG laser as optical source (Fig. 4-7). When the optical power is below 6 mW, the quantum efficiency is still 98%. Above 6 mW average power, the quantum efficiency begins to decrease, which may be caused by the local saturation due to the small spot size ($10^{\mu m}$) of the lensed fiber. At 8 mW, the quantum efficiency is 95%.

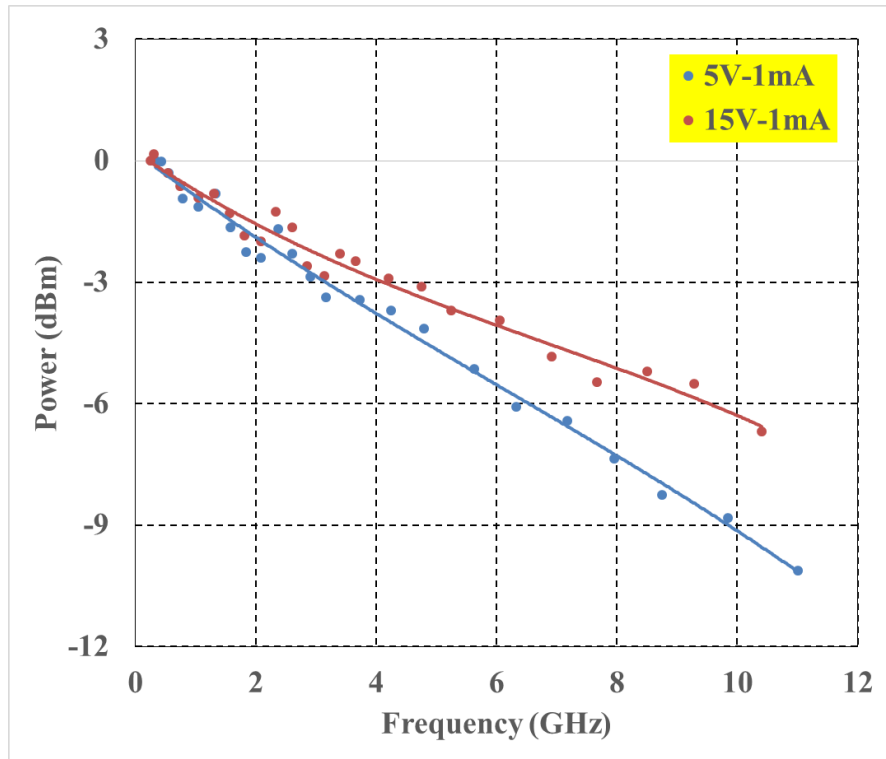


Figure 4-8. The measured bandwidth at different bias voltage.

To measure the bandwidth, the devices were flip-chip bonded onto an AlN submount. An optical heterodyne setup was used to measure the bandwidth. Similar to the setup in Fig. 2-3, light from two lasers at 1064 nm was combined by an optical coupler. One of the output signals from the optical coupler was directed to a commercial photodiode and an electrical spectrum analyzer to monitor the beat frequency. Another went to the high-efficiency photodiode through a lensed fiber. No optical power amplifier was used and the maximum power delivered to the photodiode is ~75 mW.

Fig. 4-8 shows the measured bandwidth of a 50 μm -diameter device at bias of -5 V and -15 V. The photocurrent was fixed at 1mA and the RF output power was normalized to 0 dBm. At bias voltage of -5 V and -15 V, the 3-dB bandwidth of 50 μm device is 3 GHz and 4 GHz, respectively. For 50 μm devices, the estimated RC-limited bandwidth is ~11 GHz, therefore they are transit-time limited. The results in Fig. 4-8 indicates that the photodiodes require high bias voltage to

maintain high electron velocity and achieve large transit-time limited bandwidth.

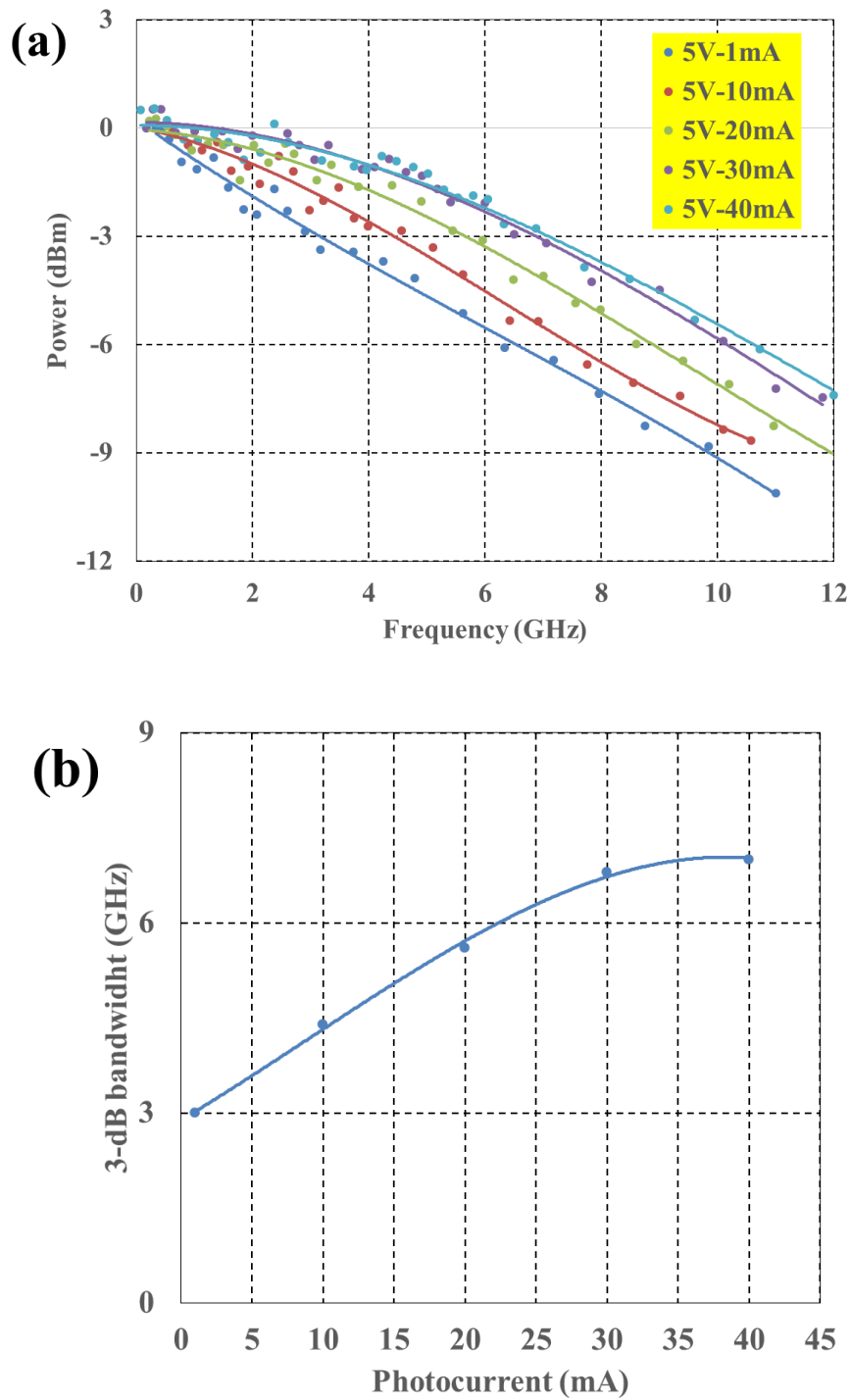


Figure 4-9. Measured bandwidth of 50 μm devices at different photocurrent.

Fig. 4-9 shows the measured bandwidth of a 50 μm -diameter device versus photocurrent. Fig.

4-9 (a) shows the RF output power at different frequency and Fig. 4-9 (b) summaries the 3-dB bandwidth at different photocurrent. As the photocurrent increases from 1 mA to 40 mA, the 3-dB bandwidth increases from 3 GHz to 7 GHz. As mentioned above, the bandwidth of the 50- μm devices is transit-time limited. At low photocurrent, the transport of photo-generated electrons in the undepleted absorber is primarily diffusion, which is much slower than drift under the electric field. The transit-time through the whole structure is dominated by that in the undepleted absorber. As the photocurrent increases, the self-induced field in the undepleted absorber increases and the electrons travel much faster. Therefore, the transit-time limited bandwidth is higher at larger photocurrent. In the experiment, the maximum photocurrent is still limited by the laser output power in our optical heterodyne setup at 1064 nm. If a ytterbium-doped fiber amplifier (YDFA) is used to further amplify the light at 1064 nm, larger photocurrent and associated 3-dB bandwidth can be achieved.

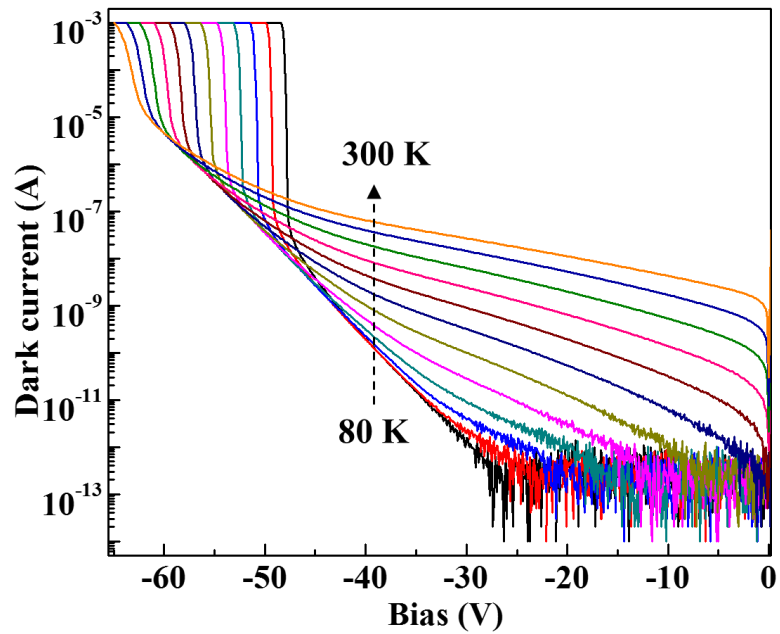


Figure 4-10. Current-voltage curves of a 50 μm device for temperature 80 K to 300 K in 20 K steps.

In quantum optical systems, the dark current of the photodiodes is one of the primary concerns.

It needs to be as low as possible to reduce the noise. In addition, some of the entangled photons will be extremely low power (~ 45 nA per pulse). Therefore the dark current needs to be low enough to measure that signal level accurately. Fig. 4-10 shows the measured current-voltage curves of a $50\ \mu\text{m}$ -diameter device in the temperature range 80 K to 300 K in steps of 20 K. At 300 K and lower bias voltage (0 to -25 V), the dark current is in the range 10-100 nA, and decreases with temperature. As expected the avalanche breakdown voltage increases with temperature owing to the fact that, when the temperature increases, the mean free path of the carrier decreases due to increased phonon scattering. Therefore, a higher electrical field is required to ensure that the carriers have sufficient kinetic energy to initiate the avalanche breakdown process.

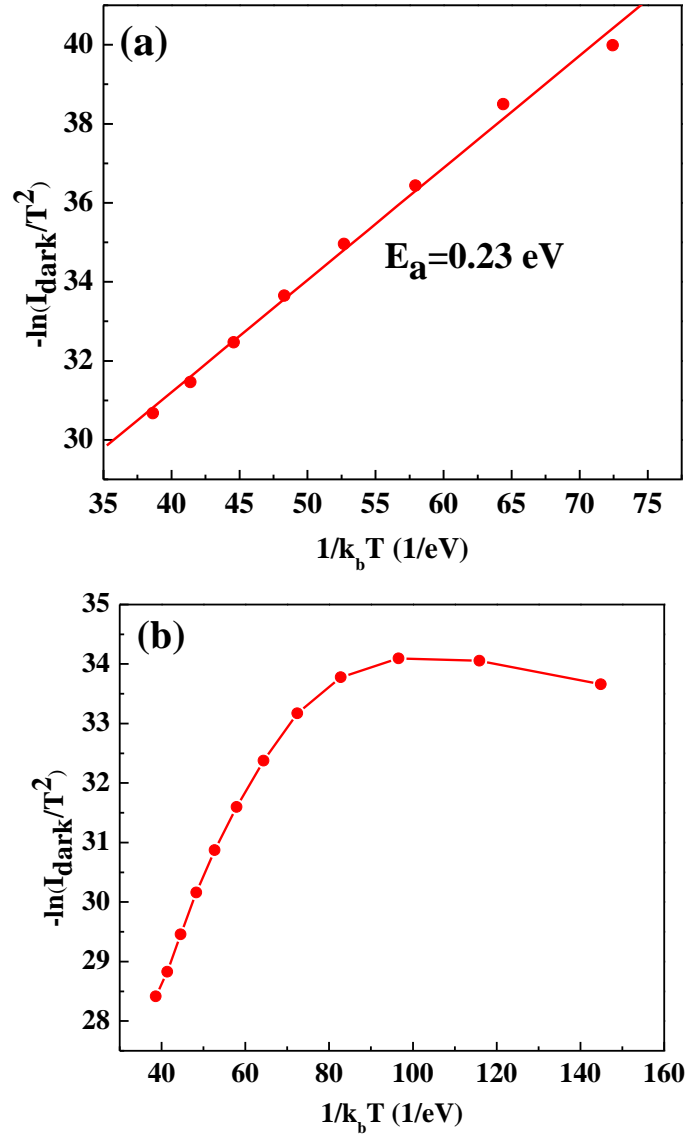


Figure 4-11. $-\ln(I_{\text{dark}}/T^2)$ versus $1/k_b T$ for a 50 μm -diameter device at (a) -10 V and (b) -35 V.

The temperature dependence of the dark current versus voltage can be used to identify the dominated physical mechanisms. There are two primary sources of the dark current, generation-recombination and band-to-band tunneling. The temperature dependence of generation-recombination is given by the expression [4.1]:

$$I_{\text{dark}} \propto T^2 e^{-\frac{E_a}{k_b T}} \quad (4.1)$$

where E_a is activation energy and k_b is the Boltzmann constant. A plot of $-\ln(I_{\text{dark}}/T^2)$ versus $1/k_b T$

is linear if the dark current is dominated by generation-recombination. On the other hand, the same plot will exhibit exponential decay if the dark current is dominated by tunneling. Fig. 4-11 (a) shows $-\ln(I_{\text{dark}}/T^2)$ versus $1/k_b T$ when the bias voltage is -10V. The slope indicates that the dark current is dominated by generation-recombination and the activation energy is 0.23 eV. The same curve at bias voltage of -35 V is shown in Fig. 4-11 (b). The nonlinearity of this curve indicates that band-to-band tunneling becomes significant at temperatures below 140 K.

4.3 Conclusion

UTC photodiodes with $98\% \pm 0.8\%$ external quantum efficiency at 1064 nm is designed and fabricated. To achieve such high quantum efficiency, a 3- μm -thick absorber is designed to fully absorb the light. The scattering and reflection at the semiconductor/air interface are also effectively reduced by high-quality surface polishing and anti-reflection coating. At bias voltage of -5 V and photocurrent of 40 mA, the 3 dB bandwidth is 7 GHz and the dark current is ~ 10 nA. The dark current at low bias voltage is dominated by generation-recombination with 0.23 eV activation energy.

Chapter 5. Photovaractor for optically modulated scatterer

5.1 Device design and fabrication

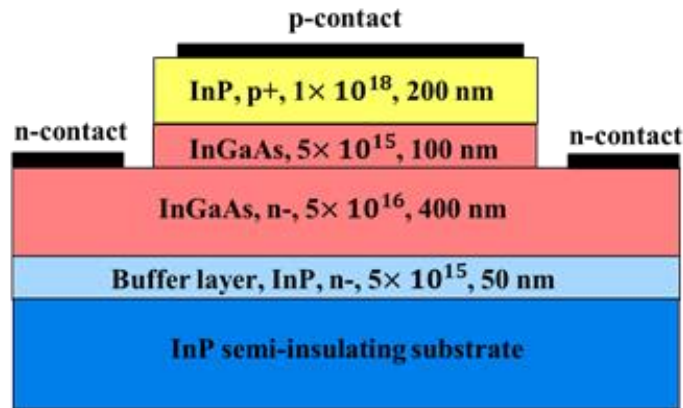


Figure 5-1. Epitaxial-layer design of the photovaractor.

Varactors are widely used in RF oscillators, reconfigurable antennas, tunable filters and terahertz modulation. However, for some applications, such as characterizing the radiation pattern of an antenna, the metal in the voltage supply cable of the varactor can alter the antenna field profile and lead to measurement error. A photovaractor is a good candidate to solve this problem. The capacitance of the photovaractor is controlled by the incident optical power, which can be delivered with an optical fiber that will not distort the near field of the antenna. Further, if the photovaractor can be operated at zero bias, the associated circuitry is greatly simplified. In addition, optical control has the advantage of fast tuning speed and good isolation between the controlling and microwave signals.

Previously, several types of photovaractors have been reported. Malyshev and Chizh described the operation and optimization of an InGaAs homojunction photodiode as a photovaractor [1.30-1.32]. The largest capacitance change, $\sim 6x$, was achieved with 3 mW, 1550 nm illumination, at zero bias. However, the impedance change decreased rapidly for modulation frequency greater

than 1 GHz. F. Capasso, et al. proposed a channeling diode to achieve a large capacitance variation (~ 1 pF) with very low optical power levels (~ 20 pW) [5.1]. The demonstrated structure required a bias voltage and little change in the capacitance was observed at 0 V. C. Tsai, et al., reported a novel photovaractor that was also based on shifting the capacitance-voltage curve with illumination [5.2]. A light-induced capacitance shift of ~ 1 pF was observed for $9 \mu\text{A}$ photocurrent at zero bias. To date, only low frequency operation, < 3 GHz, has been reported for photovaractors.

At low frequencies and zero bias, the AC signal from the measurement apparatus, e.g., LCR meter or vector network analyzer (VNA), may induce diffusion capacitance because the photovaractor is forward biased during the positive half cycle. As a consequence, the measured value may be larger than the actual depletion capacitance [1.33]. Higher AC signals will induce larger diffusion capacitance. At high frequencies, both the diffusion capacitance and depletion capacitance decrease; the diffusion component drops faster owing to its shorter carrier transport time [2.14]. This calls into question whether the low frequency capacitance shift can be maintained at high frequencies.

In this part of my dissertation research, I developed a zero-bias photovaractor that operates at up to 60 GHz. The structure of the photovaractor is shown in Fig. 5-1. The epitaxial-layers were grown on semi-insulating InP substrate by metal organic chemical vapor deposition (MOVCD). The first layer is a 50 nm InP buffer layer. This is followed by 400 nm lightly n-doped ($5 \times 10^{16} \text{ cm}^{-3}$) and 100 nm unintentionally doped ($5 \times 10^{15} \text{ cm}^{-3}$) InGaAs absorber. Finally, the top layer is a 200 nm heavily p-doped ($1 \times 10^{18} \text{ cm}^{-3}$) InP contact layer.

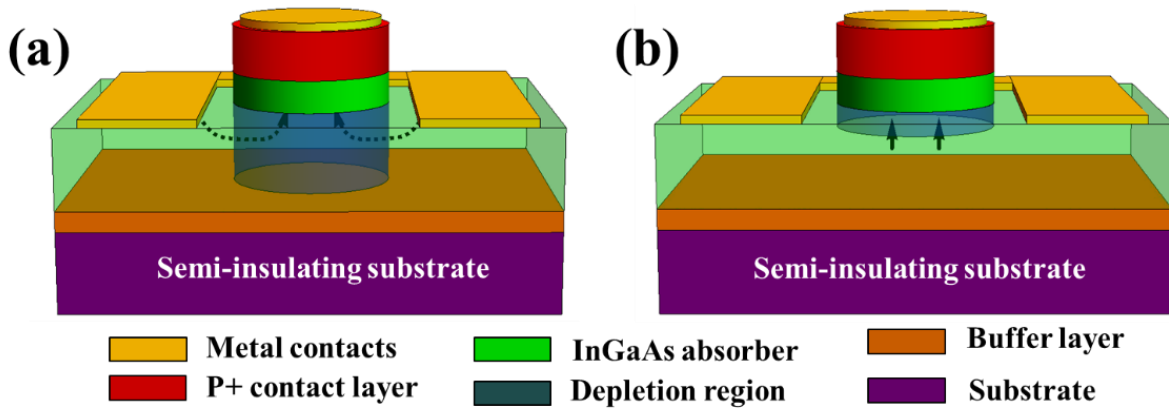


Figure 5-2. The depletion region in the dark case (a) and after illumination (b).

The operation of the photovaractor is illustrated in Fig. 5-2. At reversed bias voltage, the capacitance of the p-n junction is dominated by the depletion capacitance, which can be expressed as:

$$C = \frac{\epsilon_s A}{W_D} \quad (5.1)$$

where ϵ_s is the permittivity of the semiconductor, A is the effective area and W_D is the width of the depletion region. The dashed arrows are the sketched electric field lines. In the dark case, since the InGaAs absorber is thin and lightly doped, it is depleted to the semi-insulating substrate. Considering the capacitance between the p and n contacts, the effective area is the lateral area of the depletion region. When illuminated, the depletion region shrinks and a low-resistance channel is generated between the depletion region and substrate due to the accumulation of photo-generated carriers. In this case, the effective area becomes the sum of the lateral and bottom areas. Although the lateral area decreases somewhat, the additional bottom area dominates because it is much larger than the lateral area. In addition to the increase of effective area, A , the depletion width w_D also decreases. The combination of these two effects enables a large change in capacitance with illumination.

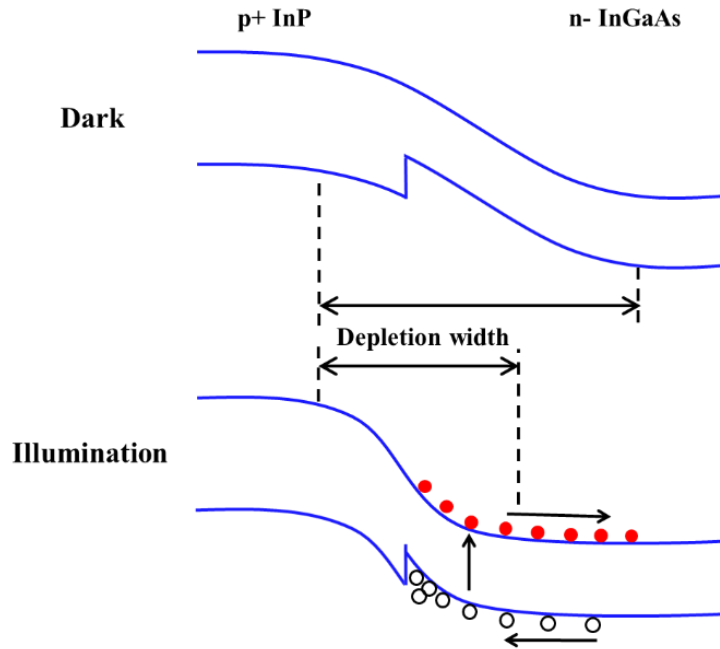


Figure 5-3. The decrease of depletion width after illumination.

Fig. 5-3 illustrates the decreasing depletion width. Owing to the band gap difference, there is a barrier in the valence band at the InP/InGaAs heterointerface. This barrier is very important for realizing the capacitance change of the photovaractor. In the case of illumination, the photo-generated holes will accumulate at this barrier. The accumulation of positive charge creates an increased potential in this region, which corresponds to a drop of the band diagram. As shown by the dashed box, after illumination, there is no electric field in this region and it becomes undepleted. Therefore, the depletion region becomes narrower and the slope in the band diagram becomes steeper.

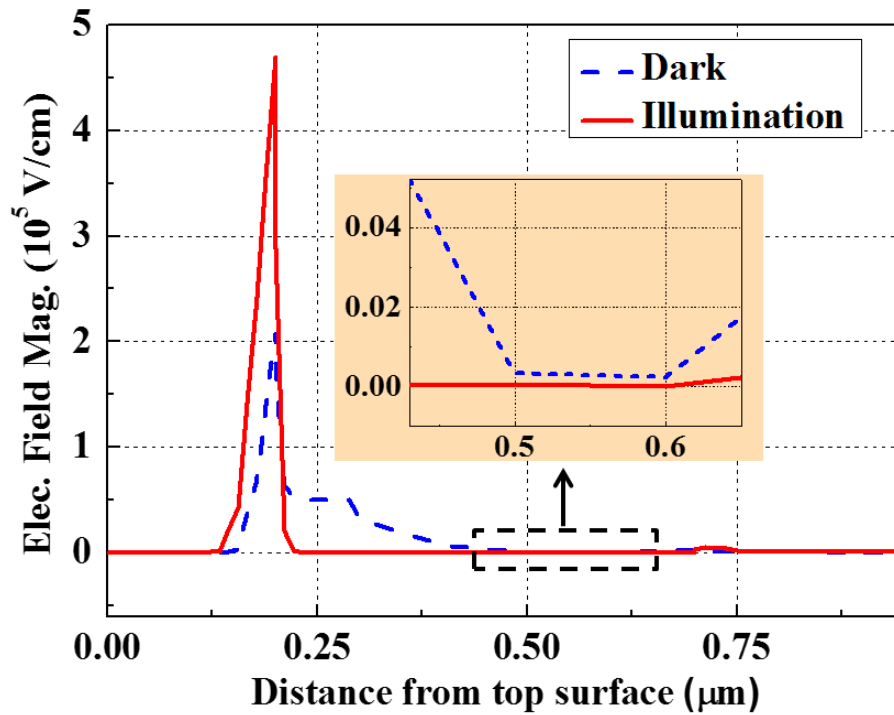


Figure 5-4. A vertical cut of the simulated electric field distribution.

The electric field distribution without bias was simulated with Crosslight software and is shown in Fig. 5-4. The horizontal axis is the distance from the top of the p⁺ InP layer. The dashed curve depicts the electric field in the dark case, while the solid line is that after illumination. The inset is an expanded view of the two curves. In the dark case, the electric field extends across the whole InGaAs absorber and the buffer layer, which means they are fully depleted. After illumination, the electric field drops to zero in most of the InGaAs absorber, an indication of decreased depletion width. Since the built-in potential remains relatively constant, the peak electric field intensity increases after illumination.

5.2 Device Characterization

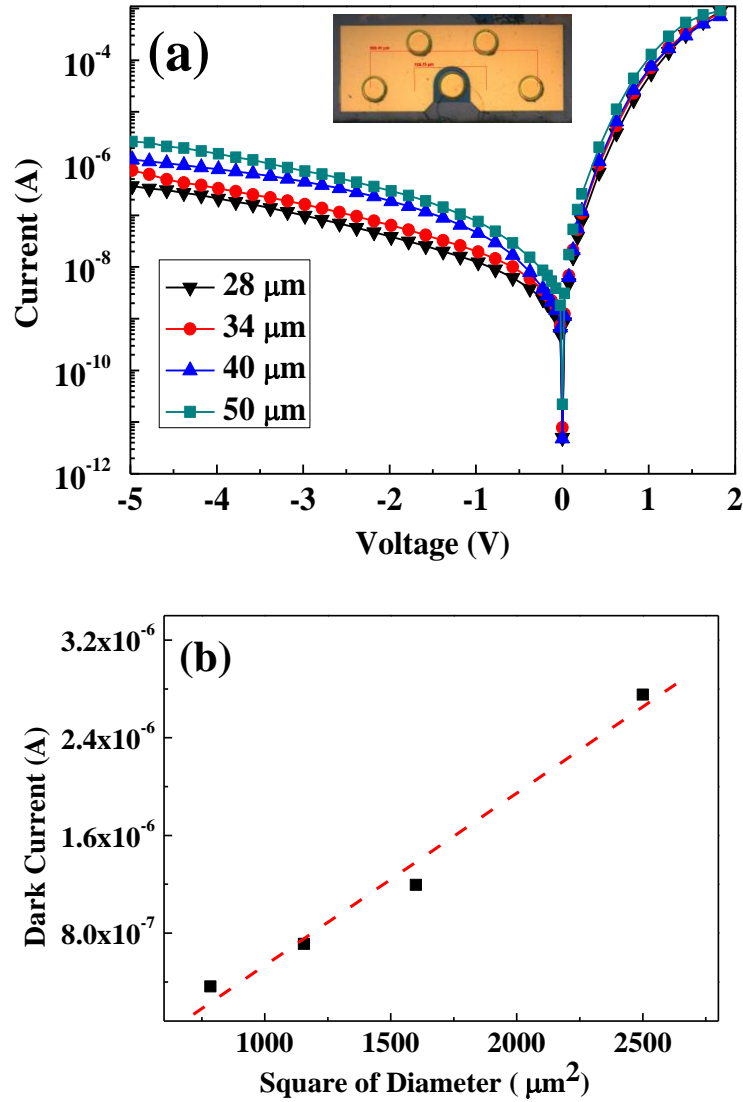


Figure 5-5. (a) Measured current-voltage curves of devices with different area and (b) dark current at -5V versus the square of the diameter.

Figure 5-5 (a) shows measured current-voltage curves for devices with diameters of 28 μm , 34 μm , 40 μm , and 50 μm , respectively. The forward current increases to the compliance value (1 mA) at 1.7 V, which indicates a relatively large series resistance resulting from the lightly-doped n-type region. At -5 V, the dark current of all the devices is approximately 1 μA . The insert is a photo of the fabricated device. Figure 5-5 (b) shows that the dark current exhibits a linear

relationship with the square of the device diameter, an indication that bulk leakage dominates.

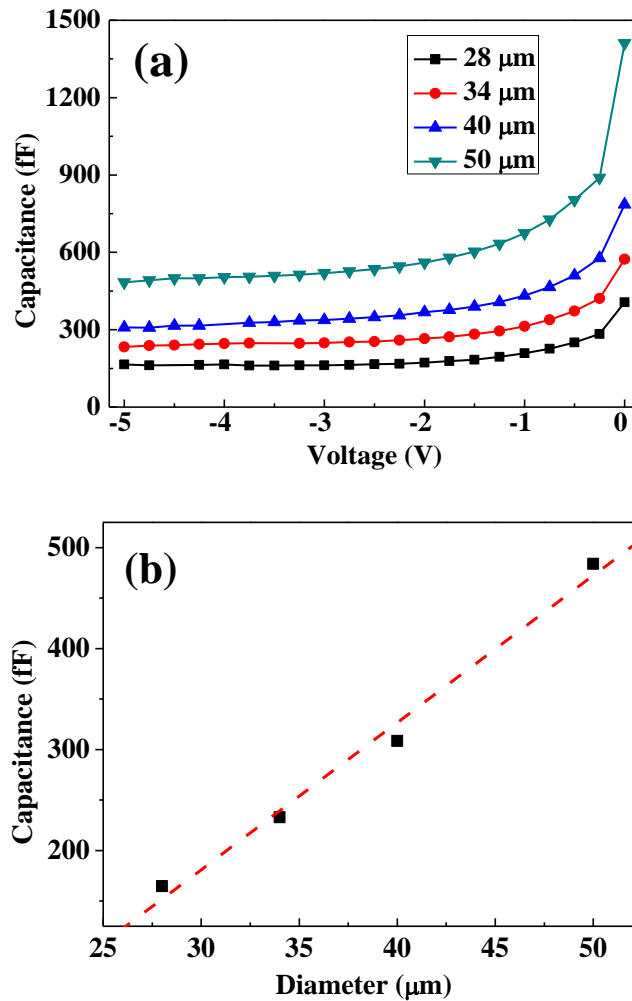


Figure 5-6. (a) Measured capacitance-voltage curves for devices with diameters of 28 μm , 34 μm , 40 μm , and 50 μm ; (b) capacitance at -5 V bias versus diameter.

The capacitance-voltage curves were measured with an LCR meter (HP 4257A). It should be noted that this is the capacitance in the low-frequency range (100 KHz). At high frequency, such as 60 GHz, the capacitance decreases owing to the frequency-dependence of the junction capacitance. As shown in Fig. 5-6 (a), the measured C-V curves can be divided into three regions. Near 0 V, the capacitance decreases rapidly with increasing reverse bias. As mentioned above, the influence of the AC voltage (~ 0.2 V_{pp}) of the LCR meter needs to be considered. Due to the low-

frequency AC signal, the varactor operates alternately in reverse and forward bias, and the diffusion capacitance is comparable to or even larger than the depletion capacitance. From -0.5 V to ~ -2 V, the capacitance decreases with bias voltage, because the depletion region under the n contact is increasing. When the reverse bias voltage is higher than - 2 V, the capacitance is relatively constant. The capacitance at -5 V versus device diameter is shown in Fig. 5-6 (b). In the dark at -5 V, the depletion capacitance is dominate and the effective area is the lateral area, which has a linear relationship with the diameter.

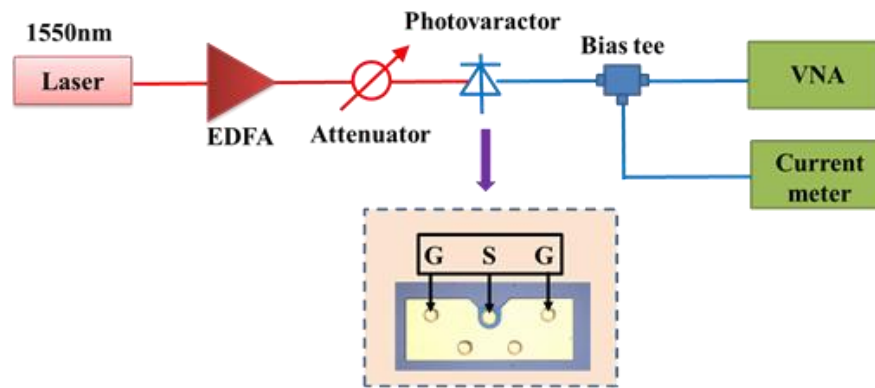


Figure 5-7. S11 measurement setup.

The impedance at high frequencies was determined by measuring the S11 parameters using a vector network analyzer. The experimental setup is shown in Fig. 5-7. Light from a CW laser at 1550 nm is first amplified by an EDFA, and then coupled into the photovaractor through a lensed fiber. An optical attenuator is inserted after the EDFA to adjust the incident signal level. To avoid the influence of the coplanar waveguide, the device is tested directly using a ground-signal-ground RF probe with pitch size of 150 μm . A current meter is used to measure the photocurrent through a bias tee. Finally, the S11 curve is measured by the vector network analyzer.

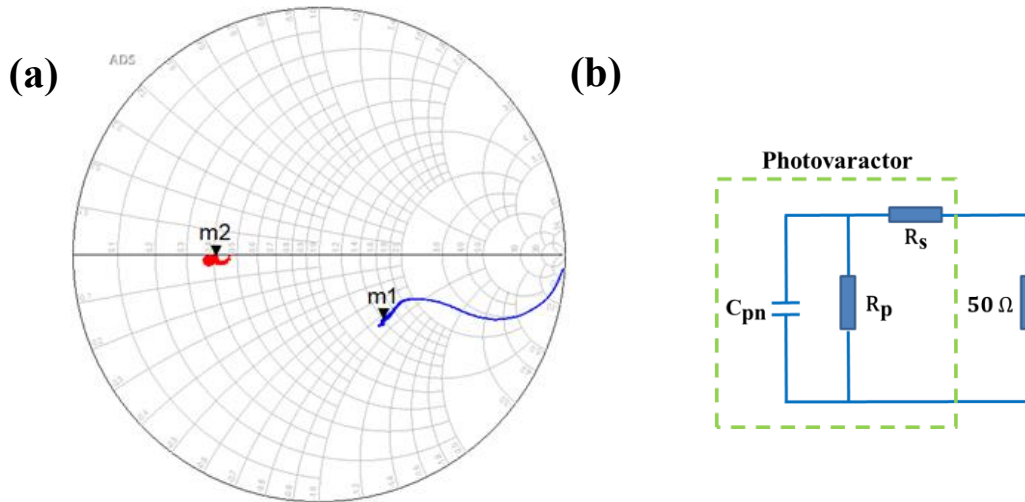


Figure 5-8. (a): S11 of a 50 μm-diameter photovaractor in the dark and after illumination. Two markers show the impedance at 60 GHz; (b) Equivalent circuit of the photovaractor.

Fig. 5-8 (a) shows the measured S11 curves of the 50 μm-diameter device in the frequency range of 100 MHz-67 GHz. The blue curve is the S11 in the dark case, while the red one is that with a photocurrent of 12 mA. Two markers in the figure show the impedance at 60 GHz: m1, the dark case, is $70.6-j42.4 \Omega$ while m2, the illuminated case, is $20.4-j0.15 \Omega$. After illumination, the resistance changes from 70.6Ω to 20.4Ω , which is a result of the photoconductive effect of the lightly-doped InGaAs absorber. The reactance at 60 GHz changes by $\sim 280\times$, which is caused by both the large capacitance and parallel resistance changes.

To fully identify the impedance changes, an equivalent circuit, shown in Fig. 5-8 (b), was used to fit the S11 measurements. C_{pn} , R_p and R_s are the junction capacitance, parallel resistance and series resistance, respectively. In the dark case, the parallel resistance is very large ($\sim M\Omega$) and can be taken as “open”. Then the equivalent circuit becomes a simple cascaded RC circuit and the series resistance and junction capacitance can be calculated directly from the input impedance. However, in the case of illumination, the parallel resistance drops to less than 100Ω and cannot be ignored. Curve-fitting of the measured amplitude and phase of S11 is needed to estimate three

parameters of the equivalent circuit: the junction capacitance, parallel resistance and series resistance.

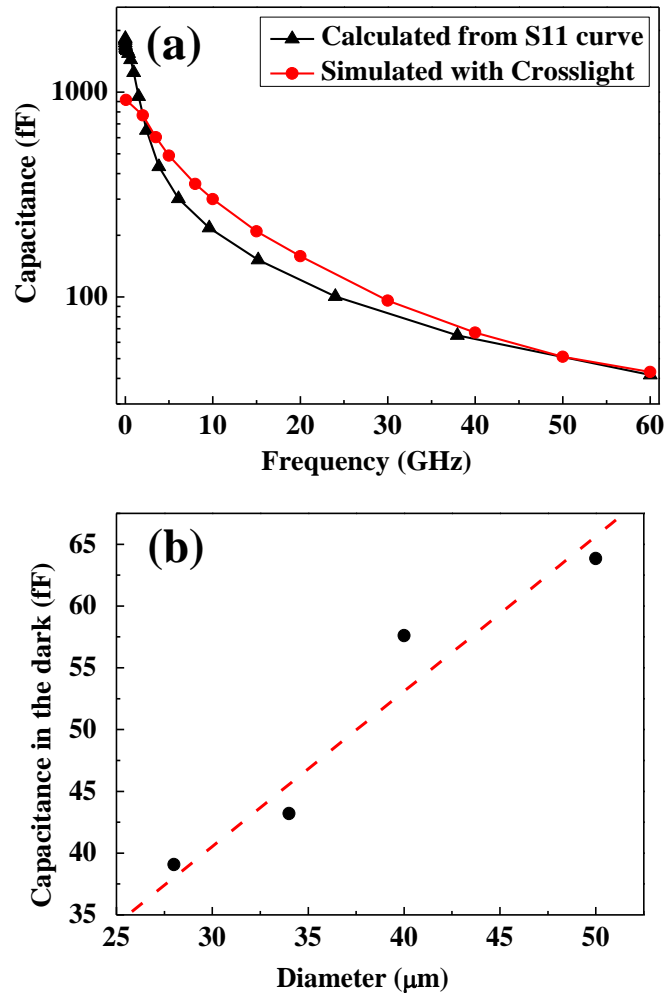


Figure 5-9. Calculated capacitance in the dark case: (a): capacitance of 50 μm device versus frequency; (b): capacitance at 60 GHz versus device size.

At zero bias, the measured capacitance has two contributions: the depletion capacitance and diffusion capacitance, which are based on the transport of majority carriers and minority carriers, respectively. As the frequency increases, both types of capacitance decrease because the carrier transport cannot follow the rapidly-changing electric field. But the diffusion capacitance will relax first because the diffusion of minority carrier is much slower than the dielectric relaxation process

of majority carriers. As estimated, the diffusion capacitance began to decrease at frequencies above 1-10 MHz, while for the depletion capacitance, that value is in the range of 1-10 GHz. In Fig. 5-9 (a), the black line is the calculated capacitance versus frequency in the dark case. For comparison, the value simulated with Crosslight is also shown by the red line. There is good agreement between these two curves. The overall capacitance decreases from ~ 2000 fF to 40 fF when the frequency increases from 100 MHz to 60 GHz. Fig. 5-9 (b) shows the capacitance at 60 GHz for devices of different sizes. In this case, the depletion capacitance is dominant and the effective area is the lateral area. Therefore, the capacitance increases linearly with the diameter. However, the absolute value is much smaller at 60 GHz. At such high frequency, the contribution of diffusion capacitance is very small and can be ignored. But the depletion capacitance, which is dominant, also suffers a large decrease due to its frequency-dependence.

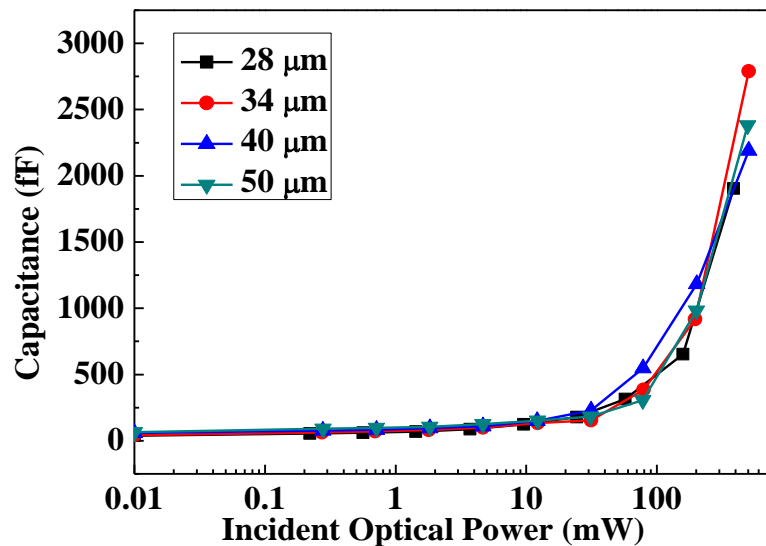


Figure 5-10. Capacitance of different-size devices versus incident optical power.

In the case of illumination, the parallel resistance drops to less than 100Ω and cannot be ignored. In the fitting process, the frequency range needs to be chosen appropriately as a result of the frequency dependence of the capacitance. In Fig. 5-9 (a), it can be seen that the capacitance

does not change very much when the frequency is higher than 40 GHz. Therefore, we chose the S11 curves in the range of 40 GHz to 67 GHz to do fitting and estimate the capacitance at 60 GHz. Fig. 5-10 shows the capacitance versus incident optical power. Since the capacitance change relies on the accumulation of the photo-generated carriers, it increases slowly when the photocurrent is lower than 2 mA. The capacitance increase becomes significant when the photocurrent is higher than 3 mA. Compared with that in the dark case, the capacitance of the 50 μm -diameter device increases from 63.8 fF to 2381 fF at photocurrent of 8.8 mA. The capacitance increased by nearly 37 times. For the 28 μm -diameter device, the increase is 49x at photocurrent of 9.6 mA.

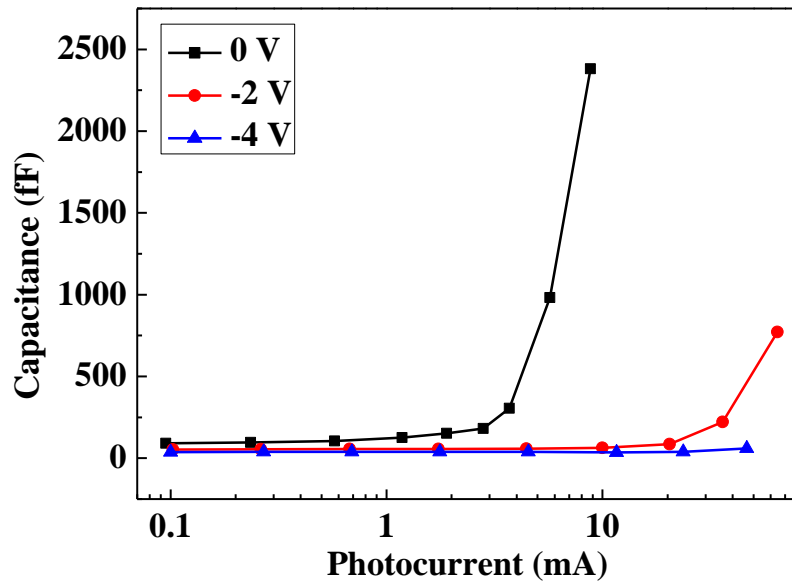


Figure 5-11. Capacitance versus photocurrent for 50 μm device at different reverse bias voltage. The measurement frequency is 60 GHz.

Fig. 5-11 shows the fitted capacitance versus photocurrent at different reverse bias voltages. As expected, the capacitance change becomes smaller when the reverse bias increases. At -4 V, the capacitance after illumination never exceeds 61 fF. The reverse bias aids hole transport at the InP/InGaAs heterointerface. Since the capacitance change is based on the accumulation of photo-generated carriers, the reverse bias will prevent the accumulation and minimize the capacitance

change. Therefore, at high reverse bias voltage, the capacitance change is not as large as that at 0 V.

5.3 Photovaractor flip-chip bonded with matching network

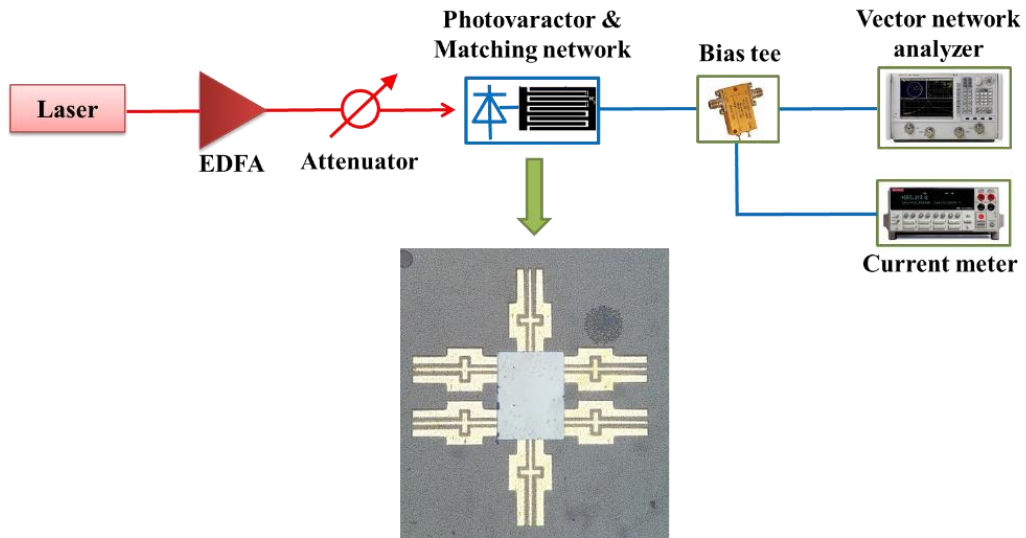


Figure 5-12. Measurement setup.

Similar to [5.3], a matching network was designed to enhance the scattering by the OMS probe and achieve a larger modulation depth. Fig. 5-12 shows the S11 measurement setup and the photovaractor on the matching network after gold-gold thermo-compression bonding. CW light from a laser is first amplified by an EDFA and then incident on the backside of the photovaractor through a lensed fiber. A tunable optical attenuator is used to adjust the incident optical power. Through a bias tee, the S11 and photocurrent is measured by a vector network analyzer and a current meter.

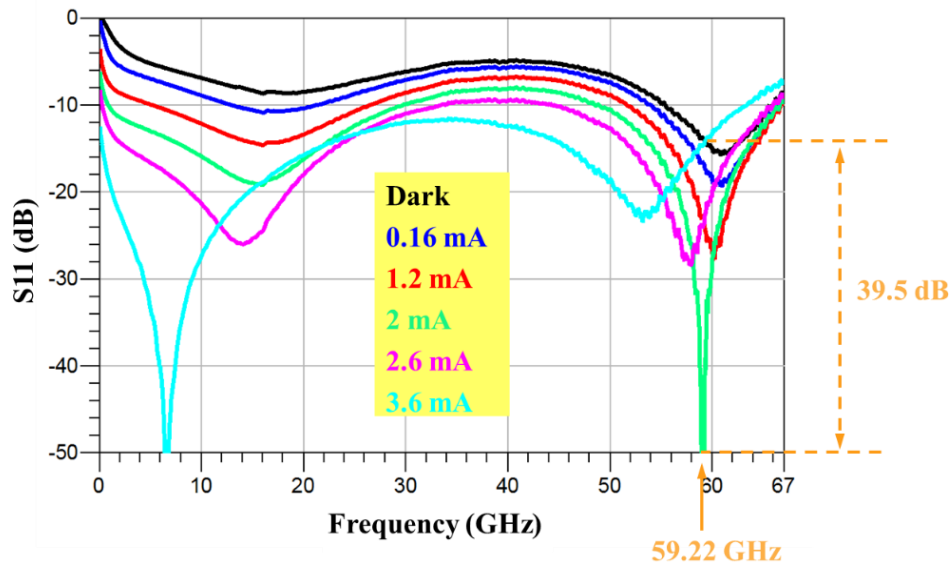


Figure 5-13 . Measured S11 versus frequency at different photocurrent.

Fig. 5-13 illustrates the measured S11 at different photocurrent. The matching network is designed so that there is resonance at 60 GHz in the case of dark. However, due to the little uncertainty in the fabrication as well as simulation, the strongest resonance is observed at 59.22 GHz with a photocurrent of 2 mA. Compared with the case of “dark” or 3.6 mA photocurrent, the difference of the S11 is 39.5 dB. Therefore, it can work in the state of “dark” and “2 mA” or state of “2 mA” and “3.6 mA”. In either case, modulation depth of 39.5 dB can be achieved.

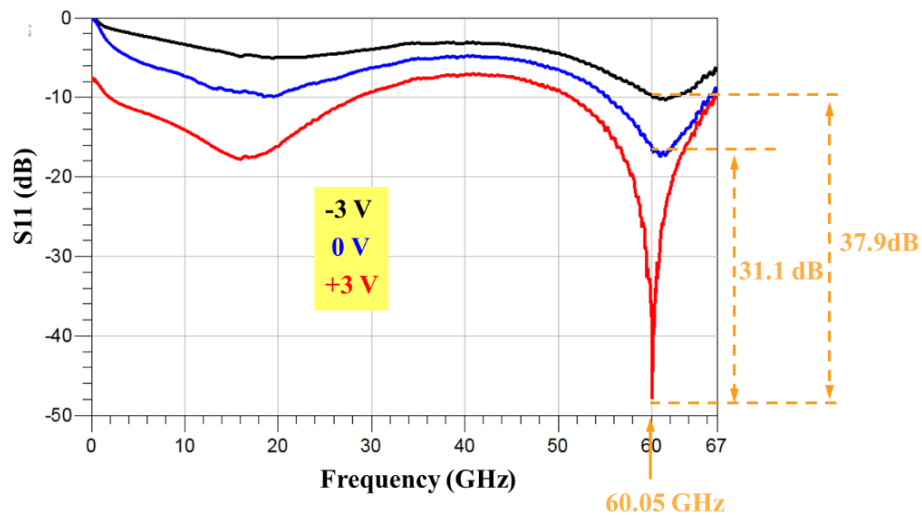


Figure 5-14. Measured S11 at different bias voltage in the dark case.

In addition to optical modulation at zero bias, the photovaractor can also be modulated electrically without illumination. Figure 5-14 shows the S11 at different bias voltages in the dark case. The strongest resonance occurs at 60.05 GHz at +3 V, which is as low as -48 dB. Compared with the case of 0 V and -3V, the S11 at 60.05 GHz is changed by 31.1dB and 37.9 dB, respectively.

5.4 Conclusion

A photovaractor was designed to operate as an OMS probe for antenna radiation measurement. The capacitance change is based on the decrease of depletion width and the steep increase of the effective area after illumination. With photocurrent of 12 mA, the reactance at 60 GHz is changed by 280 times relative to the dark condition. S11 parameter fitting shows that the capacitance of a 50 μm -diameter device increases by 37 times after illumination. The photovaractor was flip-chip bonded to a matching network to enhance the scattering. The S11 can be changed by ~ 40 dB by modulating it optically or electrically.

Chapter 6. Photovaractor Working as a Microwave

Attenuator

6.1 Introduction

Variable microwave attenuators play an important role in modern radar and telecommunications systems where continuous control of signal level is essential [6.1-6.3]. Depending on the particular applications, the key parameters of such attenuators include bandwidth, insertion loss, power handling capability, phase variation and dynamic range. In general, microwave attenuators can be grouped into two classes, i.e., transmission-type attenuators [6.4] and reflection-type attenuators [6.5]. The reflection-type attenuators usually consist of a hybrid coupler connected to variable resistance devices, such as p-i-n diodes or field-effect transistors. The tuning of attenuation is realized by changing the applied bias voltage. However, the metallic voltage control circuit may induce some electromagnetic interference. Also, the associated networks may increase the system complexity and limit the operating bandwidth of the microwave attenuator.

Here we report an optically-controlled microwave attenuator with simple structure, wide bandwidth, large dynamic range and low phase variation. The attenuator is realized by bonding a zero-biased photovaractor onto coplanar waveguide (CPW) RF pads. The attenuation is tuned by changing the intensity of light incident on the photovaractor. Compared with voltage control, the optical control has the advantage of no electromagnetic interference, fast tuning speed and good isolation between the controlling and microwave signals [1.30].

6.2 Principle of the optically-controlled microwave attenuator

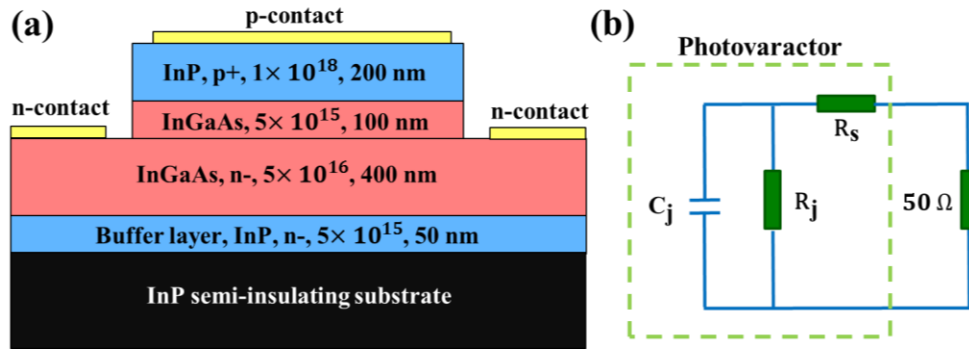


Figure 6-1. Epitaxial layers design (a) and equivalent circuit (b) of the photovaractor.

In Chapter 5, we have discussed the impedance characteristics of a zero-biased photovaractor. The equivalent circuit of the photovaractor is shown in Fig.6-1 (b). R_j , C_j and R_s are the junction resistance, junction capacitance and series resistance, respectively. In the case of dark, since the absorber is thin and lightly doped, it is depleted to the semi-insulating substrate without any bias voltage. The estimated junction resistance R_j of the varactor is on the order of $M\Omega$ s, while the junction capacitance C_j depends on the frequency. From 1 GHz to 60 GHz, the junction capacitance drops from ~ 1000 fF to 43 fF. Under illumination, R_j decreases to $\sim 20 \Omega$ and C_j increases to > 2000 fF. Therefore, the photovaractor can function as an optically controlled tunable load. If it is connected to a transmission line with characteristic impedance Z_0 (50Ω in our experiment), S11, or the reflection coefficient, can be expressed as:

$$S_{11} = \frac{Z_L - Z_0}{Z_L + Z_0} \quad (6.1)$$

The impedance of the photovaractor Z_L is:

$$Z_L = \frac{1}{1/R_j + j2\pi f C_j} + R_s \quad (6.2)$$

where f is the frequency of the RF signal. Eq. 6.1 shows that S11 can be tuned by changing the intensity of light incident on the photovaractor. Different light intensity changes the reflection

coefficient of the input microwave signal. Therefore, the photovaractor can operate as an optically-controlled reflection-type attenuator. Although this is a one-port microwave attenuator, a RF circulator or 3-dB coupler as in [6.5] can be added to enable two-port operation.

6.3 Results and discussions

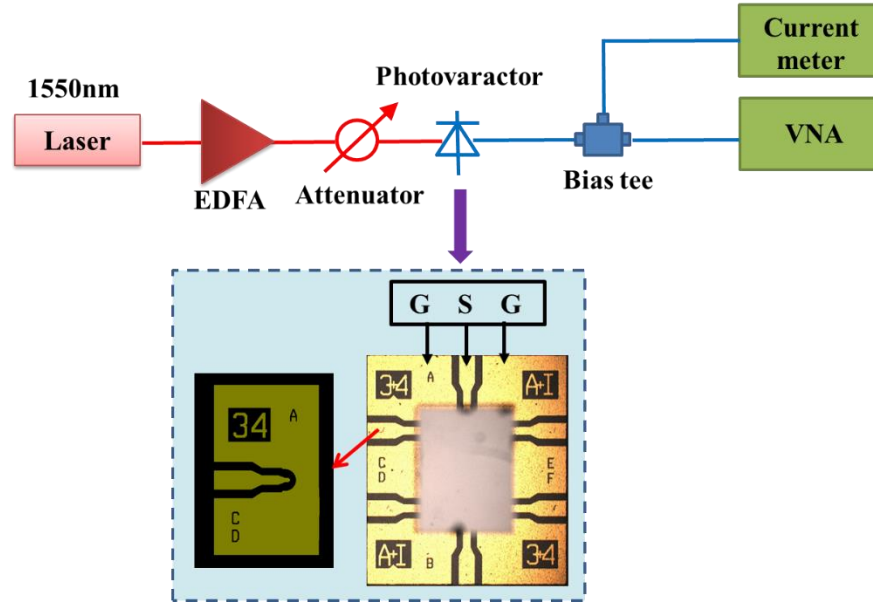


Figure 6-2. S11 measurement setup.

Fig. 6-2 shows the S11 measurement setup. Light from a CW laser at 1550 nm is amplified by an EDFA, and coupled to the photovaractor using a lensed fiber. An optical attenuator after the EDFA is used to adjust the light intensity. S11 is measured by a vector network analyzer (VNA) with a ground-signal-ground (GSG) RF probe. As shown in the inset, six 34- μm photovaractors are flip-chip bonded to coplanar waveguide pads on an AlN submount by gold-gold thermo-compression. The flip-chip bonding provides good thermal dissipation and facilitates measurements with a GSG probe.

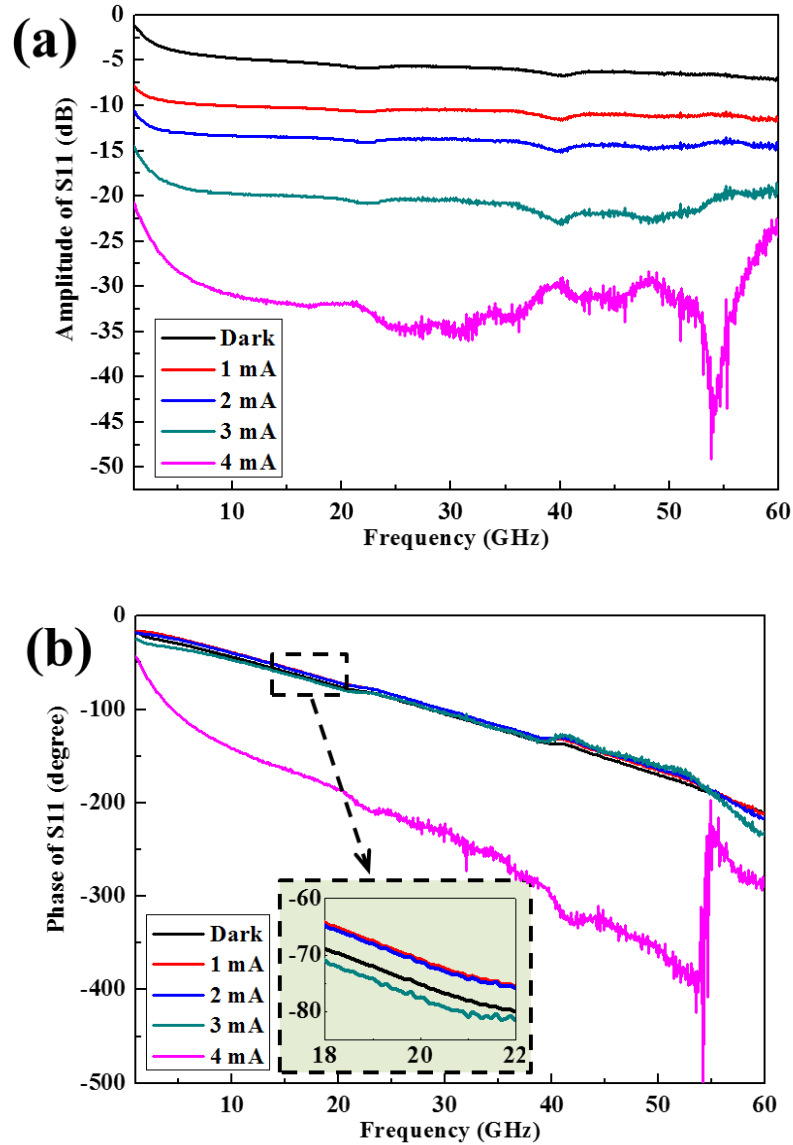


Figure 6-3. Amplitude (a) and phase (b) of S11 for 34 μm devices flip-chip bonded with CPW.

Fig. 6-3 (a) shows the amplitude of S11 in the frequency range of 1 GHz-60 GHz. As the frequency increases, the amplitude of S11 first decreases due to the frequency dependence of the photovaractor impedance, which can be seen from Eq. 6.2. At frequency >5 GHz, the curves become relatively flat. From 5 GHz to 60 GHz, the variation of S11 is less than 3 dB, except for the 4 mA curve. There are two possible reasons for the broad frequency response. First, at high frequency, the frequency-dependent term in Eq. 6.2, $j2\pi fC_j$, is so small that the overall impedance

Z_L is dominated by the resistances R_j and R_s , which are frequency-independent. Second, as the frequency increases, the junction capacitance C_j decreases [2.14], which lessens the influence of the variation of $j2\pi fC_j$ much smaller.

As the photocurrent increases from 0 to 4 mA, the attenuation at 5 GHz increases from 4 dB to 29 dB, indicating a dynamic range of 25 dB. At 25 GHz and 54 GHz, the dynamic range of attenuation is 30 dB and 40 dB, respectively. With photocurrent of 4 mA, the largest attenuation is achieved at 54 GHz, which is close to 47 dB.

For the microwave attenuators, another figure of merit is the phase variation at different attenuation values, which should be as little as possible [6.6, 6.7]. Fig. 6-3 (b) shows the corresponding phase of S_{11} at different photocurrent. The inset is a zoom-in view of the curves around 20 GHz. As the photocurrent increases from 0 mA to 3 mA (attenuation of -5 dB to -20 dB), the variation of phase is less than 10 degree in the frequency range of 5 GHz to 55 GHz. At photocurrent of 4 mA, there is a large phase change, which may result from the large attenuation at 4 mA. In this case, the reflected signal is so weak that the phase is difficult to measure accurately.

6.4 Conclusion

In this chapter, we report an optically-controlled microwave attenuator based on a zero-biased photovaractor. The proposed attenuator exhibits uniform attenuation in the frequency range of 5 GHz to 60 GHz. By changing the photocurrent, a dynamic range of up to 40 dB is achieved. At photocurrent < 3 mA, the phase variation is less than 10 degree in the frequency range of 5 GHz to 55 GHz. Having the advantage of simple structure, wide bandwidth, large attenuation dynamic range and little phase variation, the proposed attenuator may prove to be beneficial for future microwave systems.

Chapter 7. AM-to-PM in transit-time limited Photodiodes

7.1 Introduction

As noted in Chapter 1, generation of ultra-stable microwaves is important for a variety of applications such as coherent radar, telecommunications, navigation systems, timing synchronization, and photonic analog-to-digital conversion. Many approaches have been proposed to generate microwave signals with ultra-low phase noise, among which the technique based on stabilized optical frequency combs has achieved the lowest phase noise reported to date. In [1.37], the optical frequency comb from a mode-locked laser is phase-locked to the optical reference, which consists of a continuous wave (CW) laser stabilized to a high-Q Fabry-Perot (FP) resonant cavity. After photo-detection with a P-I-N photodiode, the frequency stability of the CW laser is transferred to the generated microwave signal. Based on this approach, a 10 GHz signal with integrated timing jitter of 760 fs over a bandwidth from 1 Hz-1 MHz is generated. This is one of most stable microwave signals generated by any source.

In this type of photonic oscillator, the phase noise is so low that any noise induced by the components cannot be neglected. One of the primary noise sources is amplitude-to-phase (AM-to-PM) conversion in the photo-detection process. Due to the AM-to-PM effect, the intensity fluctuations of the laser are converted to phase variations of the generated microwave signal, which can significantly affect the overall timing performance.

To reduce AM-to-PM conversion, several approaches have been proposed [7.1-7.6]. It has been demonstrated that the AM-to-PM coefficient α varies with photocurrent, and there are “null” points at certain photocurrent levels [1.51]. The bias voltage of the photodiode also influences the photocurrent value where the “null” points occur. Therefore, it is possible to effectively reduce the AM-to-PM conversion and relax the requirement on the laser relative intensity (RIN) noise by

operating the photodiode at one of the “null” points [7.4, 7.5]. Software-based automatic control systems have been used to rapidly find the specific parameters for “null” points in order to achieve long-term, stable RIN rejection > 50 dB [7.6]. However, these methods do not solve the fundamental problem and may increase the system complexity and instability. Ideally, the best solution is to identify the origin of AM-to-PM and re-design the photodiode to suppress it.

7.2 Device design and fabrication

CC-MUTC	Optimized CC-MUTC		
InGaAs, p+, Zn, 2×10^{19} , 50nm	InGaAs, p+, Zn, 2×10^{19} , 50nm	Un-depleted Absorption Layer	
InP, p+, Zn, 2×10^{18} , 100nm	InP, p+, Zn, 5×10^{18} , 100nm		
InGaAsP,Q1.1, p+, Zn, 5×10^{18} , 15nm	InGaAsP,Q1.1, p+, Zn, 5×10^{18} , 15nm		
InGaAsP,Q1.4, p+, Zn, 5×10^{18} , 15nm	InGaAsP,Q1.4, p+, Zn, 5×10^{18} , 15nm		
InGaAs, p+, Zn, 2×10^{18} , 200nm	InGaAs, p+, Zn, 5×10^{18} , 200nm		
InGaAs, p+, Zn, 1×10^{18} , 200nm	InGaAs, p+, Zn, 5×10^{18} , 200nm		
InGaAs, p+, Zn, 5×10^{17} , 200nm	InGaAs, p+, Zn, 5×10^{18} , 200nm		
InGaAs, n-, Si, 1×10^{16} , 80nm	InGaAs, n-, Si, 3×10^{16} , 80nm		Depleted Absorption Layer
InGaAsP, Q 1.62, n-, Si, 1×10^{16} , 120nm	InGaAsP, Q 1.62, n-, Si, 3×10^{16} , 120nm		
InGaAsP, Q 1.58, n-, Si, 1×10^{16} , 120nm	InGaAsP, Q 1.58, n-, Si, 3×10^{16} , 120nm		
InGaAsP, Q1.4, n-, Si, 1×10^{16} , 15nm	InGaAsP, Q1.4, n-, Si, 1×10^{16} , 15nm		
InGaAsP,Q1.1, n-, Si, 1×10^{16} , 15nm	InGaAsP,Q1.1, n-, Si, 1×10^{16} , 15nm		
InP, n-, Si, 3×10^{17} , 50nm	InP, n-, Si, 3×10^{17} , 50nm		
InP, n-, Si, 1×10^{16} , 400nm	InP, n-, Si, 1×10^{16} , 400nm		
InP, n+, Si, 1.0×10^{18} , 100nm	InP, n+, Si, 1.0×10^{18} , 100nm		
InP, n+, Si, 1.0×10^{19} , 1000nm	InP, n+, Si, 1.0×10^{19} , 1000nm		
InP, semi-insulating substrate	InP, semi-insulating substrate		

Figure 7-1. The epitaxial layer design of the CC-MUTC and optimized CC-MUTC.

Fig. 7-1 shows a comparison of the epitaxial layer design between the original CC-MUTC (referred to in the following as simply CC-MUTC) and optimized CC-MUTC. For the CC-MUTC, the growth of the epitaxial layer begins with a 1000 nm heavily doped n-type InP contact layer, which is followed by a 400 nm lightly doped InP drift layer. A 50 nm-thick n-doped ($3 \times 10^{17} \text{ cm}^{-3}$)

InP cliff layer and two 15 nm-thick lightly n-doped InGaAsP quaternary layers were used to maintain high electric field in the depleted absorber and to help charge transport at the heterojunction interfaces. Then two unintentionally doped 120 nm InGaAsP quaternary layers and an 80 nm InGaAs layer are deposited as the depleted absorber. The un-depleted absorber consists of three 200 nm p-doped InGaAs layers, which are step-graded ($1 \times 10^{17} \text{ cm}^{-3}$, $8 \times 10^{17} \text{ cm}^{-3}$, $6 \times 10^{18} \text{ cm}^{-3}$, $5 \times 10^{19} \text{ cm}^{-3}$) to create a quasi-field that aids carrier transport. Then two 15 nm-thick p-doped InGaAsP quaternary layers are deposited to assist hole collection and a 100 nm-thick heavily p-doped InP layer is used to block electrons. Finally, the top layer is InGaAs p-contact layer with doping concentration of $2 \times 10^{19} \text{ cm}^{-3}$.

Compared with the CC-MUTC, the optimized version has two modifications: First, the doping concentration of the un-depleted absorption layer is more heavily doped ($5 \times 10^{18} \text{ cm}^{-3}$). In the un-depleted absorption layer, the intensity of the self-induced field can be expressed as [7.7]:

$$E(x) = \frac{J(x)_h}{qp_0\mu_h} \quad (7.1)$$

where $J(x)_h$, p_0 , μ_h is the hole current density, doping concentration, and hole mobility, respectively.

It can be seen that, increasing the doping concentration will weaken the self-induced field, thus suppressing the electron acceleration in the un-depleted absorption region. Second, the doping concentration of depleted absorption layer is increased from $1 \times 10^{16} \text{ cm}^{-3}$ to $3 \times 10^{16} \text{ cm}^{-3}$ to pre-emphasize the electrical field distribution in this region, which can prevent the collapse of electric field at large photocurrent and suppress the associated hole deceleration. Therefore, the optimized CC-MUTC is expected to have lower AM-to-PM conversion than the original CC-MUTC.

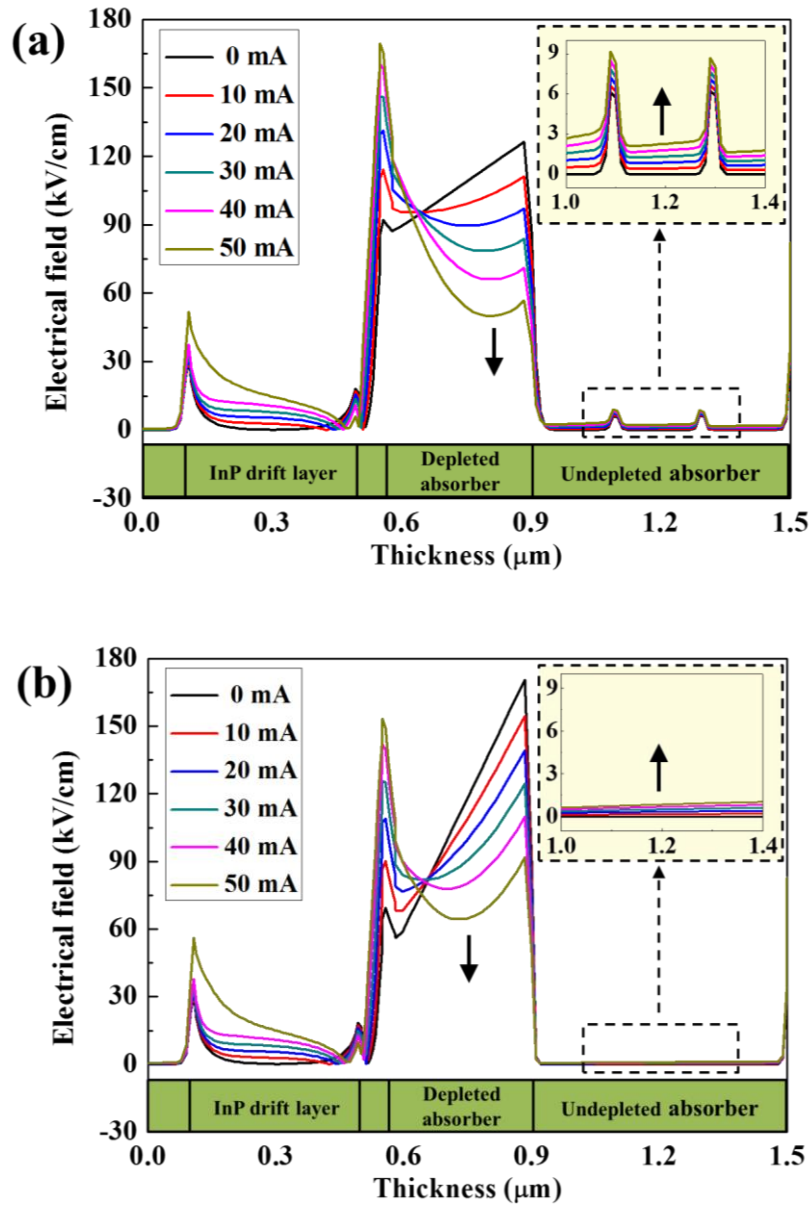


Figure 7-2. Simulated electric field distribution at different photocurrent for CC-MUTC (a) and optimized CC-MUTC (b).

The electric field distribution was simulated with Crosslight software. The same drift-diffusion model as in [1.53] was used and the bias voltage was -3 V. Fig. 7-2 (a) and (b) compare the electric field profiles at different photocurrents in the original and optimized CC-MUTCs. As the photocurrent increases from 0 mA to 50 mA, the electric field in the undepleted absorber

increases, while that in depleted absorber decreases. However, as shown in the two insets of Fig. 7-2 (a) and (b), the photocurrent-induced field enhancement of the optimized CC-MUTC is much weaker than that of the original CC-MUTC, which results from the more heavily doped undepleted absorber in the former. In the dark case (0 mA lines in Fig. 7-2 (a) and (b)), as a result of increased doping concentration in the depleted absorber, the electric field in this region of the optimized CC-MUTC is enhanced, which can be considered as “pre-compensation” for the photocurrent-induced field collapse. At the same photocurrent, the electric field in the depleted absorber of the optimized CC-MUTC is always higher than that of the CC-MUTC. Therefore, the photocurrent-induced field change is suppressed and the optimized CC-MUTC photodiodes are expected to exhibit lower AM-to-PM conversion than the original CC-MUTC.

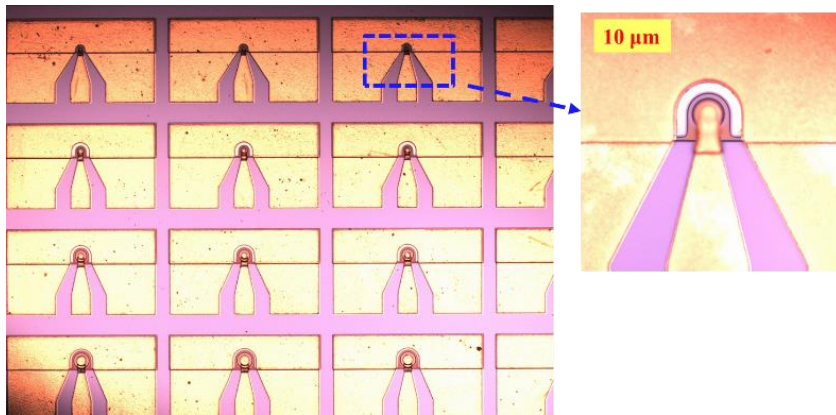


Figure 7-3. Fabricated back-illuminated devices.

The devices were fabricated as back-illuminated double-mesa structures, which is shown in Fig. 7-3. The p and n contacts are Ti/Pt/Au/Ti and AuGe/Ni/Au metal stacks deposited by e-beam evaporation. SiO₂ grown by PECVD is used as a hard mask for the mesa etch. After photolithography, both the hard mask and the III-V material are etched by inductively coupled plasma (ICP) etching. An air-bridge is formed by gold plating to connect the p contact and the RF

signal pad. Finally, the backside of the wafer is polished and coated with SiO₂ to reduce scattering and reflection.

7.2 Device Characterization

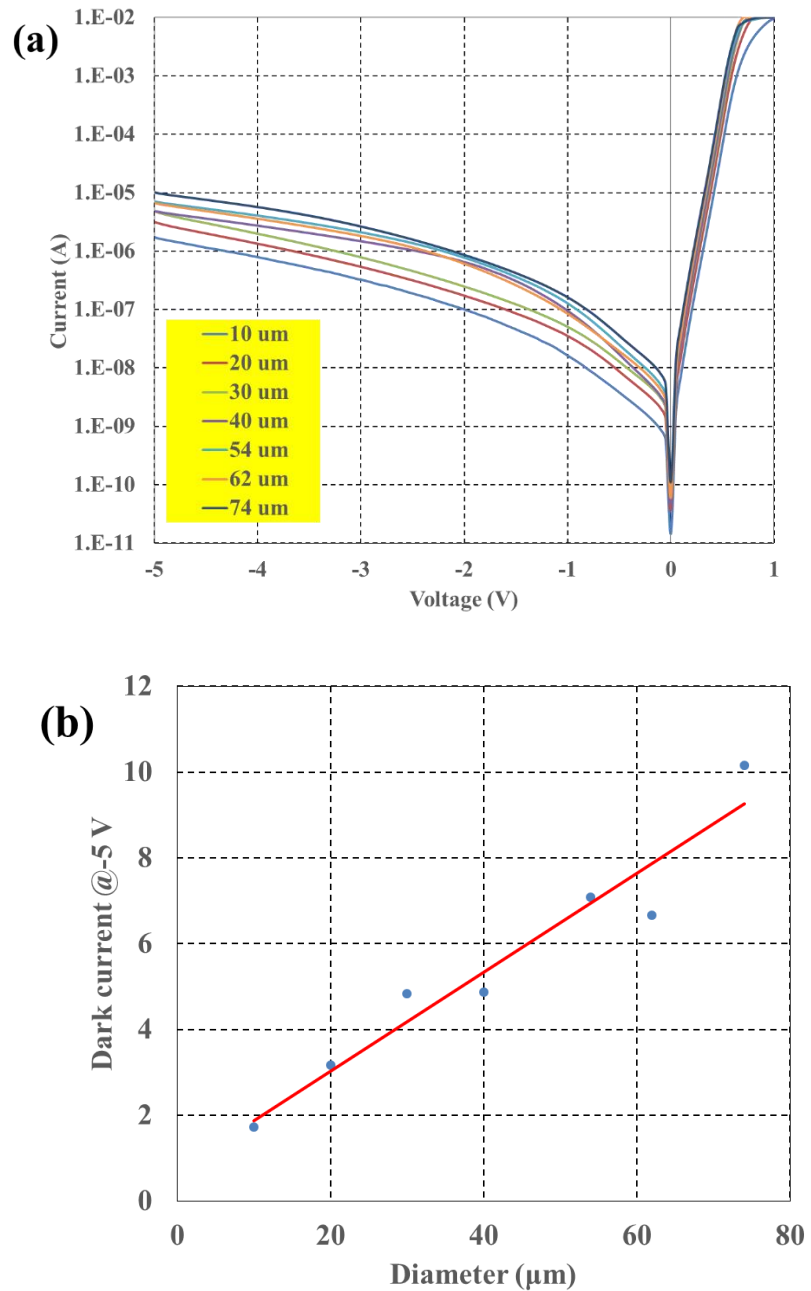


Figure 7-4. (a) Current-voltage curves of the optimized CC-MUTC photodiodes; (b) Dark current at -5V for devices with different diameter.

The optimized CC-MUTC photodiodes were fabricated in seven different diameters. Fig. 7-4 (a) shows the corresponding current-voltage curves. It can be seen that, for all the devices, the dark current at -5 V is in the range of $1\text{--}10\mu\text{A}$. Fig. 7-4 (b) shows the dark current for devices with different diameter. Since the dark current increases linearly with the diameter, it can be concluded that the surface leakage dominates.

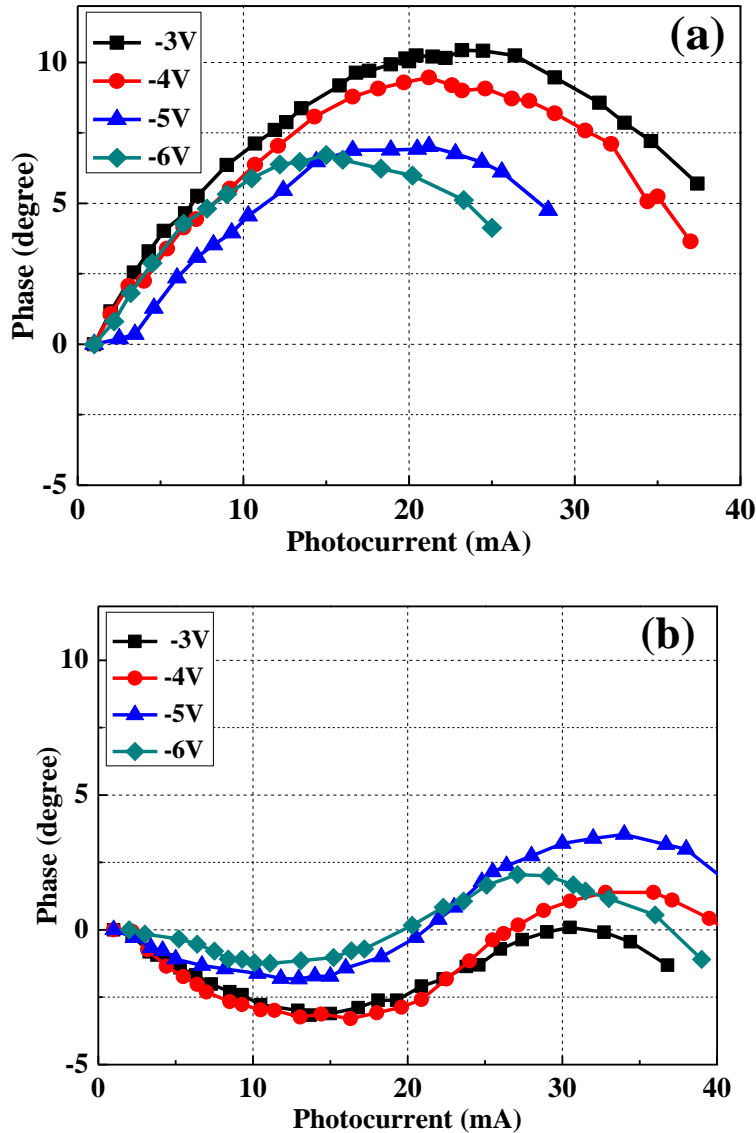
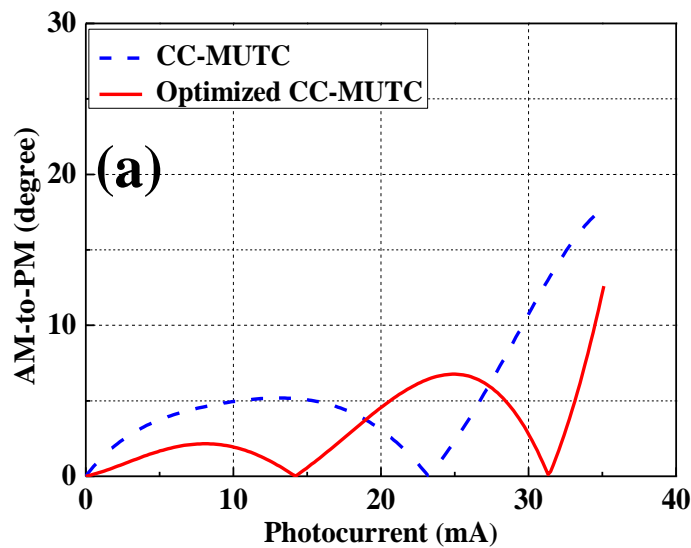


Figure 7-5. Measured phase versus photocurrent for CC-MUTC (a) and optimized CC-MUTC (b).

The measured phase of the S21 at different photocurrent for the CC-MUTC and the optimized

CC-MUTC are shown in Fig. 7-5 (a) and (b), respectively. The bias voltage varies from -3 V to -6V. For the CC-MUTC, the phase of the 15 GHz signal first increases due to the electron acceleration in the undepleted absorber and then decreases owing to the hole deceleration in the depleted absorber. For the optimized CC-MUTC, the photocurrent-induced field enhancement in the undepleted absorber is suppressed and the hole deceleration in the depleted absorber dominates at low photocurrent. Therefore, the phase of S21 first decreases for photocurrent below ~12 mA. At larger photocurrent, as shown in Fig. 7-2 (b), the increase of the electric field in both the undepleted absorber and the InP drift layer will contribute to the electron acceleration, which dominates in this case and the phase increases with photocurrent. Finally, when the photocurrent is above 30-34 mA, the collapse of the electric field in the depleted absorption region causes the hole deceleration to dominate. Therefore, the phase drops quickly with photocurrent in this case. Comparison between Fig. 7-5 (a) and (b) shows that the photocurrent-induced phase change of the optimized CC-MUTC is much lower than that of the original CC-MUTC. At bias voltage of -3 V, the range of phase change is reduced from 10.5 degrees to 3.1 degrees, indicating a decrease of more than three times after optimization.



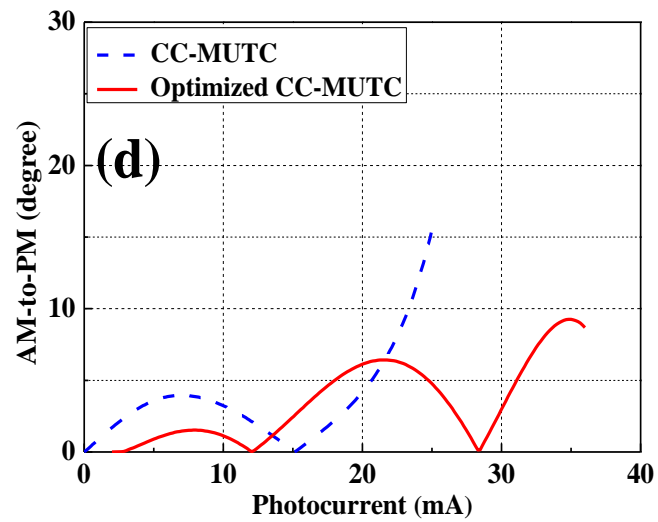
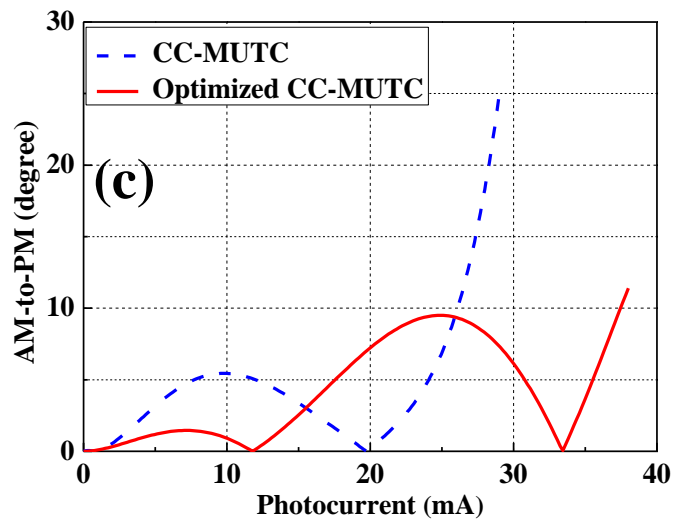
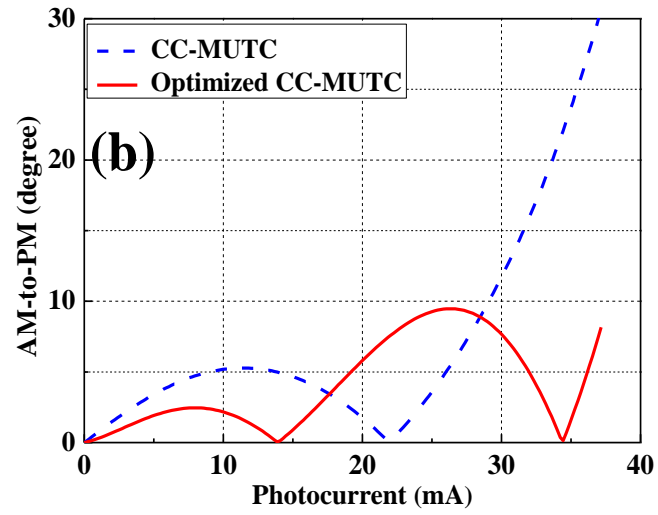


Figure 7-6. Calculated AM-to-PM coefficient versus photocurrent for CC-MUTC and optimized CC-MUTC at bias voltage of -3 V (a), -4 V (b), -5 V (c) and -6 V (d).

Fig. 7-6 (a)-(d) shows a comparison of the AM-to-PM coefficient at bias voltage of -3 V to -6 V, respectively. The dashed lines are α versus photocurrent curves for the CC-MUTC, while the solid lines are those of the optimized CC-MUTC. With bias voltage of -5 V and -6 V, the CC-MUTC devices failed at photocurrent below 28 mA, so there is no data to compare with photocurrent > 28 mA in Fig. 5-6 (c) and (d).

As shown in Fig. 7-6, there is one “null” point in the curve for the CC-MUTC and two “null” points for the optimized CC-MUTC. At photocurrent below 13 mA or above 22-27 mA, the optimized CC-MUTC always has much lower AM-to-PM coefficient than the CC-MUTC. In addition, the difference becomes larger with increasing photocurrent. The CC-MUTC only outperforms the optimized CC-MUTC in a narrow region around its “null” point.

As mentioned before, if the photodiodes operate at “null” points, there is no AM-to-PM noise conversion. The second “null” point of the optimized CC-MUTC occurs at 31.3 mA at -3 V, which is 8.3 mA higher than the “null” point of the CC-MUTC. At -4V, -5 V and -6 V, that increase of “null” point photocurrent is 12.6 mA, 13.7 mA and 13.4 mA, respectively. This is beneficial for generating ultra-low noise microwave signals because the noise floor is also limited by the power-handling capabilities of the photodiodes in these systems.

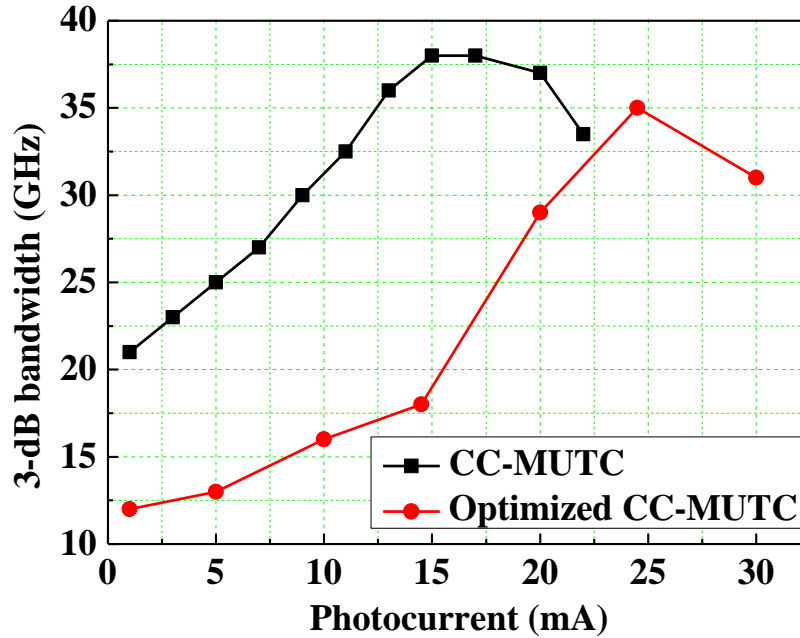


Figure 7-7. Measured 3-dB bandwidth of CC-MUTC and optimized CC-MUTC at different photocurrent, the bias voltage is -6 V.

The 3-dB bandwidth of these two types of photodiodes at different photocurrent is shown in Fig. 7-7. The bias voltage is -6 V. For the optimized CC-MUTC, the highest bandwidth of 35 GHz is achieved at photocurrent of 25 mA. As the photocurrent increases, the bandwidth also increases, but the bandwidth of the optimized CC-MUTC is always lower than that of the CC-MUTC. For 10 μm CC-MUTC devices, the bandwidth is transit-time limited. A larger photocurrent leads to stronger self-induced field in the un-depleted absorber, which results in a shorter transit-time and larger bandwidth. However, in the optimized CC-MUTC, the un-depleted absorber is more heavily doped to suppress the self-induced field. As shown in Fig. 7-2, the field-enhancement in the undepleted absorber of the optimized CC-MUTC is much weaker than that of the CC-MUTC. In addition, the elimination of graded doping in this region also removes the associated built-in electric field, which is detrimental for electron transport in the undepleted absorber. At photocurrent close to the saturation current, the bandwidth of both structures decreases because

the electric field in the depleted absorber collapses. This occurs at higher photocurrent for the optimized MUTC due to the enhanced electric field in depleted absorber.

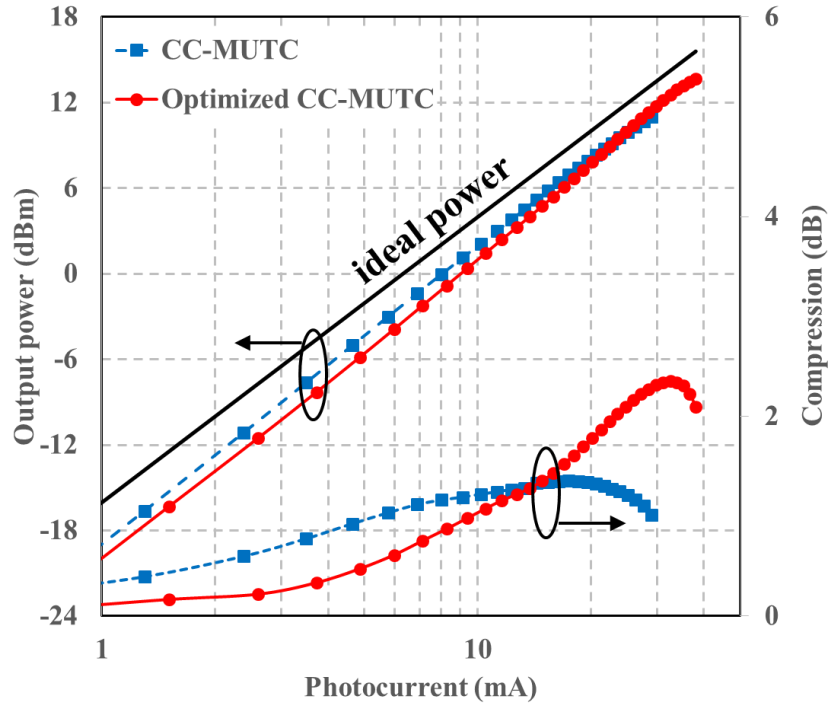


Figure 7-8. Measured RF output power and RF power compression of 10 μm devices at different photocurrent.

Fig. 7-8 shows the RF output power and power compression versus photocurrent. The RF frequency is 15 GHz and the bias voltage is -6 V. The ideal power (black line in Fig. 7-8) is the theoretical RF output power when the photodiode is modeled as an ideal current source. Assuming that the modulation depth of the incident light is 100%, the ideal power can be expressed as

$$P_{ideal} (dBm) = 10 \log_{10} (500 I^2 R) \quad (7.1)$$

where I is the DC photocurrent in units of Ampere and R is the load in the power meter (50 Ω). Both the CC-MUTC and the optimized CC-MUTC fail when the RF power compression curve drops by ~ 0.3 dB from its peak value. The maximum photocurrent and RF output power of the optimized CC-MUTC are 38 mA and 13.7 dBm, respectively, compared with 29 mA and 11 dBm for the CC-MUTC. This can be explained by the simulated electrical field in Fig. 7-2. As the

photocurrent increases, the electric field in the depleted absorber collapses due to the space-charge effect, which will limit the power-handling capability of the photodiode. In the optimized CC-MUTC, this region is more heavily doped to suppress the field collapse. As shown in Fig. 7-2 (b), at the same photocurrent, the lowest point of electric field in the depleted absorber of the optimized CC-MUTC is always higher than that of the CC-MUTC in Fig. 7-2 (a). Therefore, the maximum RF output power is also increased after optimization.

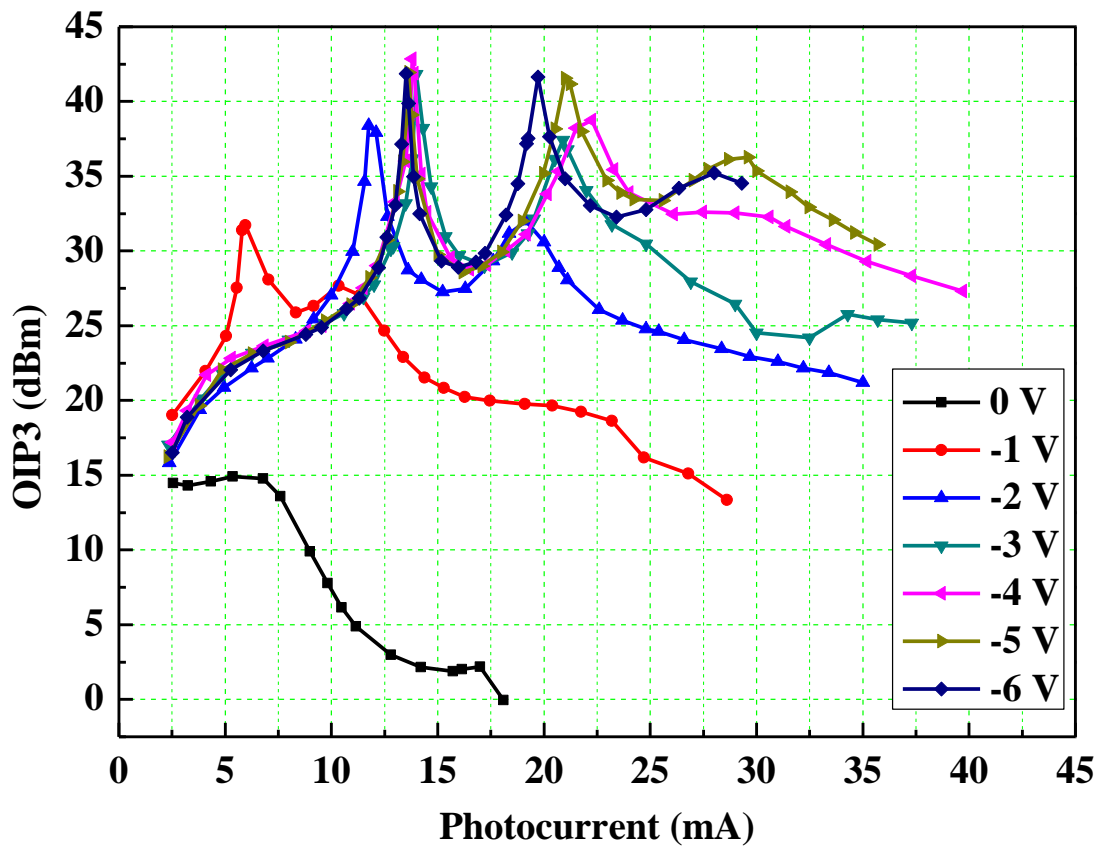


Figure 7-9. Measured OIP3-photocurrent curves of optimized CC-MUTC at different bias voltage.

Fig. 7-9 shows the OIP3-photocurrent curves of the optimized CC-MUTC at different bias voltage. A three-tone measurement setup was used and the fundamental frequency was ~300 MHz. Without bias voltage, the photodiode exhibits high nonlinearity and the maximum OIP3 is about 15 dBm. This can be explained as: at 0V, the responsivity and capacitance of the photodiodes have high

dependence on the bias voltage as well as photocurrent, and that dependence results as high nonlinearity [7.8]. With reverse bias voltage, there are two peaks in the curves: one is near 13 mA, another is approximately 21 mA, which varies with bias voltage. In the applications that require high linearity photodetection, the photocurrent should be adjusted carefully to achieve the highest OIP3, which is ~43 dBm.

7.3 Conclusion

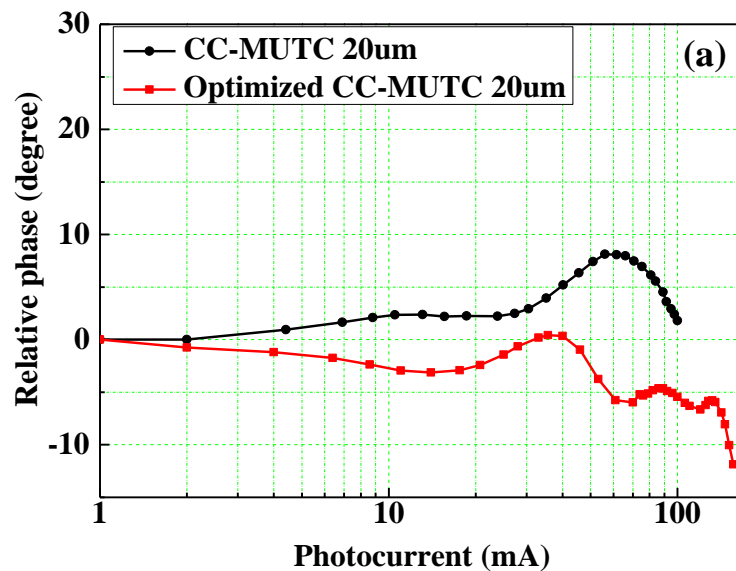
We have optimized the epitaxial layer design of the CC-MUTC photodiodes to reduce the AM-to-PM conversion. After optimization, the photocurrent-induced field enhancement in the undepleted absorber is suppressed and the collapse of the electric field in the depleted absorber is suppressed, which is verified by simulation. Measurement results show that the range of phase change at different photocurrent is reduced by more than three times and the AM-to-PM conversion is greatly suppressed, especially at large photocurrent. For 10 μm devices, the 3-dB bandwidth is 35 GHz at bias voltage of -6 V and the maximum RF output power at 15 GHz increases from 11 dBm to 13.7 dBm after optimization. For the optimized CC-MUTC photodiodes, the maximum OIP3 is ~43 dBm. Featuring low AM-to-PM and high power-handling capabilities, the optimized CC-MUTC may prove advantageous for the generation of ultra-low noise microwave signals.

Chapter 8. Investigation of AM-to-PM in Large Devices

8.1 Introduction

Chapter 7 reports AM-to-PM in 10- μm devices, which exhibit transit-time limited bandwidth. However, in the generation of ultra-stable microwave signals, the larger devices are usually preferred because they have higher power handling capabilities than smaller devices. In addition, larger devices are easier to fabricate and characterize. In this chapter, AM-to-PM in larger devices is reported. The measurement results show that, in addition to the transit time, the RC phase response also influences the AM-to-PM of these photodiodes. Further investigation shows that the phase-photocurrent curves vary with the distance between the lensed fiber and photodiode. To maintain low AM-to-PM coefficient, the photodiode should be in the focus of the lensed fiber.

8.2 Results and discussions



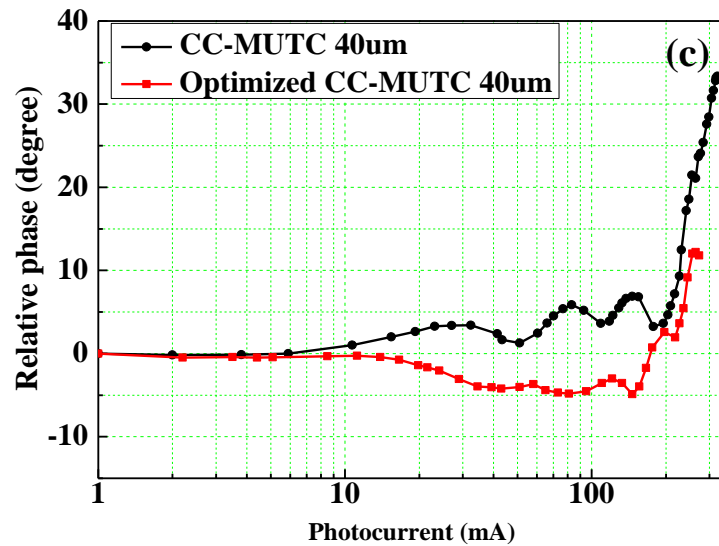
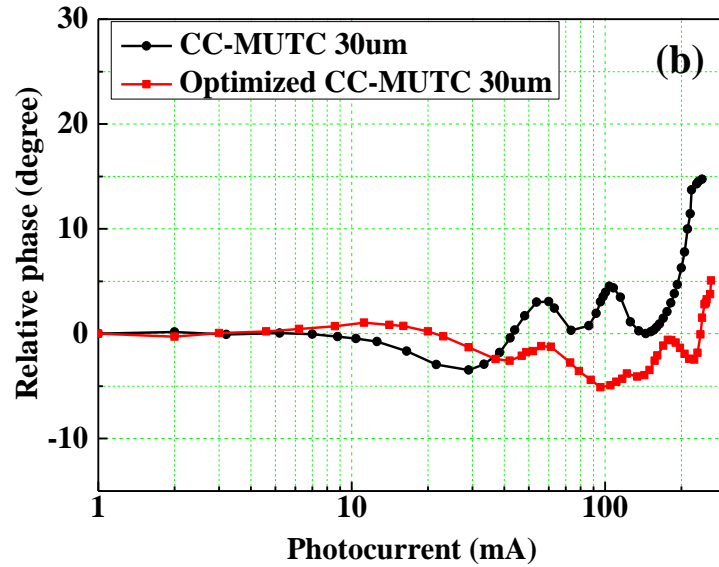


Figure 8-1. Comparison of the phase-photocurrent curves for 20 μm (a), 30 μm (b), 40 μm (c) photodiodes, the bias voltage is -3 V.

Fig. 8-1 shows the phase-photocurrent curves for 20 μm , 30 μm , 40 μm photodiodes at bias voltage of -3 V. Compared with the 10 μm devices, the phase-photocurrent curves of larger device exhibit different characteristics. First, the variation of the phase with photocurrent is totally different. For the 10 μm devices, the phase first increases, and then decreases as the photocurrent

approaches its saturation value. For the larger devices in Fig. 8-1, the trend is different and there are oscillations in the phase-photocurrent curves. Second, in Fig. 8-1, the advantage of the optimized CC-MUTC is not as obvious as for the 10 μm devices. Third, at photocurrent close to saturation, the phase of the output signal for the 10 μm devices decreases. However, for the 30 μm and 40 μm devices, that phase increases at large photocurrent. These differences indicate that there must be unknown mechanisms that influence the phase and their contributions become more obvious in larger devices.

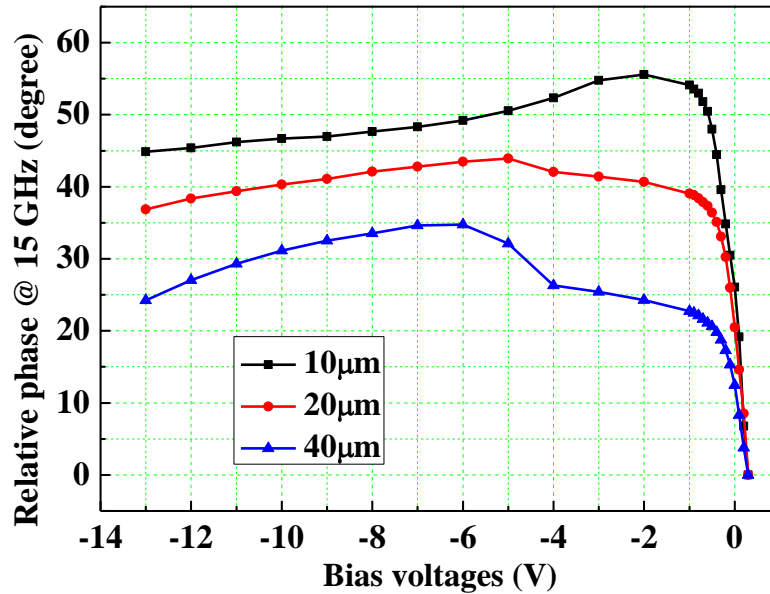


Figure 8-2. Variation of relative phase with bias voltage for different photodiodes, the photocurrent is fixed at ~ 10 mA.

Fig. 8-2 shows the measured relative phase of a 15 GHz signal at different reverse bias voltage. As the bias voltage decreases from 0.3 V to -13 V, the relative phase first increases and then decreases. In the vector network analyzer, the relationship between the measured phase shift and time delay can be expressed as [8.1]:

$$\varphi(f) = -360^\circ \cdot f \cdot \tau \quad (8.1)$$

where f is signal frequency and τ is the time delay between two ports. From Eq. 8.1, it can be seen that an increase of phase corresponds to decreasing delay. In Fig. 8-2, as the reverse bias voltage increases, the electric field in the depletion region is built up and photo-generated carriers travel faster. Therefore, the time delay becomes shorter and the measured phase will increase. Below -2 V, the relative phase does not change very much, because the carrier velocity is close to saturation velocity.

According to [1.53], the phase of the output signal is determined by the carrier velocity, or in other words, the time delay induced by the photo-detection process. For the photodiodes at the same bias voltages, the carrier velocity should not be influenced by the diameter because the electric field distribution is independent of the device size. Therefore, the relative phase for devices with different diameters is the same. However, Fig. 8-2 shows that the relative phase is different for $10\mu m$, $20\mu m$, $40\mu m$ devices. Therefore, there must be other mechanisms that influence the phase of the output RF signal.

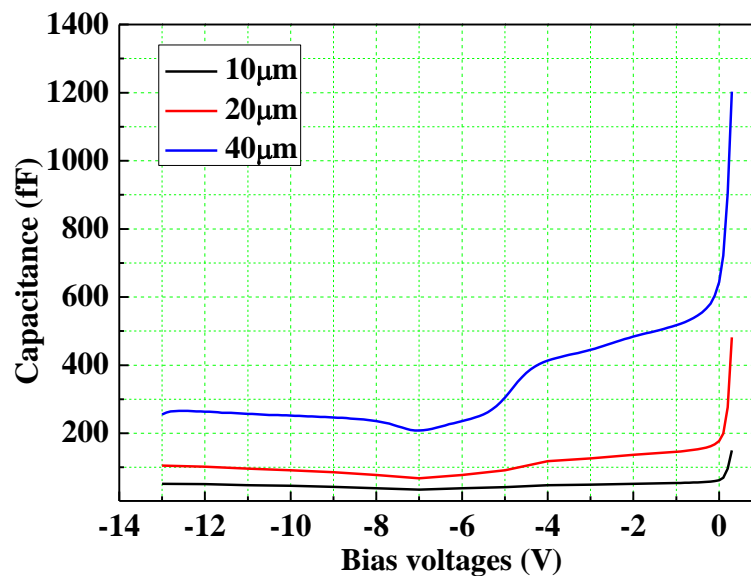


Figure 8-3. Capacitance-voltage curves of the photodiodes with different diameter.

Since the equivalent circuit of the photodiode is essentially an RC circuit, one explanation for Fig. 8-2 is that, the phase of the output signal is not only determined by the time delay, but also influenced by the RC phase response. Fig. 8-3 shows the capacitance-voltage curves of the photodiodes with different diameters. The phase response of a simple RC circuit is:

$$\text{Arg}[H(f)] = -\tan^{-1}(2\pi fRC) \quad (8.2)$$

where $H(f)$ is the transfer function of the RC circuit. As shown in Fig. 8-3, the photodiode capacitance varies with device diameter, which results as different RC phase response for different devices in Fig. 8-2.

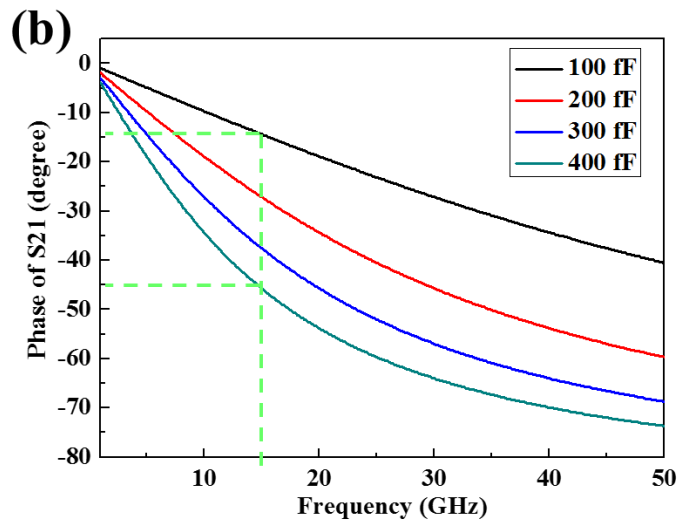
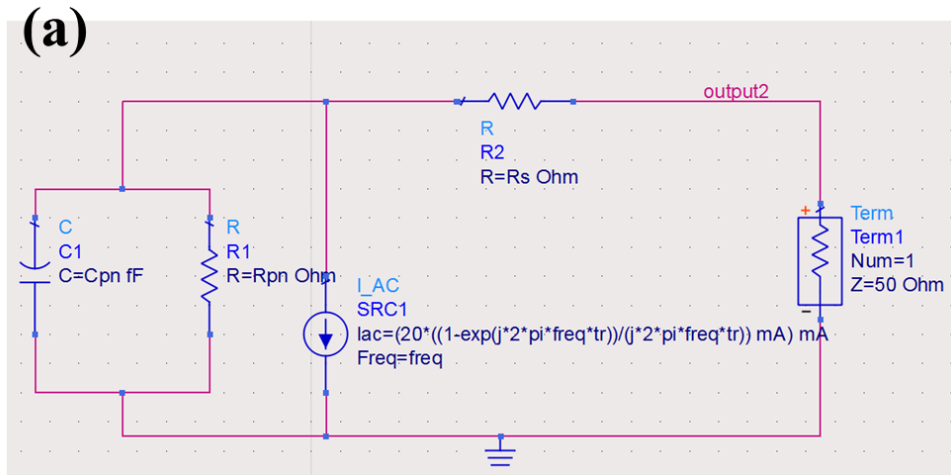


Figure 8-4. (a) ADS simulation model of the photodiode phase response; (b) simulated phase change with photodiode capacitance.

Fig. 8-4 (a) shows the phase response of the photodiode simulated with software Keysight Advanced Design System. Both the influence of the transit time and the RC phase response are included in the simulation. In fig. 8-4 (a), C1, R1 and R2 are the junction capacitance, junction resistance, and series resistance, respectively. SRC1 is the equivalent current source and the term of transit time is included in the AC current, which is defined as [8.2]:

$$I_{ac} = 20 \cdot \frac{1 - e^{j2\pi ft_{tr}}}{j2\pi ft_{tr}} \quad (8.3)$$

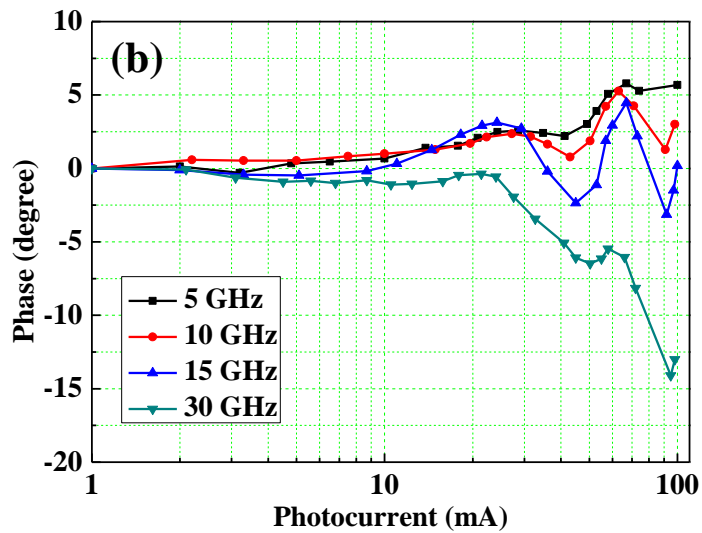
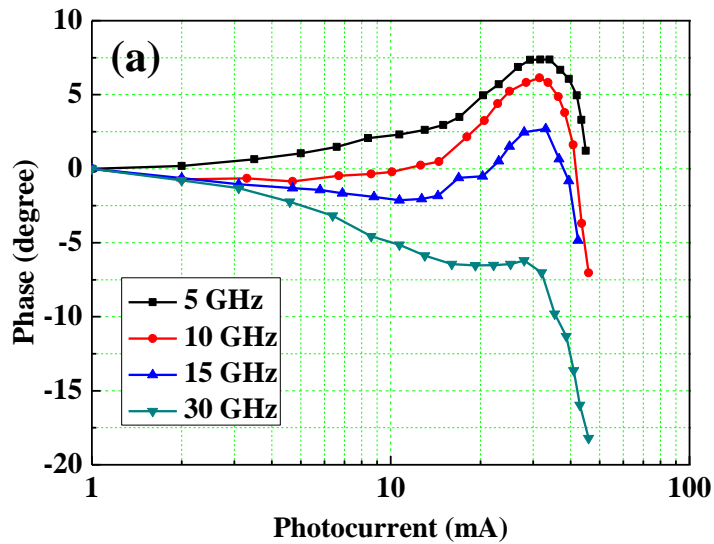
where t_{tr} is the estimated transit time. Fig. 8-4(b) shows the simulated influence of junction capacitance on the phase of the photodiode S21. In the simulation, the junction resistance is 10,000 Ω and the series resistance is 10 Ω . As the junction capacitance increases from 100 fF to 400 fF, the phase of S21 decreases from -15 degree to -45 degree, which means that capacitance increase will lead to phase decrease. Eq. 8.1 indicates that the vector network analyzer will do inverse operation on the actual phase. Therefore, the actual phase decrease corresponds to phase increase in the measurement with the vector network analyzer. That can explain why the phase will increase at large photocurrent in Fig. 8-1. As the photocurrent increases, the junction capacitance will increase as a result of the “load effect” and accumulation of photo-generated carriers in the depletion region. As mentioned above, the increase of junction capacitance will cause an increase of measured phase.

Table 8-1. Simulated phase change for 10 μm and 40 μm photodiodes.

size	C_{pn} (fF)	t_r (ps)	Relative phase (degree)
10 μm	10	4	0
	10	8	-10.8
	20	4	3.2
	20	8	-7.6
40 μm	160	4	0
	160	8	-10.8
	320	4	19
	320	8	8.2

Fig. 8-1 shows that phase behavior for 10 μm and 40 μm devices is totally different. To find the reason for that, the influence of junction capacitance and transit time on the phase of the output signal are investigated individually, as shown in Table 8-1. As mentioned above, photocurrent increases will cause an increase of the junction capacitance and decrease of the transit time due to the collapse of the electric field. In the simulation, it is assumed that both the capacitance and the transit time will double at large photocurrent. The initial values of the junction capacitance (C_{pn}) and the transit time (t_{tr}) are 10 fF and 4ps for 10 μm devices, and 160 fF and 4 ps for 40 μm devices. As shown in Table 8-1, for 10 μm devices, if only the transit time is doubled and the junction capacitance stays the same and the relative phase will decrease by -10.8 degree; if only the junction capacitance is doubled, the phase change is 3.2 degree; if both are doubled, the overall phase change is -7.6 degree. The simulation results indicate that, for 10 μm devices, although the increase of capacitance will induce some phase change, the overall phase change is still dominated by the phase change induce by the decrease of transit time. On the contrary, the simulation results

of $40\ \mu\text{m}$ devices show that the overall phase change is dominated by the influence of junction capacitance. Therefore, it can be concluded that, the phase of the RF output signal for a small device is dominated by the transit time, while for a large device, it is dominated by the RC phase response.



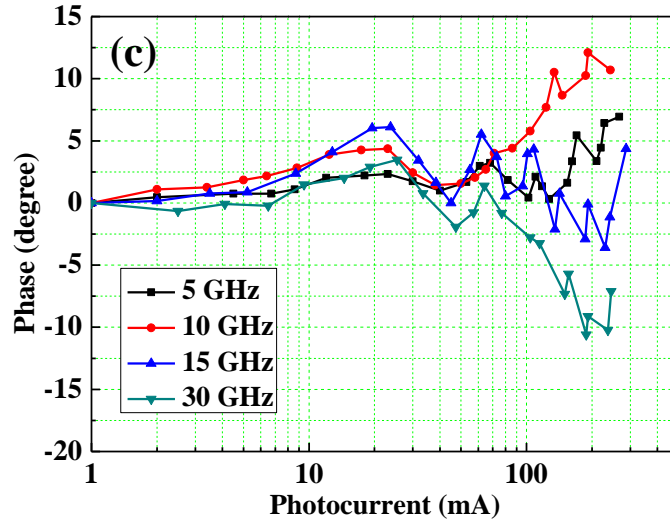
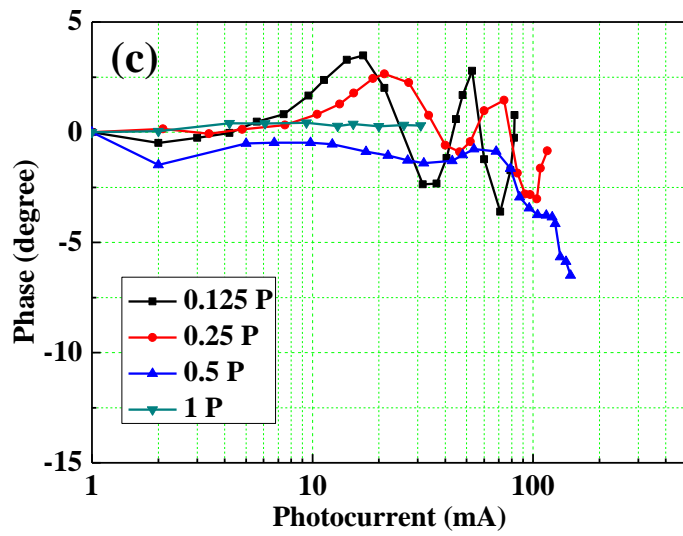
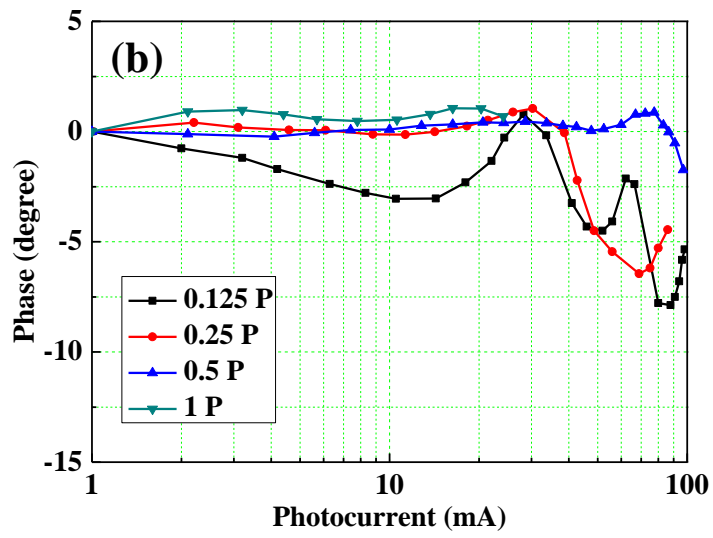
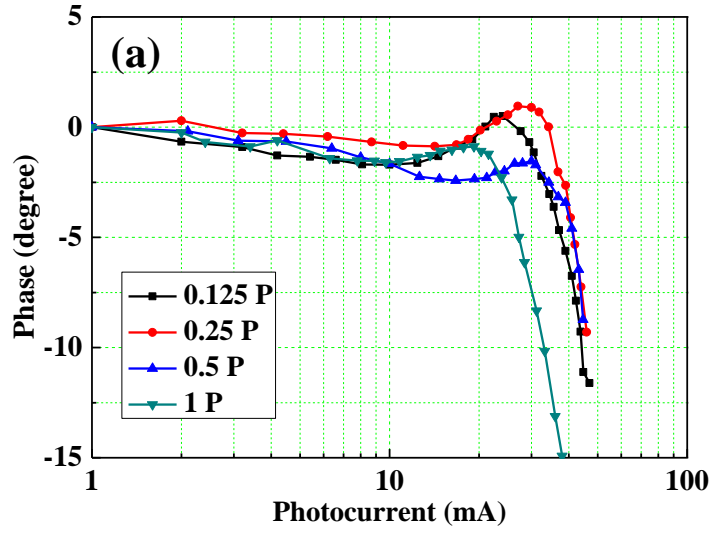


Figure 8-5. Measured phase-photocurrent curves at different frequency for $10\ \mu\text{m}$ (a), $20\ \mu\text{m}$ (b) and $40\ \mu\text{m}$ (c) optimized CC-MUTC photodiodes.

Fig. 8-5 shows the phase-photocurrent curves at different frequency. The diameter of the devices are $10\ \mu\text{m}$ (a), $20\ \mu\text{m}$ (b) and $40\ \mu\text{m}$ (c), respectively. At low photocurrent, the influence of the frequency is not so obvious and the curves of the same photodiode nearly overlap. As the photocurrent increases, the differences between these curves increase. At large photocurrent, the curves even have different trends. For example, for the $40\ \mu\text{m}$ photodiode the phase of the 5 GHz signal increases when the photocurrent is $>100\ \text{mA}$, however, the phase of the 30 GHz signal decreases with photocurrent at the same current value. That is further evidence that the phase is not only determined solely by the carrier transit times. If the phase is only determined by the transit time, the relative phase at 30 GHz should be 6 times larger than that at 5 GHz.



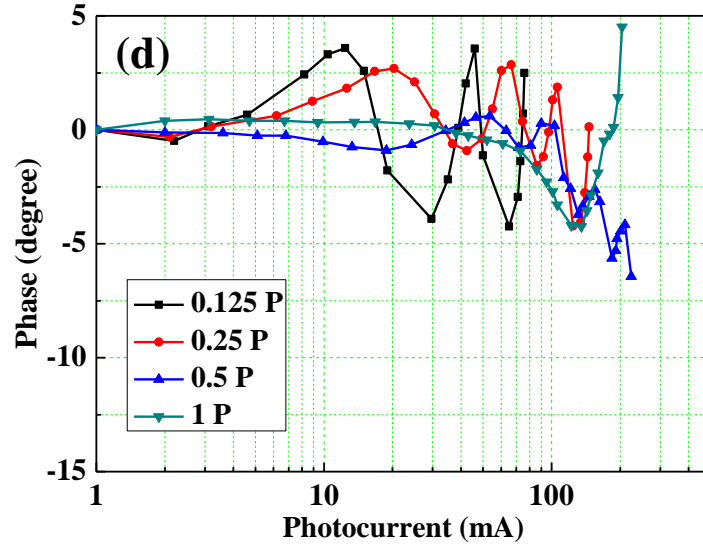


Figure 8-6. Measured phase-photocurrent curves for different distance between the lensed fiber and devices, the device diameters are $10\ \mu\text{m}$ (a), $20\ \mu\text{m}$ (b), $30\ \mu\text{m}$ (c) and $40\ \mu\text{m}$ (d), respectively.

Fig. 8-6 shows the phase-photocurrent curves for different distances between the lensed fiber and the devices. The device diameters are $10\ \mu\text{m}$ (a), $20\ \mu\text{m}$ (b), $30\ \mu\text{m}$ (c) and $40\ \mu\text{m}$ (d), respectively. The minimum spot size of the lensed fiber is $8\ \mu\text{m}$ and it is controlled by changing the distance between the lensed fiber and the photodiode. In Fig. 8-6, the case “1P” means the lensed fiber is focused on the photodiode and the spot size reaches its minimum. “0.5P”, “0.25P”, and “0.125P” represent the cases that the lensed fiber is pulled back and the photocurrent drops to 0.5, 0.25 and 0.125 of its maximum value, respectively. Fig. 8-6 shows that, the influence of the distance on the $10\ \mu\text{m}$ is not as obvious as that on larger devices. For large devices such as the $40\ \mu\text{m}$ diameter, there are oscillations in the phase-photocurrent curves if the lensed fiber is pulled far away from the device. Since the AM-to-PM coefficient is primarily determined by the slope of the phase-photocurrent curves, these oscillations will lead to larger AM-to-PM coefficient. The further the lensed fiber is pulled back, the larger is the oscillation amplitude. The reason for such phenomenon is still unknown, but the measurement results indicates that, for larger devices, the

photodiode and the fiber should be separated by the focal length to make the AM-to-PM coefficient as small as possible. In this case, however, the problem of “local saturation” may limit the maximum output power and cause early failure of the photodiode. Therefore, there is potentially a tradeoff between the power handling capabilities and the AM-to-PM coefficient for large devices.

8.3 Conclusions

In this chapter, the AM-to-PM in large ($>10 \mu m$) devices has been investigated. Measurements show that not only the carrier transit time, but also the RC phase response will influence the phase of the RF signal from the photodiodes. For the $10 \mu m$ devices, the influence of the transit time is dominant, while for larger devices such as the $40 \mu m$ devices, the influence of the RC phase response dominates. It has also been found that the phase-photocurrent curves vary with the distance between the lensed fiber and photodiode. For large devices, photodiode and the fiber should be separated by the focal length to obtain the lowest AM-to-PM noise conversion.

Chapter 9. Conclusions and Future work

9.1 Conclusions

This dissertation focuses on photodiodes for applications in quantum optics and microwave photonic systems. Three types of photodiodes have been investigated: high-efficiency photodiodes for quantum information processing, a photovaractor for optically modulated scatterer, and photodiodes with reduced AM-to-PM noise conversion.

For the high-efficiency photodiodes, we achieved $98\% \pm 0.8\%$ external quantum efficiency at 1064 nm. At bias voltage of -5 V, the 3 dB bandwidth is 7 GHz and the dark current is ~ 10 nA. The dark current at low bias voltage is dominated by generation-recombination with 0.23 eV activation energy.

For the photovaractor, we designed III-V photovaractors whose capacitance change is based on the decrease of depletion width and the steep increase of the effective area after illumination. At photocurrent of 12 mA, the reactance at 60 GHz is changed by 280 times relative to the dark condition. S11 parameter fitting shows that the capacitance of a 50 μm -diameter device increases by 37 times after illumination. The photovaractor is further flip-chip bonded with matching network to enhance the scattering. The S11 can be changed by ~ 40 dB by modulating it optically or electrically. Further, the proposed photovaractor is used as an optically-controlled microwave attenuator. The proposed attenuator exhibits uniform attenuation in the frequency range of 5 GHz to 60 GHz. By changing the photocurrent, a dynamic range of up to 40 dB is achieved. At photocurrent < 3 mA, the phase variation is less than 10 degrees in the frequency range of 5 GHz to 55 GHz.

For the investigation on AM-to-PM, we have optimized the epitaxial layer design of the CC-MUTC photodiodes to reduce the AM-to-PM noise conversion. Measurement results show that

the range of phase change at different photocurrent is reduced by more than three times and the AM-to-PM conversion is greatly suppressed, especially at large photocurrent. For 10 μm devices, the 3-dB bandwidth is 35 GHz at bias voltage of -6 V and the maximum RF output power at 15 GHz is 13.7 dBm after optimization. Further, we investigate the AM-to-PM in large ($>10 \mu\text{m}$) devices. Measurement shows that not only the carrier transit time, but also the RC phase response will influence the phase of RF signal from the photodiodes.

9.2 Future work

9.2.1 Application of photovaractors in other microwave circuits

As mentioned before, compared with electrical control, optical control has the advantage of no electromagnetic interference, fast tuning speed, and good isolation between the controlling and microwave signals. In addition to the applications in OMS probes and attenuators, the proposed photovaractor can also be used in other microwave circuits. Using the same method as Section 5.3, by varying the network design, other functions, such a microwave phase shifter, a tunable power splitter and mixer, can also be created.

9.2.2 Further investigation on the AM-to-PM in large devices

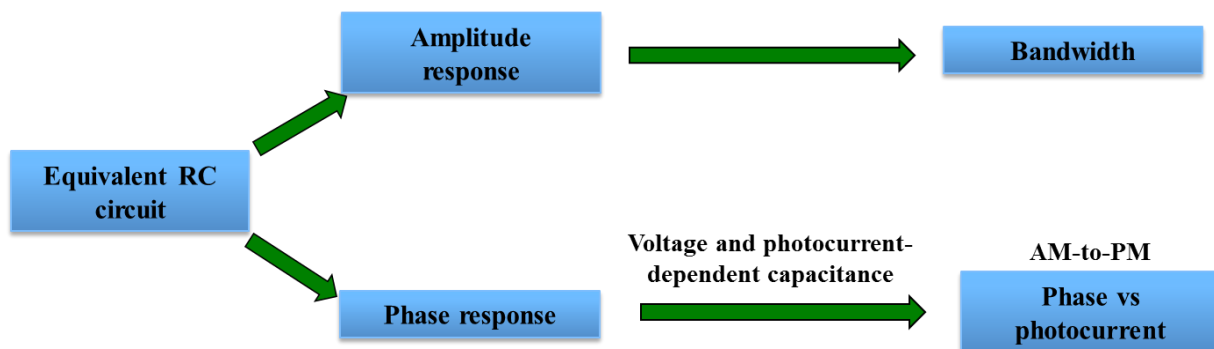


Figure 9-1. Influence of the equivalent circuit.

Chapter 8 discussed the AM-to-PM in large photodiodes and proposed a new theory for the AM-to-PM of these photodiodes. As shown in Fig. 9-1, the photodiode can be simulated as an RC equivalent circuit. The RC-limited bandwidth depends on the amplitude response of this circuit, while the phase response of this circuit influences the AM-to-PM by the voltage and photocurrent-dependent capacitance. However, this model still needs detailed theoretical analysis and simulation results to strengthen its feasibility. In addition, it is still unknown why the phase-photocurrent curves vary with the distance between the lensed fiber and the photodiode. More measurements and further investigation are needed to find a clear and complete explanation for the AM-to-PM noise conversion in photodiodes.

9.2.3 Investigation of photodiode nonlinearity

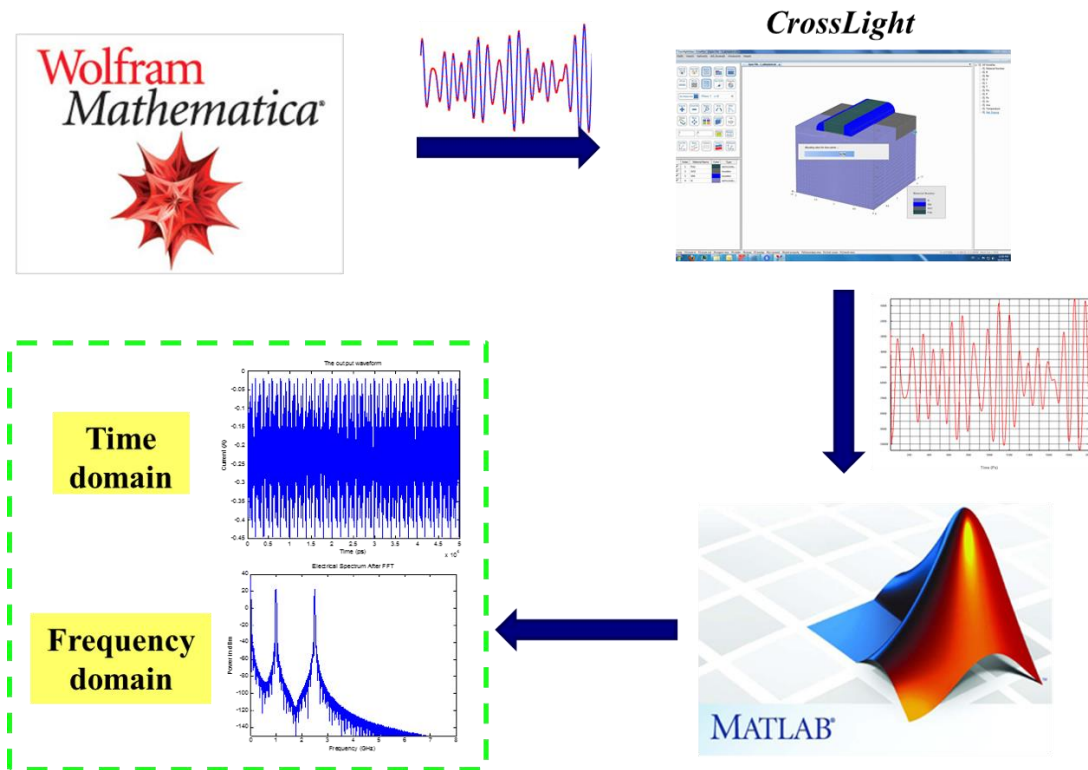


Figure 9-2. Simulation schematic of the photodiode nonlinearity.

For the applications in microwave photonic systems, photodiode nonlinearity is an essential figure of merit because it may limit the system spur-free dynamic range (SFDR) [9.1, 9.2]. However, the origins of the photodiode nonlinearity are complex and it can be influenced by bias voltage, photocurrent, and temperature. Therefore, it is necessary to refine the model of the effects that create nonlinearity and modify the photodiode design to effectively reduce the nonlinearity.

Fig. 9-2 shows a method of simulating the photodiode nonlinearity (the load effect is not included here). Three software tools are used in the simulation: Wolfram Mathematica, Crosslight and MATLAB. Wolfram Mathematica is used to generate the data sequence of ideal waveforms containing two different frequencies (2-tone OIP3). Then the data file of the ideal waveforms is imported into Crosslight to define the intensity-modulated light that is incident on the photodiode. There is a drift-diffusion model in Crosslight and it can simulate the photo-detection process. Then the photocurrent waveform is exported and analyzed with MATLAB. Finally, the electrical spectrum in the frequency domain can be achieved by doing a fast Fourier transform (FFT). From the electrical spectrum, we can find the fundamental frequency and IMD3 for the OIP3 calculation.

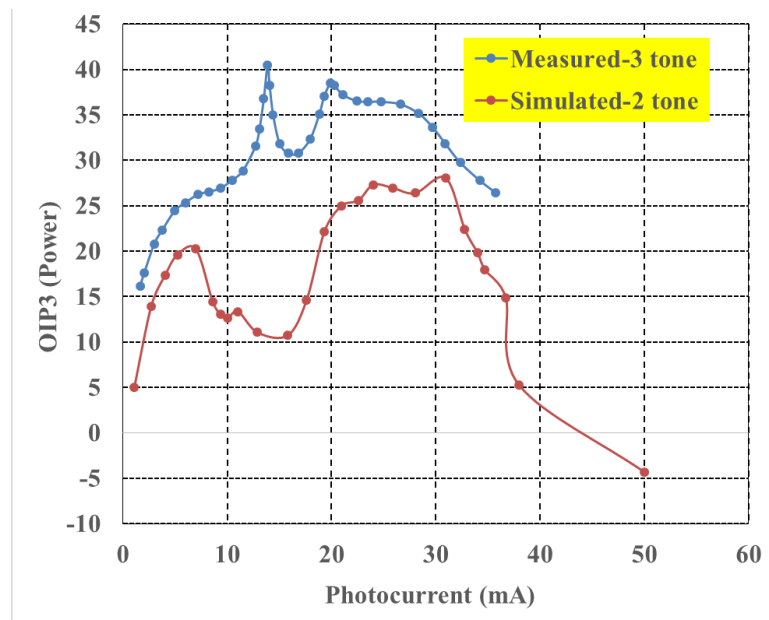


Fig. 9-3. Comparison between the measured and simulated OIP3.

Fig. 9-3 shows a comparison between the measured and simulated OIP3. The differences between the 3-tone and 2-tone OIP3 measurement are included in the calculation. These two curves exhibit similar trends, but they do not agree well with each other, especially in the frequency range of 10-20 GHz. That difference may result from the inaccurate parameters in the Crosslight simulation model or the FFT process. Further optimization of the simulation model is still needed to achieve better agreement between these results.

References

- [1.1] J. C. Campbell, A. G. Dentai, W. S. Holden, and B. L. Kasper, "High-performance avalanche photodiode with separate absorption 'grading' and multiplication regions," *Electronics Letters*, vol. 19, pp. 818-820, 1983.
- [1.2] Eui-Tae Kim, Anupam Madhukar, Zhengmao Ye, and Joe C. Campbell, "High detectivity InAs quantum dot infrared photodetectors," *Applied Physics Letters*, vol. 84, pp. 3277, 2004.
- [1.3] Zhihong Huang, James E. Carey, Mingguo Liu, Xiangyi Guo, Eric Mazur, and Joe C. Campbell, "Microstructured silicon photodetector," *Applied Physics Letters*, vol. 89, pp. 033506, 2006.
- [1.4] A. Wakatsuki, T. Furuta, Y. Muramoto and T. Ishibashia, "High-speed photodiode and optical receiver technologies," *OFC 2009*, paper OMK1, 2009.
- [1.5] D. R. Smith, R. C. Hooper, P. P. Smyth and D. Wake, "Experimental comparison of a germanium avalanche photodiode and InGaAs PINFET receiver for longer wavelength optical communication systems," *Electronics Letters*, vol. 18, pp. 453-454, 1982.
- [1.6] H Yang, N Ye, R Phelan, J O'Carroll, B Kelly, W Han, X Wang, N Nudds, N MacSuibhne, F Gunning, P O'Brien, FH Peters, B Corbett, "Butterfly packaged high-speed and low leakage InGaAs quantum well photodiode for 2000nm wavelength systems," *Electronics Letters*, vol. 49, pp. 281-282, 2013.
- [1.7] Xiaojun Xie, Kejia Li, Yang Shen, Qinglong Li, Jizhao Zang, Andreas Beling, Joe C Campbell, "Photonic generation of high-power pulsed microwave signals," *IEEE Journal of Lightwave Technology*, vol. 33, pp. 3808-3814, 2015.
- [1.8] Xiaojun Xie, Qiugui Zhou, Kejia Li, Yang Shen, Qinglong Li, Zhanyu Yang, Andreas Beling, Joe C Campbell, "Improved power conversion efficiency in high-performance photodiodes by flip-chip bonding on diamond," *Optica*, vol. 1, pp. 429-435, 2014.

- [1.9] Robert H. Hadfield, "Single-photon detectors for optical quantum information applications," *Nature Photonics*, vol. 3, pp. 696–705, 2009.
- [1.10] G. L. Mansell, T. G. McRae, P. A. Altin, M. J. Yap, R. L. Ward, B. J. J. Slagmolen, D. A. Shaddock, and D. E. McClelland, "Observation of squeezed light in the 2 μm region," *Physical Review Letter*, vol. 120, pp. 203603, 2018.
- [1.11] F. Ji, M. Juntunen, I. Hietanen and S. Eranen, "Advanced photodiode detector for medical CT imaging: design and performance," *IEEE International Symposium on Industrial Electronics*, pp. 2730-2735, 2007.
- [1.12] R. Sudharsanan, T. Parodos, A. Ruzin, Y. Nemirovsky and N. H. Karam, "CdZnTe photodiode arrays for medical imaging," *Journal of Electronic Materials*, vol. 25, pp. 1318–1322, 1996.
- [1.13] R. Bloomer, M. Pysher and O. Pfister, "Nonlocal restoration of two-mode squeezing in the presence of strong optical loss," *New Journal of Physics*, vol. 13, pp. 063014, 2011.
- [1.14] M. Pysher, R. Bloomer, C. M. Kaleva, T. D. Roberts, P. Battle, and O. Pfister, "Broadband amplitude squeezing in a periodically poled KTiOPO₄ waveguide," *Optics Letters*, vol. 34, pp. 256-258, 2009.
- [1.15] A. R. Wade, G. L. Mansell, S. S.Y. Chua, R. L. Ward, B. J. J. Slagmolen, D. A. Shaddock and D. E. McClelland, "A squeezed light source operated under high vacuum," *Scientific Reports*, vol. 5, pp. 18052, 2015.
- [1.16] X. Li, N. Li, S. Demiguel, X. Zheng, J. C. Campbell, H. H. Tan and C. Jagadish, "A partially depleted absorber photodiode with graded doping injection regions," *IEEE Photonic Technology Letters*, vol. 16, pp. 2326-2328, 2004.
- [1.17] D. Dai, M. Piels, and J. E. Bowers, "Monolithic germanium/silicon photodetectors with decoupled structures: resonant APDs and UTC photodiodes," *IEEE Journal of Selected Topics*

in *Quantum Electronics*, vol. 20, pp. 43-56, 2014.

- [1.17] Y. Li and M. Xiao, "Generation and applications of amplitude-squeezed states of light from semiconductor diode lasers," *Optics Express*, vol. 2, pp. 110-117, 1998.
- [1.18] C. Baune, J. Gniesmer, A. Schönbeck, C. E. Vollmer, J. Fiurášek, and R. Schnabel, "Strongly squeezed states at 532 nm based on frequency up-conversion," *Optics Express*, vol. 23, pp. 16035-16041, 2015.
- [1.19] X. Zhao, A. Cola, A. Tersigni, F. Quaranta, E. Gallo, J. Spanier, and B. Nabet, "Optically modulated high-sensitivity heterostructure varactor," *IEEE Electron Device Letters*, vol. 27, pp. 710-712, 2006.
- [1.20] Y. Oh, S. Kim, S. Lee, and J. Rieh, "The island-gate varactor—a high-Q MOS varactor for millimeter-wave applications," *IEEE Microwave and Wireless Components Letters*, vol. 19, pp. 215-217, 2009.
- [1.21] S. P. Bruss and R. R. Spencer, "A continuously tuned varactor array," *IEEE Microwave and Wireless Components Letters*, vol. 19, pp. 596-598, 2009.
- [1.22] H. Xu and K. K. O, "High-Q thick-gate-oxide MOS varactors with subdesign-rule channel lengths for millimeter-wave applications," *IEEE Electron Device Letters*, vol. 29, pp. 363-365, 2008.
- [1.23] P. Andreani and S. Mattisson, "On the use of MOS varactors in RF VCOs," *IEEE Journal of Solid-State Circuits*, vol. 35, pp. 905-910, 2000.
- [1.24] N. Behdad and K. Sarabandi, "Dual-band reconfigurable antenna with a very wide tunability range," *IEEE Transactions on Antennas and Propagation*, vol. 54, pp. 409 – 416, 2006.
- [1.25] M. Nouman, H. Kim, J. Woo, J. Hwang, D. Kim and J. Jang, "Terahertz modulator based on metamaterials integrated with metal-semiconductor-metal varactors," *Scientific Reports*, vol. 6,

pp. 26452, 2016.

- [1.26] R. Lopez and W. Scott, "Measurement of ground-penetrating radar antenna patterns using modulated scatterers," *Proceedings of SPIE*, vol. 5794, pp. 459-469, 2005.
- [1.27] K. Murano and Y. Kotsuka, "New controllable noise suppression methods for near-magnetic field radiations on PCB using small active component circuits," *IEEE International Symposium on Electromagnetic Compatibility*, pp. 124-127, 2013.
- [1.28] S. Shinde, S. Marathe, G. Li, R. Zoughi, and D. Pommerenke, "A frequency tunable high sensitivity H-field probe using varactor diodes and parasitic inductance," *IEEE Transactions on Electromagnetic Compatibility*, vol. 58, pp. 331-334, 2016.
- [1.29] A. Nafra, O. Jerphagnon, P. Chavarkar, M. VanBlaricum and R. York, "Indirect optical control of microwave circuits using monolithic optically variable capacitors," *IEEE Transactions on Microwave Theory and Techniques*, vol. 47, pp. 1365-1372, 1999.
- [1.30] S. Malyshev, V. Andrievski, T. Budko, C. Chen, A. Chizh, E. Gushchinskaya, B. Liu, L. Romanova, and E. Zaporozhets, "Photovaractor for optically controlled microwave circuits", *Proceedings of International Conference on Microwaves & Radar (MIKON)*, pp. 401-403, 2000.
- [1.31] S. Malyshev and A. Chizh, "Modeling and characterization of photovaractor for microwave optoelectronics," *Proceedings of European Microwave Conference*, pp. 1-4, 2001.
- [1.32] S. Malyshev and A. Chizh, "Photovaractor with enhanced quality factor," *International Conference on Microwaves, Radar & Wireless Communications*, pp. 914-917, 2006.
- [1.33] M. Lucia, J. Hernandez-Rojas, C. Leon, and I. Mártil, "Capacitance measurements of p-n junctions: depletion layer and diffusion capacitance contributions," *European Journal of Physics*, vol. 14, pp. 86-89, 1993.
- [1.34] R. Daniels, J. Murdock, T. Rappaport, and R. Heath, "60 GHz wireless: up close and personal,"

IEEE Microwave Magazine, vol. 11, no. 7, pp. 44-50, Dec. 2010.

- [1.35] A. Kim, Y. H. Joo, and Y. Kim, “60 GHz wireless communication systems with radio-over-fiber links for indoor wireless LANs,” IEEE transactions on consumer electronics, vol. 50, pp. 517-520, 2004.
- [1.36] R. C. Daniels, and R. W. Heath, “60 GHz wireless communications: Emerging requirements and design recommendations,” IEEE Vehicular Technology Magazine, vol. 2, pp. 41-50, 2007.
- [1.37] T. M. Fortier, M. S. Kirchner, F. Quinlan, J. Taylor, J. C. Bergquist, T. Rosenband, N. Lemke, A. Ludlow, Y. Jiang, C. W. Oates, and S. A. Diddams, “Generation of ultrastable microwaves via optical frequency division,” Nature Photonics, vol. 5, pp.425-429, 2011.
- [1.38] J. Kim, J. A. Cox, J. Chen, and F. X. Kärtner, “Drift-free femtosecond timing synchronization of remote optical and microwave sources,” Nature Photonics, vol. 2, pp. 733-736, 2008.
- [1.39] K. Saleh, J. Millo, B. Marechal, B. Dubois, A. Bakir, A. Didier, C. Lâcroute, and Y. Kersalé, “Photonic generation of high power, ultrastable microwave signals by Vernier effect in a femtosecond laser frequency comb,” Scientific Reports, vol. 8, 2018.
- [1.40] P. Ghelfi, F. Laghezza, F. Scotti, G. Serafino, A. Capria, S. Pinna, D. Onori, C. Porzi, M. Scaffardi, A. Malacarne, V. Vercesi, E. Lazzeri, F. Berizzi, and A. Bogoni, “A fully photonics-based coherent radar system,” Nature, vol. 507, pp. 341–345, 2014.
- [1.41] D. Kong, H. Wang, Y. Li, J. Zang, S. Zhou, X. Jia, J. Wu, and J. Lin, “Ultra-low timing-jitter clock recovery using EAM-MZM double-loop and its application in a 640Gbit/s OTDM system,” Optics Express, vol. 20, pp. B615-B623, 2012.
- [1.42] G. S. Woods, D. L. Maskell, and M. V. Mahoney, “A high accuracy microwave ranging system for industrial applications,” IEEE Transactions on Instrumentation and Measurement, vol. 42, pp. 812-816, 1993.

- [1.43] H. Bergeron, "Tight real-time synchronization of a microwave clock to an optical clock across a turbulent air path," *Optica*, vol. 3, pp. 441-447, 2016.
- [1.44] A. A. Savchenkov, E. Rubiola, A. B. Matsko, V. S. Ilchenko, and L. Maleki, "Phase noise of whispering gallery photonic hyper-parametric microwave oscillators," *Optics Express*, vol. 16, pp. 4130-4144, 2008.
- [1.45] Y. Ji, X. S. Yao and L. Malek., "Compact optoelectronic oscillator with ultra-low phase noise performance," *Electronics Letters*, vol. 35, pp. 1554-1555, 1999.
- [1.46] A. Bartels, S. A. Diddams, C. W. Oates, G. Wilpers, J. C. Bergquist, W. H. Oskay, and L. Hollberg "Femtosecond-laser-based synthesis of ultrastable microwave signals from optical frequency references," *Optics Letters*, vol. 30, pp. 667-669, 2005.
- [1.47] F. Quinlan, T. M. Fortier, M. S. Kirchner, J. A. Taylor, M. J. Thorpe, N. Lemke, A. D. Ludlow, Y. Jiang, and S. A. Diddams, "Ultralow phase noise microwave generation with an Er:fiber-based optical frequency divider," *Optics Letters*, vol. 36, pp. 3260-3262, 2011.
- [1.48] K. Jung and J. Kim, "All-fibre photonic signal generator for attosecond timing and ultralow-noise microwave," *Scientific Reports*, vol. 5, pp. 16250, 2015.
- [1.49] M. Currie and I. Vurgaftman, "Microwave phase retardation in saturated InGaAs photodetectors," *IEEE Photonics Technology Letters*, vol. 18, pp. 1433-1435, 2006.
- [1.50] T. M. Fortier, F. Quinlan, A. Hati, C. Nelson, J. A. Taylor, Y. Fu, J. Campbell, and S. A. Diddams, "Photonic microwave generation with high-power photodiodes," *Optics Letters*, vol. 38, pp. 1712-1714, 2013.
- [1.51] J. Taylor, S. Datta, A. Hati, C. Nelson, F. Quinlan, A. Joshi, and S. Diddams, "Characterization of power-to-phase conversion in high-speed P-I-N photodiodes," *IEEE Photonics Journal*, vol. 3, pp. 140-151, 2011.

- [1.52] Y. Hu, C. R. Menyuk, X. Xie, M. N. Hutchinson, V. J. Urick, J. C. Campbell, and K. J. Williams, "Computational study of amplitude-to-phase conversion in a modified untraveling carrier photodetector," *IEEE Photonics Journal*, vol. 9, pp. 1-11, 2017.
- [1.53] X. Xie, J. Zang, A. Beling, and J. Campbell, "Characterization of amplitude noise to phase noise conversion in charge-compensated modified untravelling carrier photodiodes," *IEEE Journal of Lightwave and Technology*, vol. 35, pp. 1718-1724, 2017.
- [2.1] Y. Zhao, D. Zhang, L. Qin, Q. Tang, R. Wu, J. Liu, Y. Zhang, H. Zhang, X. Yuan, and W. Liu, "InGaAs-InP avalanche photodiodes with dark current limited by generation-recombination," *Optics Express*, vol. 19, pp. 8546-8556, 2011.
- [2.2] J. Kang, H. Kim, C. Han, H. Yang, S. R. Jeon, B. Park, and H. Cha, "Enhanced UV absorption of GaN photodiodes with a ZnO quantum dot coating layer," *Optics Express*, vol. 26, pp. 8296-8300, 2018.
- [2.3] M. V. Schneider, "Schottky barrier photodiodes with antireflection coating," *Bell System Technical Journal*, vol. 45, pp. 1611-1638, 1966.
- [2.4] K. Kato, S. Hata, K. Kawano, and A. Kozen, "Design of ultrawide-band, high-sensitivity p-i-n photodiodes," *IEICE Transactions on Electronics*, vol. E76-C, pp. 214-221, 1993.
- [2.5] R., M. Norgia, G. Giuliani, S. Donati, "High-bandwidth photodiode frequency-response characterization method based on the photomixing technique," *Microwave and Terahertz Photonics*, vol. 5466, 2004.
- [2.6] Y. Hu, B. S. Marks, C. R. Menyuk, V. J. Urick, and K. J. Williams, "Modeling sources of nonlinearity in a simple p-i-n photodetector," *Journal of Lightwave Technology*, vol. 32, pp. 3710-3720, 2014.
- [2.7] A. S. Hastings, D. A. Tulchinsky, K. J. Williams, H. Pan, A. Beling, and J. C. Campbell,

- “Minimizing photodiode nonlinearities by compensating voltage-dependent responsivity effects,” *Journal of Lightwave Technology*, vol. 28, pp. 3329-3333, 2010.
- [2.8] N. J. Frigo, M. N. Hutchinson, and J. R. Peasant, “Characterization of photodiode nonlinearities by output frequency analysis,” *Journal of Lightwave Technology*, vol. 34, pp. 4696-4704, 2016.
- [2.9] X. Xie, K. Li, Q. Zhou, A. Beling, and J. C. Campbell, “High-gain, low-noise-figure, and high-linearity analog photonic link based on a high-performance photodetector,” *Journal of Lightwave Technology*, vol. 32, pp. 4187-4192, 2014.
- [2.10] J. Zang, Y. Li, Z. Yang, J. Wu, W. Li, R. Hui and J. Lin, “Tunable frequency-doubling Brillouin optoelectronic oscillator using single-sideband suppressed-carrier modulation,” *OFC 2014*, San Francisco, paper TH3D.3, 2014.
- [2.11] M. N. Draa, A. S. Hastings, and K. J. Williams, “Comparison of photodiode nonlinearity measurement systems,” *Optics Express*, vol. 19, pp. 12635-12645, 2011.
- [2.12] J. Shi, Y. Cheng, J. Wun, K. Chi, Y. Hsin, and S. D. Benjamin, “High-speed, high-efficiency, large-area p-i-n photodiode for application to optical interconnects from 0.85 to 1.55 μm wavelengths,” *Journal of Lightwave Technology*, vol. 31, pp. 3956-3961, 2013.
- [2.13] G. Wang, T. Tokumitsu, I. Hanawa, K. Sato, and M. Kobayashi, “Analysis of high speed p-i-n photodiode S-parameters by a novel small-signal equivalent circuit model,” *IEEE Microwave and Wireless Components Letters*, vol. 12, pp. 378-380, 2002.
- [2.14] E. Schibli and A. Milnes, “Effects of deep impurities on n+p junction reverse-biased small-signal capacitance,” *Solid-State Electronics*, vol. 11, pp. 323-334, 1968.
- [2.15] Y. Hu, C. R. Menyuk, X. Xie, M. Hutchinson, V. J. Urick, J. Campbell, and K. J. Williams, “Numerical modeling of amplitude-to-phase conversion in modified uni-traveling carrier (MUTC) photodetector,” *CLEO 2016*, paper JW2A.117, 2016.

- [2.17] Z. Yang, Q. Yu, J. Zang, J. C. Campbell, and A. Beling, "Phase-modulated analog photonic link with a high-power high-linearity photodiode," *Journal of Lightwave Technology*, vol. 36, pp. 3805-3814, 2018.
- [2.18] Y. Shen, J. Gaskins, X. Xie, B. M. Foley, R. Cheaito, P. E. Hopkins, and J. C. Campbell, "Thermal analysis of high-power flip-chip-bonded photodiodes," *Journal of Lightwave Technology*, vol. 35, pp. 4242-4246, 2017.
- [2.19] K. J. Williams, R. D. Esman, and M. Dagenais, "Effects of high space-charge fields on the response of microwave photodetectors," *IEEE Photonics Technology Letters*, vol. 6, pp. 639-641, 1994.
- [2.20] X. Li, N. Li, S. Demiguel, X. Zheng, J. C. Campbell, H. H. Tan, and C. Jagadish, "A partially depleted absorber photodiode with graded doping injection regions," *IEEE Photonics Technology Letters*, vol. 16, pp. 2326-2328, 2004.
- [2.21] F. J. Effenberger and A. M. Joshi, "Ultrafast, dual-depletion region, InGaAs/InP p-i-n detector," *Journal of Lightwave Technology*, vol. 14, pp. 1859-1864, 1996.
- [2.22] N. Shimizu, N. Watanabe, T. Furuta, and T. Ishibashi, "High-speed InP/InGaAs uni-traveling-carrier photodiodes with 3-dB bandwidth over 150 GHz," *55th Annual Device Research Conference Digest*, pp. 164-165, 1997.
- [2.23] X. Wang, N. Duan, H. Chen, and J. C. Campbell, "InGaAs-InP photodiodes with high responsivity and high saturation power," *IEEE Photonics Technology Letters*, vol. 19, pp. 1272-1274, 2007.
- [2.24] E. Rouvalis, C. C. Renaud, D. G. Moodie, M. J. Robertson, and A. J. Seeds, "Traveling-wave uni-Traveling carrier photodiodes for continuous wave THz generation," *Optics Express*, vol. 18, pp. 11105-11110, 2010.

- [2.25] A. Beck, G. Ducournau, M. Zaknoune, E. Peytavit, T. Akalin, J. F. Lampin, F. Mollot, F. Hindle, C. Yang, and G. Mouret, "High-efficiency uni-travelling-carrier photomixer at 1.55 μm and spectroscopy application up to 1.4 THz," *Electronics Letters*, vol. 44, pp. 1320-1321, 2008.
- [2.26] J. Shi, F. Kuo, and M. Chou, "A linear cascade near-ballistic uni-traveling-carrier photodiodes with extremely high saturation-current bandwidth product (6825mA-GHz, 75mA/91GHz) under a 50 Ω load," *OFC 2010*, paper PDPA6, 2010.
- [2.27] X. Xie, Q. Zhou, K. Li, A. Beling, and J. C. Campbell, "1.8 Watt RF power and 60% power conversion efficiency based on photodiode flip-chip-bonded on diamond," *CLEO 2014*, paper JTh5B.9, 2014.
- [3.1] Web: https://nanolab.berkeley.edu/process_manual/chap6/6.20PECVD.pdf
- [3.2] T. Clausen and O. Leistiko, "Metallurgical optimization for ohmic contacts to InP using conventional metallization schemes," *Microelectronic Engineering*, vol. 18, pp. 305-325, 1992.
- [3.3] A. Beling, X. Xie, and J. C. Campbell, "High-power, high-linearity photodiodes," *Optica*, vol. 3, pp. 328-338, 2016.
- [3.4] X. Xie, Q. Zhou, K. Li, Y. Shen, Q. Li, Z. Yang, A. Beling, and J. C. Campbell, "Improved power conversion efficiency in high-performance photodiodes by flip-chip bonding on diamond," *Optica*, vol. 1, pp. 429-435, 2014.
- [4.1] W. Sun, Z. Lu, X. Zheng, J. C. Campbell, S. J. Maddox, H. P. Nair, and S. R. Bank, "High-Gain InAs Avalanche Photodiodes," *IEEE Journal of Quantum Electronics*, vol. 49, pp. 154-161, 2013.
- [5.1] F. Capasso, R. Logan, W. Tsang, and J. Hayes, "Channeling photodiode-a new versatile interdigitated p-n junction photodetector," *Applied Physics Letters*, vol. 41, pp. 944-946, 1982.
- [5.2] C. Tsai, J. Campbell, and R. Dupuis, "Optically controlled varactor diode," *Journal of Applied Physics*, vol. 70, pp. 3989-3990, 1991.

- [5.3] H. Memarzadeh-Tehran, J. J. Laurin and R. Kashyap, "Optically modulated probe for precision near-field measurements," *IEEE Transactions on Instrumentation and Measurement*, vol. 59, pp. 2755-2762, 2010.
- [6.1] K. M. Cheng and M. J. Chi, "A varactor-based variable attenuator design with enhanced linearity performance," *IEEE Transactions on Microwave Theory and Techniques*, vol. 63, pp. 3191-3198, 2015.
- [6.2] C. R. Trent and T. M. Weller, "S-band reflection type variable attenuator," *IEEE Microwave and Wireless Components Letters*, vol. 12, pp. 243-245, 2002.
- [6.3] O. V. Stukach, "Variable attenuator with low phase shift," *2006 European Conference on Wireless Technology*, pp. 241-244, 2006.
- [6.4] C. E. Saavedra and Y. Zheng, "Ring-hybrid microwave voltage-variable attenuator using HFET transistors," *IEEE Transactions on Microwave Theory and Techniques*, vol. 53, pp. 2430-2434, 2005.
- [6.5] S. Bulja and A. Grebennikov, "Variable reflection-type attenuators based on varactor diodes," *IEEE Transactions on Microwave Theory and Techniques*, vol. 60, pp. 3719-3727, 2012.
- [6.6] S. Walker, "A low phase shift attenuator," *IEEE Transactions on Microwave Theory*, vol. 42, pp. 182-185, 1994.
- [6.7] Y. Dai, D. Fang, and Y. Guo, "A Novel UWB (0.045-50 GHz) digital/analog compatible MMIC variable attenuator with low insertion phase shift and large dynamic range," *IEEE Microwave and Wireless Components Letters*, vol. 17, pp. 61-63, 2007.
- [7.1] D. Phung, M. Merzougui, C. Alexandre, and M. Lintz, "Phase measurement of a microwave optical modulation: characterisation and reduction of amplitude-to-phase conversion in 1.5 μm high bandwidth photodiodes," *IEEE Journal of Lightwave Technology*, vol. 32, pp. 3759-3767,

2014.

- [7.2] J. Guillory, J. García-Márquez, C. Alexandre, D. Truong, and J.-P. Wallerand, “Characterization and reduction of the amplitude-to-phase conversion effects in telemetry,” *Measurement Science and Technology*, vol. 26, pp. 084006, 2015.
- [7.3] M. Lessing, H. S. Margolis, C. T. A. Brown, P. Gill, and G. Marra, “Suppression of amplitude-to-phase noise conversion in balanced optical-microwave phase detectors,” *Optics Express*, vol. 21, pp. 27057-27062, 2013.
- [7.4] F. N. Baynes, F. Quinlan, T. M. Fortier, Q. Zhou, A. Beling, J. C. Campbell, and S. A. Diddams, “Attosecond timing in optical-to-electrical conversion,” *Optica*, vol. 2, pp. 141-146, 2015.
- [7.5] W. Zhang, T. Li, M. Lours, S. Seidelin, G. Santarelli, and Y. Le Coq, “Amplitude to phase conversion of InGaAs pin photo-diodes for femtosecond lasers microwave signal generation,” *Applied Physics B: Lasers and Optics*, vol. 106, pp. 301-308, 2011.
- [7.6] R. Bouchand, D. Nicolodi, X. Xie, C. Alexandre, and Y. Le Coq, “Accurate control of optoelectronic amplitude to phase noise conversion in photodetection of ultra-fast optical pulses,” *Optics Express*, vol. 25, pp. 12268-12281, 2017.
- [7.7] H. Ito, S. Kodama, Y. Muramoto, T. Furuta, T. Nagatsuma, and T. Ishibashi, “High-speed and high-output InP-InGaAs unitraveling-carrier photodiodes,” *IEEE Journal of Selected Topics in Quantum Electronics*, vol. 10, pp. 709-727, 2004.
- [7.8] H. Pan, “High-power high-linearity photodiodes and high-power photodiodes as optoelectronic mixers,” 2011 (Doctoral dissertation).
- [8.1] Rohde&Schwarz application note: “1EZ35: Group and Phase Delay Measurements with Vector Network Analyzer ZVR,” 1997.
- [8.2] S. M. Sze and K. K. Ng, *Physics of Semiconductor Devices* 3rd edition (Wiley, 2007).

- [9.1] K. J. Williams, L. T. Nichols, and R. D. Esman, "Photodetector nonlinearity limitations on a high-dynamic range 3 GHz fiber optic link," *Journal of Lightwave Technology*, vol. 16, pp. 192-199, 1998.
- [9.2] A. Beling, H. Pan, H. Chen, and J. C. Campbell, "Measurement and Modeling of a High-Linearity Modified Uni-Traveling Carrier Photodiode," *IEEE Photonics Technology Letters*, vol. 20, pp. 1219-1221, 2008.

A. List of publications

- [1] **Jizhao Zang**, Jesse S. Morgan, Xiaojun Xie, Keye Sun, Qinglong Li, Andreas Beling, and Joe C. Campbell, “InP/InGaAs Photovaractor,” *IEEE Journal of Lightwave Technology*, vol. 36, pp. 1661-1665, 2017.
- [2] **Jizhao Zang**, Xiaojun Xie, Qianhuan Yu, Zhanyu Yang, Andreas Beling, and Joe C. Campbell, “Reduction of amplitude-to-phase conversion in charge-compensated modified unitravelling carrier photodiodes,” *IEEE Journal of Lightwave Technology*, under review.
- [3] **Jizhao Zang**, Jesse Morgan, Andreas Beling, and Joe C. Campbell, “Optically controlled microwave attenuator based on InP/InGaAs photovaractor,” *IPC 2018*, under review.
- [4] **Jizhao Zang**, Zhanyu Yang, Xiaojun Xie, Min Ren, Yang Shen, ZackCarson, Olivier Pfister, Andreas Beling, and Joe C. Campbell, “High quantum efficiency uni-traveling-carrier photodiode,” *IEEE Photonics Technology Letters*, vol. 29, pp. 302-305, 2017.
- [5] **Jizhao Zang**, Xiaojun Xie, Qianhuan Yu, Keye Sun, Andreas Beling, and Joe C. Campbell, “Reduction of amplitude-to-phase conversion in charge-compensated modified unitravelling carrier photodiodes,” *CLEO 2018*, paper SM2L.2, 2018.
- [6] Jesse Morgan, **Jizhao Zang**, Keye Sun, Bassem Tossoun, Joe C. Campbell and Andreas Beling, “Zero-bias photovaractor with 60 GHz resonant network for optically modulated scatterer (OMS) application,” *CLEO 2018*, paper STu3B.5, 2018.
- [7] Xiaojun Xie, **Jizhao Zang**, Andreas Beling, and Joe Campbell, “Characterization of amplitude noise to phase noise conversion in charge-compensated modified unitravelling carrier photodiodes,” *IEEE Journal of Lightwave Technology*, vol. 35, pp. 1718-1724, 2017.
- [8] Bassem Tossoun, **Jizhao Zang**, Sadhvikas Addamane, Ganesh Balakrishnan, Archie Holmes, Jr., and Andreas Beling, “InP-based waveguide-integrated photodiodes with InGaAs-GaAsSb

- type-II quantum wells and 10-GHz bandwidth at 2 μm ,” *IEEE Journal of Lightwave Technology*, under review.
- [9] Zhanyu Yang, Qianhuan Yu, **Jizhao Zang**, Joe C. Campbell, and Andreas Beling, “Phase-modulated analog photonic link with a high-power high-linearity photodiode,” *IEEE Journal of Lightwave Technology*, vol. 36, pp. 3805-3814, 2018.
- [10] Josue Davila-Rodriguez, Xiaojun Xie, **Jizhao Zang**, Chris Long, Tara M. Fortier, Holly Leopardi, T. Nakamura, Joe. C. Campbell, Scott A. Diddams, and Franklyn Quinlan, “Nonlinearity cancellation in high-speed photodiodes,” *Optica*, under review.
- [11] Shaoqi Feng, Yang Shen, Xiaojun Xie, **Jizhao Zang**, Siwei Li, Tiehui Su, Kuanping Shang, Weicheng Lai, Guangyao Liu, Joe C Campbell and S. J. Ben Yoo, “Hybrid integration of modified uni-traveling carrier photodiodes on a multi-layer silicon nitride platform using total internal reflection mirrors,” *OFC 2017*, paper W2A.4.
- [12] Yang Shen, Shaoqi Feng, Xiaojun Xie, **Jizhao Zang**, Siwei Li, Tiehui Su, Kuanping Shang, Weicheng Lai, Guangyao Liu, S. J. Ben Yoo and Joe C Campbell, “Hybrid integration of modified uni-traveling carrier photodiodes on a multi-layer silicon nitride platform using total reflection mirrors,” *Optics Express*, vol. 25, pp. 9521-9527, 2017.
- [13] Zhanyu Yang, Robert Costanzo, Nicolas Raduazo, **Jizhao Zang**, Steven Bowers, and Andreas Beling, “Low-noise balanced photoreceiver with 21 V/W optical conversion gain,” *Integrated Photonics Research, Silicon and Nanophotonics 2017*, paper IM3A.5.
- [14] Xiaojun Xie, Kejia Li, Yang Shen, Qinglong Li, **Jizhao Zang**, Andreas Beling, Joe C Campbell, “Photonic generation of high-power pulsed microwave signals,” *IEEE Journal of Lightwave Technology*, vol. 33, pp. 3808-3814, 2015.
- [15] Qinglong Li, Keye Sun, Kejia Li, Qianhuan Yu, **Jizhao Zang**, Ze Wang, Patrick Runge, Willi

- Ebert, Andreas Beling, and Joe C. Campbell, "Waveguide-integrated high-speed and high-power photodiode with >105 GHz bandwidth," *IPC 2017*, pp. 49-50, 2017.
- [16] Keye Sun, Daehwan Jung, Chen Shang, Alan Liu, Jesse Morgan, **Jizhao Zang**, Qinglong Li, Jonathan Klamkin, John E. Bowers, and Andreas Beling, "Low dark current III–V on silicon photodiodes by heteroepitaxy," *Optics Express*, vol. 26, pp. 13605-13613, 2018.
- [17] Qianhuan Yu, Ye Wang, Linli Xie, Souheil Nadri, Keye Sun, **Jizhao zang**, Qinglong Li, Robert Weikle and Andreas Beling, "High-performance InGaAs/InP photodiodes on silicon using low-temperature wafer-bonding," *CLEO 2018*, paper SM2I.1, 2018.
- [18] Xiaojun Xie, Anand Ramaswamy, Yang Shen, Zhanyu Yang, Matt Jacob-Mitos, Ye Wang, **Jizhao Zang**, Erik Norberg, Greg Fish, Joe C. Campbell and Andreas Beling, "Heterogeneously integrated waveguide-coupled photodiodes on silicon-on-diamond (SOD)," *Infrared Sensors, Devices, and Applications VI*, 2011.

B. Vita

Jizhao Zang (臧继召), son of Zhangqian Zang (臧章前) and Chaoyu Zhao (赵超玉), elder brother of Shanshan Zang (臧姗姗), was born on July 22th, 1991 in City of Baoding, Hebei Province, China. After completing his study at Qingyuan middle school in 2008, he began his undergraduate study at School of Science in Beijing University of Posts and Telecommunications (BUPT), majoring in Applied Physics. After graduation in 2012, he pursued his master degree at Institute of Information Photonics & Optical Communications in BUPT. At BUPT, he worked on ultra-high speed OTDM fiber communication systems and optoelectronic oscillators under the supervision of Dr. Yan Li (李岩) and Dr. Jian Wu (伍剑). In May 2015, he joined Dr. Joe. C. Campbell's group as a PhD student. His current research focuses on the design, fabrication and characterization of high power and high quantum efficiency photodiodes.

This dissertation has been typed by the author.